BINDING SERVICES
Tel +44 (0)29 2087 4949
Fax +44 (0)29 20371921
e-mail bindery@cardiff.ac.uk

Investigation of laser milling process characteristics for micro tooling applications

A thesis

submitted to the

Cardiff University

for the degree of

Doctor of Philosophy

by

Todor Dobrev

Manufacturing Engineering Centre

Cardiff University

United Kingdom

September, 2005

ProQuest LLC
789 East Eisenhower Parkway
P.O. Box 1346
Ann Arbor, MI 48106-1346

Summary

Laser milling is a new application that is challenging for the power contained in the laser light. Due to its small unit of material removal, accuracy and repeatability, laser milling has found an application area in micro manufacturing, especially the manufacturing of microtools. There is a number of micro manufacturing and replication processes on the market at present. Their needs raise the requirements that have to be met by the microtool manufacturing process.

Initially, the requirements of micro manufacturing processes, such as micro-injection moulding and hot-embossing, are identified and compared to what the laser milling process can achieve. An investigation is carried out to identify the capabilities of the laser milling process and match them to these requirements. The investigated process characteristics are surface finish, aspect ratio, accuracy and minimum feature size.

Furthermore, as surface finish is identified to be a considerable constraint, an investigation is undertaken to improve the resulting surface finish obtained from the laser milling process. A two-dimensional theoretical model is developed to investigate the crater formation on a metal target by a microsecond laser pulse. The model takes into account the absorption of the laser light by the target, and simulates the heating and vaporisation of the material, including an adjustment to compensate for the change of state. A simple numerical technique is employed to describe the major physical processes taking part in the laser milling process. Experimental validation of the proposed model is provided for two common tooling materials.

To investigate the formation of the material surface after laser milling, a complex 3D surface model is presented based on the single crater profiles of the 2D theoretical model together with a consideration for the overlapping of the craters. Additional factors, that are influential in the formation of the final material surface, are also considered and their effect on the surface roughness estimated.

Finally, a number of techniques for reducing surface roughness are presented. Laser cleaning is a technique that utilises the de-focused laser beam to "smooth out" the material surface irregularities. The other three techniques are applied after laser milling, and are ultrasonic cleaning bath, chemical pickling and electro-chemical polishing.

Acknowledgements

I would like to express my thanks to my supervisor and Director of the Manufacturing Engineering Centre, Professor D. T. Pham, for giving me this opportunity and for his valued supervision and support during my research.

Also my thanks go to my second supervisor Dr. S. Dimov, for his assistance and constructive advice in the course of this work.

To all colleagues and friends at the Manufacturing Engineering Centre, I would like to express my gratitude for their patience and continuous support. Special thanks go to Mr. P. Petkov, Dr. Kr. Popov, Mr. At. Ivanov, Dr. N. Zlatov and Mr. C. Ferri for their constant assistance through technical help, countless discussions and unquestionable support.

My deepest gratitude goes to my family and friends that have supported me through this journey. My family, with their belief in me, have given me their love and support that I needed.

Contents

List of tables

List of figures

Abbreviations

ASE	Advanced Silicon Etch
CAD	Computer-Aided Design
CNC	Computer Numerical Control
CW	Continuous Wave
DEEMO	Dry Etching, Electroplating and Moulding process
ECM	Electro-Chemical Machining
ECP	Electro Chemical Polishing
Excimer	EXCIted diMER laser
HAZ	Heat Affected Zone
IR	Infrared
ISO	International Organization for Standardization
IT	International Tolerance Grade
LIGA	**LI**tographie **G**alvanoformung **A**bformung (Lithography Electroforming Moulding)
MEMS	Micro-Electro Mechanical Systems
micro-EDM	micro Electro Discharge Machining
NC	Numerical Control
Nd:YAG	Neodymium yttrium aluminum garnet
PC	Polycarbonate
PDMS	Polydimethylsiloxane
PMMA	Polymethylmetacrylate

SEM	Scanning Electron Microscope
STL	Stereolithography interface format
TEM_{00}	Transversal Electromagnetic Mode 00
UV	Ultraviolet
WEDG	Wire Electro Discharge Grinding

Nomenclature

α	[m^{-1}]	absorption coefficient
λ	[μm]	wavelength
π	[-]	3.1415
ρ	[kg/m^3]	material density
τ	[μs]	pulse duration
Δt	[s]	time increment
Δx	[μm]	increment in *x*
Δz	[μm]	increment in *z* depth
$2w_0$	[μm]	diameter of Gaussian beam with e^{-2} of the full irradiance
A(x, z, t)		volume heat source
AR	[ ]	
C_p	[J/kg.K]	specific heat capacity
D	[m^2/s]	thermal diffusivity
d, l, w	[mm]	depth, length and width of pocket
d_m	[μm]	measured crater depth
d_s	[μm]	simulated crater depth
f	[kHz]	pulse frequency
F_0	[J/cm^2]	laser fluence
I	[%]	laser flashlamp current
i, j, k	[-]	indexes in numerical solution for t, x, z respectively
I_0	[W/m^2]	peak laser intensity
k	[W/mK]	thermal conductivity

L_m	[kJ/kg]	latent heat of melting
L_v	[kJ/kg]	latent heat of vaporization
M^2	[-]	laser beam quality factor
$P(\infty)$	[W]	total power of a Gaussian beam
$P(r)$	[W]	power within radius r of a Gaussian beam
$p(x,t)$		temporal and spatial power distribution of the laser pulse
r	[µm]	radial variable
R_a, R_y	[µm]	surface roughness parameters
s_2	[mm]	focus distance between the lens and focal spot
T	[K]	temperature
T_g	[K]	glass transition temperature
t	[s]	time variable
T_f	[s]	pulsing period
T_m	[K]	melting temperature
T_v	[K]	boiling temperature
V	[mm/s]	scanning speed
x	[mm]	space domain variable
y	[mm]	space domain variable
z	[mm]	space domain variable

Chapter 1 Introduction

1.1 Motivation

Laser milling is a new and rapidly emerging manufacturing process. It is based on the laser ablation phenomenon in which a target material is exposed to highly focused pulsed laser light. Due to its high energy density, the incident laser heats up the target to such high temperatures that a small volume of material is instantly evaporated. Scanning the pulsed beam along the top surface of a target removes material in a way similar to conventional milling. However as a relatively new technology, the manufacturing capabilities of the process are still not well defined and in order to properly apply the process, its capabilities have to be mapped against the requirements of the possible applications (Lierath et al, 2003; Kaldos et al, 2004).

One such application area is the microtooling industry, where the need for accurate and relatively small features is fuelled by the increasing world market demand for product miniaturisation. New micro-manufacturing technologies, such as micro-injection moulding and hot embossing, raise a number of challenges for the tool manufacturing process. These challenges have to be identified and turned into quantifiable process requirements, so that an appropriate manufacturing process could be identified.

1.2 Objectives

The aim of the project is to map the requirements of applications such as micro-injection moulding and hot embossing and apply them to laser milling as a microtool manufacturing process.

The project will cover the investigation of the tool manufacturing process, which will be carried out in order to fit its capabilities to the needs of the two applications. As micro fabrication applications, micro-injection moulding and hot embossing both present a set of requirements to the micro tooling process. Some of these requirements may be the same, but probably each of the applications will have its own different requirements. For example, in micro-injection moulding, a draft angle is required on deep walls, while in hot embossing such a draft angle is not reported. On the other hand, both processes demand a good surface finish, due to the fact that in a micro component, unless care is taken, roughness can compare to the feature size.

The expected set of requirements concerns:

- Surface finish
- Aspect ratio
- Accuracy
- Minimum feature size

After identifying these requirements, laser milling can be tested and the process capabilities identified. A set of experiments are to be designed and carried out on the laser milling machine for each requirement, and then the results to be measured and compared to the identified values. The structure of the test components will probably

represent the application process capabilities, but some identical features will provide ground for comparison.

Surface roughness is expected to be a great challenge for the laser milling process. Thus, the factors and process parameters that govern the resulting surface topography are to be investigated in-depth. The average surface roughness achieved by laser milling is in the region of 2 μm, but this shows a high dependency on the type of target material used. Through a laser material interaction model of the process, it is possible to create a model of a single crater from a single laser pulse. After confirming the accuracy of the crater model with two different tooling materials through a number of validation experiments, the single crater model can be useful in better understanding the influence of different parameters on the laser milling process.

The crater profiles obtained from the theoretical model are to be utilised for creating a model of a laser milled 3D surface. The surface model will provide a comprehensive view of the topography of the laser machined surfaces and will be used to identify the effect and importance of the different laser milling parameters on the surface roughness. Parameters such as laser beam power and laser spot size are expected to be most influential on the shape and size of the single craters, while marking speed, laser pulse frequency and hatching distance, i.e. overlapping, to be more significant in the more complex (3D) surface topography models (Kaldos et al, 2004).

The next objective is to investigate a number of techniques for cleaning and improving the surface roughness: ultrasound bath, deoxidisation (or *pickling*), laser cleaning and electrochemical polishing. The ultrasound bath and deoxidisation

processes offer a non-intrusive cleaning of the debris and recast layer left from laser milling. Laser cleaning is a process based on the laser milling principles, but with such a set-up that the laser beam is out of focus in the work plane. Thus, the laser only "irons out" the surface irregularities left from the preceding laser milling operation.

Electrochemical polishing streamlines the microscopic surface of a metal object by removing metal from the object's surface through an electrochemical process. In very basic terms, the object to be electrochemically polished is immersed in an electrolyte and subjected to a direct electrical current. The object is maintained anodic, with the cathodic connection being made to a nearby metal conductor.

The effects of all cleaning processes on the roughness of laser milled surface are to be investigated. A sequential combination of processes is also possible for further improvement of the surface quality.

1.3 Outline of thesis

Chapter 2 presents an in-depth account of two of the latest micro-replication techniques: micro-injection moulding and hot-embossing. A discussion of available micro tool manufacturing processes is carried out, together with an analysis of their capabilities. The chapter continues with a description of the state-of-the-art laser milling process. The governing factors of the ablation process are discussed and the key parameters identified. An extensive review of the physical phenomena

underlying the laser/material interaction is presented to better understand the material removal process.

Chapter 3 takes a closer look at the micro-manufacturing capabilities of the laser milling process. Four process characteristics are identified as being of significance for the micro-tooling applications: surface finish, aspect ratio, dimensional accuracy and minimum feature size. An experimental investigation is carried out for each of the process characteristics. The capabilities of laser milling are measured for each characteristic and improved where possible.

In Chapter 4, a comprehensive account of the latest and classical theoretical models of laser ablation is presented. These models cover a wide range of laser ablation processes: continuous wave (CW) and pulsed laser, stationary and moving laser, and a wide range of pulse durations, from microsecond pulse laser to the ultrafast femtosecond. A description is given of the theoretical model developed by the author to simulate the material removal from a microsecond Nd:YAG laser (λ = 1064 nm). A numerical solution for the heat conduction equation with a volume heat source resulting from the absorption of the laser light is proposed. The theoretical model also takes into account the change of state for the target material. The chapter concludes with the results from an experiment carried out to measure the profile of the material removed (crater) from a single laser pulse. Two different materials were selected for the simulation validation: aluminium 6082 and stainless steel Grade 316.

Chapter 5 further develops the modelling of the laser milling process to investigate the factors that are significant in the formation of the 3D surface. The factors are

separated in two groups: base surface formation factors and secondary surface formations. The base surface is shaped mainly by two laser milling process characteristics: the crater profile and the overlapping of the neighbouring craters. The secondary surface formations are basically the factors that are detrimental to the final surface finish, such as debris and recast formations, and the crater shape imperfections.

Chapter 6 introduces four methods for cleaning and improving the surface roughness of a laser machined surfaces. The four techniques are: laser cleaning, ultrasonic cleaning, deoxidisation (or *pickling*), and electro-chemical polishing (ECP).

Chapter 7 summarizes the contributions in the presented work, together with the major conclusions. The chapter concludes with suggestions for future research.

Chapter 2 Background

In this chapter, a review of micro replication processes is presented, namely microinjection moulding and hot embossing. A discussion of available micro tool manufacturing processes is carried out, together with an analysis of their capabilities.

Later in the chapter, an extensive review of the physical phenomena underlying the interaction between a laser beam and a workpiece and the mechanisms governing the ablation process is introduced with a view to identifying the key process parameters. Then the laser milling process is described in detail, and the available machine layouts are introduced.

2.1 Micro manufacturing processes

The commercialisation of microsystem technology requires low-cost microfabrication processes that are more suitable for high-volume production (Becker and Gärtner, 2001). Such microsystems are employed in a wide variety of different applications, such as microfluidic devices, micro-optics, etc and the introduction of new materials will open up opportunities for increasing economic efficiency, for new fields of applications as well as for innovative products in the future (Gale, 1997; Ruprecht et al, 2002; Gietzelt et al, 2004).

2.1.1 Micro injection moulding

In general micro injection moulding is the production of plastic parts with structure dimensions in the micron or sub-micron range (Kemmann and Webber, 2001; Piotter et al, 2002). Key products for this process are acceleration and pressure sensors and components for the computer industry, such as flat display monitors. Even if polymer products do not take over the silicon-based market at present, they are already performing excellently in the fields of medical technology, biotechnology and optical network components.

The fabrication of micro structured mould inserts requires the application of ultra precision processes (Lin et al, 2000; Kjær et al, 2002). The LIGA technique is a special technology often used in micro technology that allows the precise production of microstructures with very high aspect ratio and high quality surfaces (Spennemann and Michaeli, 2001; Alting et al, 2003). For micro-moulds with aspect ratios < 5, traditional manufacturing processes, e.g. micro-cutting, micro-EDM and laser erosion, are supposed to be cost effective alternatives. Schaller et al, 1999 report the machining of 50 μm grooves in stainless steel and brass with an aspect ratio of three. Spennemann and Michaeli (2001) compare ten different mould inserts fabricated by the three conventional fabrication processes. The laser erosion process provided freedom of design of the structures as well as wide choice of the cavity material. The drawback was the high surface finish of the cavity that was replicated onto the moulded component. As the cavities did not show any damage after the injection moulding trials, it was concluded that laser erosion should be developed further to become a viable option for the production of micro cavities. The significance of the

surface finish (Ra) in micro injection moulding is further investigated by Provatas et al, 2002 and Tay et al, 2005.

2.1.2 Hot embossing

Hot embossing is a technology of polymer micro-fabrication that is becoming increasingly important as a low-cost alternative to the silicon or glass-based MEMS technologies (Becker and Heim, 2000). The hot embossing process is described in Figure 2.1. The process starts with the design of the microstructure, which is then fabricated on the replication master.

There are different methods for producing the embossing master. Photolithography is the most common master fabrication process. In this process, a photoresist is exposed to a mask with the desired design, the resulting topography is then electroplated into a nickel galvanic bath. After stripping the resist, a nickel embossing master is produced. Silicon is another alternative material that can be used directly as an embossing tool (Becker and Heim, 1999; Becker and Gärtner, 2001; Alting et al, 2003) and delivers a low-cost access to a microfabrication process due to the latest advances in silicon deep dry etching. Beforehand, the tool fabrication produced by the advanced silicon etch processes (ASE or BOSCH-process) suffered from the poor surface finish of the etched silicon and undercuts at the bottom of etched trenches. Novel process developments (Chabloz et al, 1999; Waits et al, 2003; Waits et al, 2005) display great potential for the use of dry etching techniques for the production of embossing tools. Finally, LIGA (Becker et al, 1986; Ghodssi et al, 1998; Makarova et al, 2003) is a well established process for the production of MEMS and

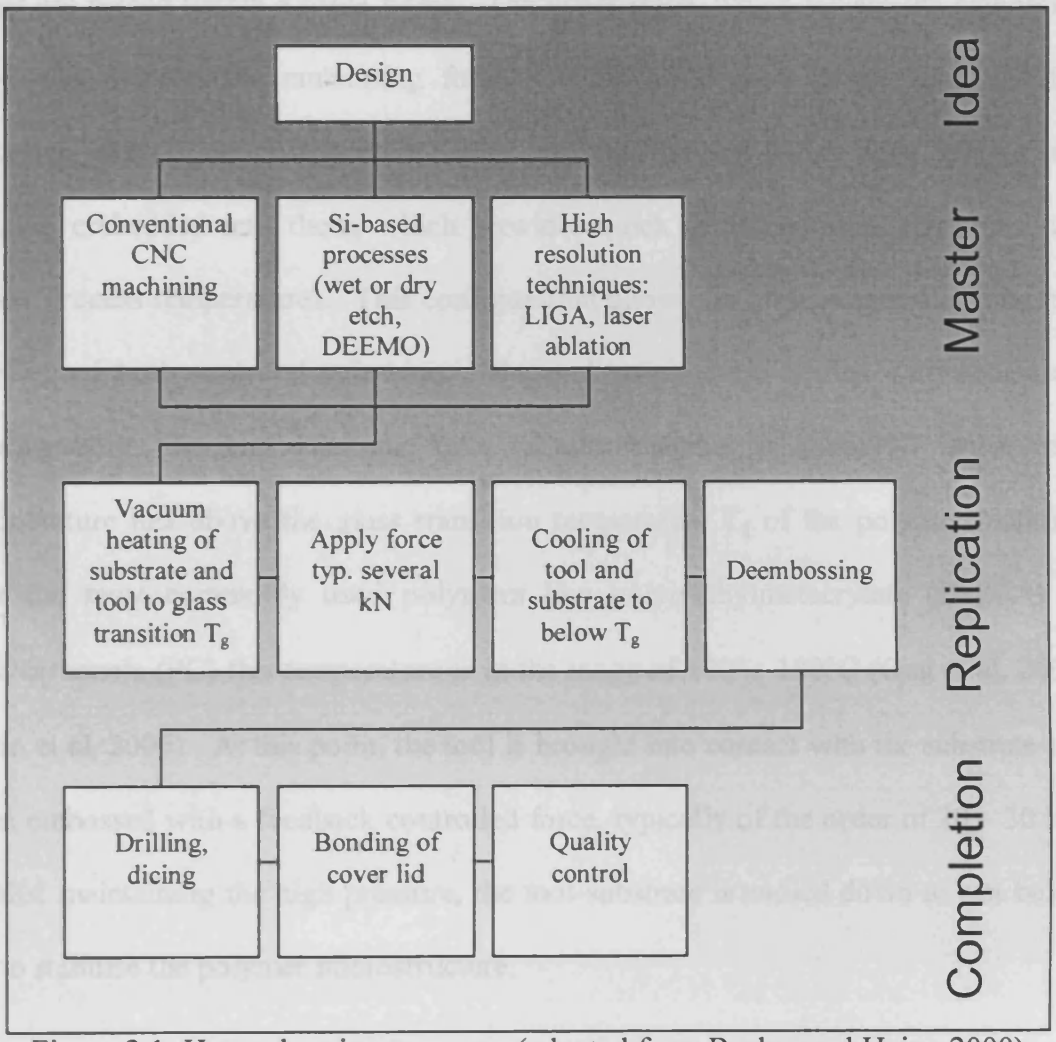

Figure 2.1 Hot embossing process - (adapted from Becker and Heim, 2000)

high aspect ratio structures, but so far lacks the commercial feasibility due to its high cost.

When the master is complete the whole embossing tool is assembled into the hot embossing machine (see Figure 2.2). A fixed bottom platform and a movable upper stage are placed within a force frame. The upper stage, which houses the embossing tool, also delivers the embossing force. On top of the bottom platform, the flat polymer substrate is positioned. Both upper and bottom plates have heating and cooling embedded into them, which provides quick cycles between the upper and lower process temperatures. This configuration allows for an isothermal heating and cooling of both tool and substrate. The embossing cycle begins with separately heating both, tool and substrate, in a vacuum chamber at about 10^{-1} mbar to a temperature just above the glass transition temperature T_g of the polymer material. For the most commonly used polymers like polymethylmetacrylate (PMMA) or polycarbonate (PC) this temperature is in the range of 100° - 180°C (Ong et al, 2002; Shan et al, 2005). At this point, the tool is brought into contact with the substrate and then embossed with a feedback controlled force, typically of the order of 20 – 30 kN. Whilst maintaining the high pressure, the tool-substrate is cooled down to just below T_g to stabilise the polymer microstructure.

When the system has reached the lower cycle temperature, the embossing tool is mechanically driven apart from the substrate, which now has a positive imprint of the desired structures.

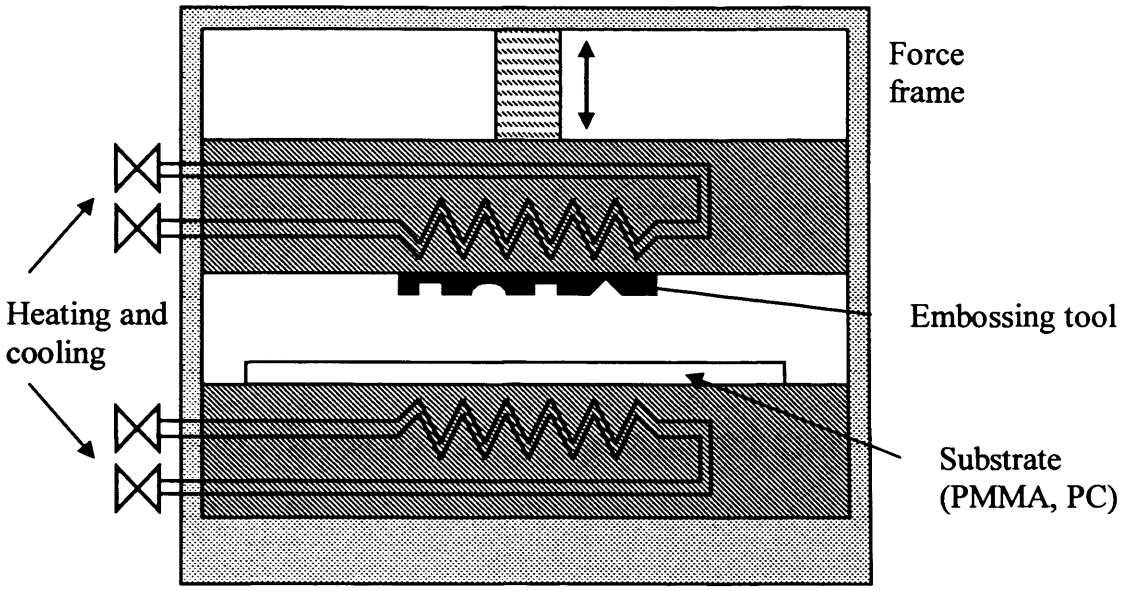

Figure 2.2 Schematic drawing of the hot embossing equipment

Bogdanski et al, (2004) has reported successfully replicating 3D structures with and without dovetail-like undercut in a silicon tool. The tool was prepared through a highly challenging laser ablation process followed by wet anisotropic etching, resulting in the dovetail-like undercut. Large area periodical structures were later replicated in thin layers of PMMA and polydimethylsiloxane (PDMS). The replication featured smooth surfaces and sharp edges despite the challenging patterns investigated.

2.2 Laser ablation

Laser milling is a new manufacturing technology suitable for machining a wide range of materials, including most metals, glass, ceramics and plastics (Tsai and Chen, 2003; Meijer, 2004; Nikumb et al, 2004). The beam from a pulsed or continuous laser source can readily be focused onto a solid material to cause sufficient heating to give surface evaporation. This process, also known as laser ablation, is particularly appropriate for hard metals and ceramics that cannot be machined by conventional means without incurring time and expense in creating special tooling (Costa et al, 2003; Pham et al, 2004).

2.2.1 Laser sources

Given a particular material to be machined, the type of laser used determines how a laser will interact with the material. There are three types of laser: semiconductor-diode, solid-state and gas lasers. Table 2.1 (Fraunhofer Institut Lasertechnik, 2003)

lists the operating mode, wavelength, power and typical applications of commonly adopted lasers.

In manufacturing, the most widely employed lasers are the CO_2 laser, the Nd:YAG laser and the *excimer* laser.

The CO_2 laser is an example of a gas laser that employs a mixture of helium and nitrogen as the protective atmosphere, and carbon dioxide as the laser emitting material. The CO_2 laser produces a collimated coherent beam in the infrared region (10.6 μm), which is characteristic of the active material. The wavelength is strongly absorbed by glass or polymers, so either mirrors or ZnSe lenses with excellent infrared transparency are used to handle the beam (Madou, 2001).

The Nd:YAG laser is a solid-state laser producing a collimated coherent beam in the near-infrared region of wavelength 1064 nm that can be either pulsed or continuous. In pulsed mode, peak-power pulses of up to 3 kW are now available. The shorter wavelength allows the adoption of optical glasses to control the beam position. By means of optical conversion techniques, it is possible to double, triple (Hellrung et al, 1999; Hayl et al, 2001) and even quadruple the fundamental emission frequency, thereby obtaining higher harmonics of wavelengths equal to 532, 355 and 266 nm, respectively.

	Wavelength	Power	Operating mode	Applications
Semiconductor diode lasers				
Single diodes	Infrared to visible	1 mW - 100 mW	Continuous and pulsed modes	Optoelectronics
Diode laser bars	Infrared to visible	up to 100 W	Continuous and pulsed modes	Pumping light source for solid state lasers
Solid state lasers				
Nd:YAG laser	1.06 μm	1 W - 3 kW	Continuous and pulsed modes	Materials processing, dimensional metrology, medicine
Ruby laser	Red	Several MW	Pulsed mode	Dimensional metrology, pulse holography
Gas lasers				
CO_2- Laser	10.6 μm	1 W – 40 kW (100 MW in pulsed mode)	Continuous and pulsed modes	Materials processing, medicine, isotope separation
Excimer laser	193 nm, 248 nm, 308 nm (and others)	1 kW - 100 MW	Pulsed mode, 10 ns - 100 ns	Micro-machining, laser chemistry, medicine
HeNe laser	632.8 nm (most common)	1 mW - 1 W	Continuous mode	Dimensional metrology, holography
Argon ion laser	515 & 458 nm (several)	1 mW - 150 W	Continuous and pulsed modes	Printing technology, pumping laser for dye laser

				stimulation, medicine
Dye laser	Continuous between infrared and ultraviolet (different dyes)	1 mW - 1 W	Continuous and pulsed modes	Dimensional metrology, spectroscopy, medicine

Table 2.1 Types of laser sources - (adapted from Fraunhofer Institut Lasertechnik, 2003)

Some laser applications, such as micromachining or direct ablation of hard materials, need high laser power density (intensity or irradiance) or energy density (fluence), so usually only excimer lasers, which can produce it, are employed (Braun et al, 2000; Ihlemann and Rubahn, 2000; Rizvi and Apte, 2002). Excimer (EXCIted diMER) lasers, invented in 1975, are a family of pulsed lasers with a fast electrical discharge in a high-pressure mixture of a rare gas (krypton, argon or xenon) and a halogen gas (fluorine or hydrogen chloride) as the source of light emission. The particular combination of rare gas and halogen determines the output wavelength.

The laser source employed determines the wavelength, spot size (i.e. the minimum diameter of the focused laser beam), average beam intensity and pulse duration that can be achieved. These parameters all affect the way in which the laser interacts with the material being processed.

There are three types of interaction between laser and material: the light can be reflected, transmitted or absorbed. In reality, all three occur to some degree. In order for laser milling to be possible, the material must absorb the laser light. Reflected and transmitted light represents energy that is lost to the manufacturing process. Only absorbed light is used to perform material removal.

2.2.2 Laser wavelength

The most important parameter affecting good material processing is the wavelength of the light used. Different materials absorb light at different parts of the electromagnetic spectrum. It is necessary to choose the correct laser wavelength so absorption of the

photons can occur. On a molecular level, infrared photons, like those emitted from a CO_2 or Nd:YAG laser, interact with materials by influencing the way the electrons vibrate internally. Infrared (IR) photon energies are matched very closely to the quantized vibrational energy levels of some materials. Thus, when absorbed, IR photons cause the electrons to vibrate faster, which in turn generates heat in the lattice and induces melting and evaporation. Ultraviolet (UV) photons, on the other hand, have a much shorter wavelength and therefore higher photon energy. Consequently, with certain materials, UV photons can break electronic bonds directly and therefore the material removal mechanism is primarily direct sublimation via plasma formation rather than through melting and evaporation.

2.2.3 Laser beam intensity

Table 2.1 gives typical values for the output power of the different laser sources. However, in laser milling, a more important characteristic is laser beam intensity.

The laser intensity (Wcm^{-2}) is defined as the peak power (W) divided by the focal spot area (cm^2), and the peak power (W) is computed as the pulse energy (J) divided by pulse duration (s). The peak power must be large enough to vaporise the material in the laser beam spot. For each material, there exists a threshold value of laser beam intensity below which no melting or evaporation will occur (see Figure 2.3). For example, for copper if the laser beam intensity is below 4.3×10^9 Wcm^{-2}, the target surface will remain below the melting point and no material removal will occur (Jandeleit, 1998). In order to heat the surface region of the material sufficiently so that melting and/or evaporation can occur, a higher power density is required.

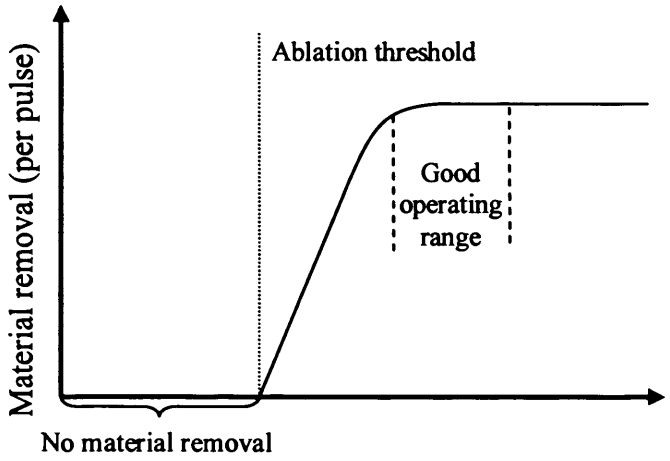

Figure 2.3 Threshold nature of the laser material removal

2.2.4 Laser pulse length

Clearly, an influential characteristic in laser-material interaction is the laser pulse length. There are two major considerations: laser pulse energy and heat diffusion time. Generally, for a given amount of energy, the shorter the pulse is, the higher the peak power delivered to the target will be.

Once applied, the heat energy does not stay localised at the point where it was initially deposited. The heat diffusion time is the time required for a given amount of energy to dissipate into the surrounding material and is specific for that material. Depending on the heat diffusion time of the material, the laser pulse duration can be divided into two time regimes: long and ultrafast. Long-pulse lasers are lasers with a pulse duration longer than 10 picoseconds. These are the most widely used commercial lasers in industry today. Ultrafast, or ultrashort-pulse, lasers have pulses much shorter than 10 picoseconds – usually in the femtosecond range (Harzic et al, 2005).

In the long-pulse regime, the heat deposited in the substrate diffuses away within the pulse duration. This has a detrimental effect on the quality of the machining, because heat diffusion reduces the efficiency of the laser machining process, through draining energy away from the work spot – energy that would otherwise go into removing material. As a result, the temperature at the focal spot can reach a working level of not much above the melting point of the material. The molten material produced is then ejected away from the work zone by vapour and plasma pressure in the form of

drops. These drops fall back onto the surface and create debris, which spoil the quality of the machined surface.

Another negative effect of long-pulse machining is the formation of a heat-affected zone (HAZ). The heat energy that dissipates into the surrounding material can produce a neighbouring zone of mechanical stresses and microcracks. A closely associated phenomenon is the formation of a recast layer around the work spot. This recast layer is made up of resolidified material that often has physical characteristics different from those of the unmelted material. The recast layer usually has to be removed in post-process cleaning.

In recent years, an alternative to long-pulse machining is being developed. In the ultrafast regime, the laser pulses are so short that the heat energy deposited by the laser into the material does not have time to dissipate into the surrounding material. Therefore, all the energy is used efficiently for heating the material well beyond the evaporation point into the plasma formation state (Petzoldt et al, 1996). The plasma expands outward from the surface in a plume of electrons and highly ionised atoms. Consequently, there are no droplets that solidify onto the surrounding material. Additionally, since there is no time for the heat to dissipate into the neighbouring material, there is no HAZ.

It is also important to note that when a material is irradiated with ultrafast laser, the penetration depth and, therefore, the interaction volume is generally small, slowing the material removal process (Harzic et al, 2005). As there are no secondary thermal

effects, the result is that much cleaner and more precise processing can be achieved, but at the expense of speed.

2.2.5 Laser spot size

In laser milling, when the objective is to manufacture the smallest possible feature, it is important to be able to focus the laser beam down to the smallest spot size. The latter depends on several factors but, typically, the smallest spot diameter that can be obtained is about half the wavelength of the light used (Madou, 2001).

However, lasers with ultrashort pulses can create features that are substantially smaller than the laser spot size (Hellrung, 1999). For example, Pronko et al. (1995) have produced holes with a diameter of 300 nm whereas the laser spot size used was of the order of 3 μm. Given that laser beam intensity distribution is Gaussian, with a maximum intensity in the centre of the beam, one can adjust the beam so that only the intensity in its central region is above the threshold for the given material (see Figure 2.4). In this way, material will be removed only in a fraction of the beam spot area, resulting in an affected area as small as one-tenth of the size of the spot itself.

As can be seen in Table 2.1, both ultrashort-pulsed lasers and long-pulsed lasers can produce wavelengths of around 0.5 μm and therefore spot sizes of the order of 0.25 μm. However, unlike the case of ultrafast lasers, with long-pulsed lasers the smallest pit diameter that can be achieved is much larger than the spot size (in the order of 10 μm). This is due to the aforementioned thermal nature of the laser-material interaction and heat diffusion into the surrounding material.

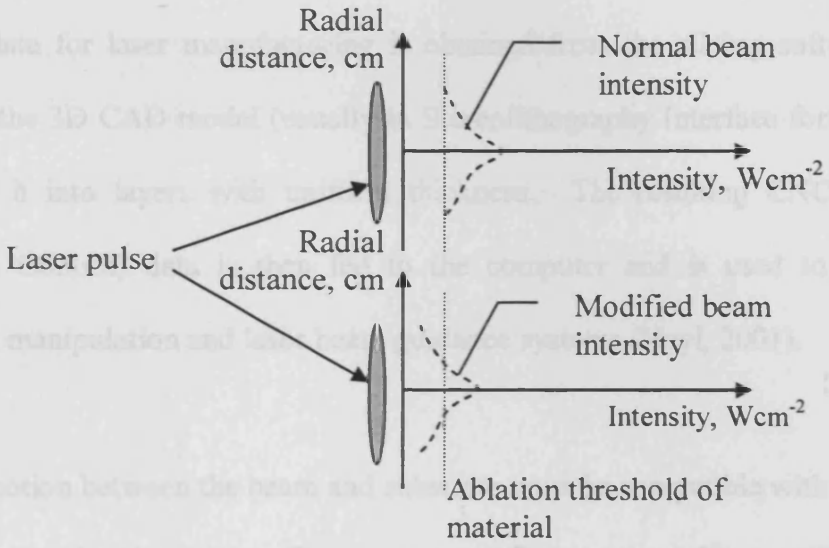

Figure 2.4 Creating sub-spot size features by adjusting the laser beam intensity

2.3 Laser milling system

A laser milling system generally consists of five main components: a laser source, a means of positioning the workpiece, a system for viewing the work surface, a computer to provide control and synchronisation of the laser beam and workpiece positioning, and software for slicing the 3D CAD model of the workpiece and for interfacing with the CAD (Computer Aided Design) package. The NC (Numerical Control) data for laser manufacturing is obtained from the slicing software, which processes the 3D CAD model (usually in Stereolithography Interface format or STL) by dicing it into layers with uniform thickness. The resulting CNC (Computer Numerical Control) data is then fed to the computer and is used to control the workpiece manipulation and laser beam guidance systems (Heyl, 2001).

Relative motion between the beam and substrate must be compatible with the required processing speed and precision. There are two different types of laser milling machine according to the relative movement of the laser beam and the workpiece: a fixed laser beam and a CNC positioning table (Heyl, 2001) or a scanning laser beam and computer-controlled focusing (Pham, 2002). In the first type, the laser beam spot is fixed and relative motion is achieved by a conventional CNC milling platform. The second type was developed later and offers higher scanning speeds and increased productivity. To scan the work surface the laser spot is moved in the slice plane by a pair of computer-controlled mirrors and focusing is achieved through a movable lens. The workpiece, more specifically the slice plane, is positioned in the laser focus plane by one of the machine axes.

The purpose of the work surface viewing system is twofold. First, it acts as an inspection tool enabling the evaluation of the progress of the milling operation. Second, it allows accurate positioning of the workpiece during setting up (Heyl, 2001).

2.4 Laser milling machine

The laser milling machine utilised in this work is called the DML 40SI, and was the first commercially available system of its kind. The system was first introduced in 1999 and is still one of the few laser milling systems available on the manufacturing market. The full technical information on the DML40SI is provided in Appendix A.

2.4.1 Machine layout

The laser milling system (see Figure 2.5) utilised was first introduced in 1999 and is still one of the few commercially available machines of its type in the world. It is equipped with an Nd:YAG laser with an operational wavelength of 1064 nm. A Q-Switch device enables the laser to operate in the pulsed mode. The pulse duration is in the microsecond range and the pulse frequency can be between 0.1 and 50 kHz (Lasertech GmbH, 1999).

The system employs a scanning laser beam. Two computer-controlled galvanometer mirrors move the laser beam spot, thus allowing the uppermost plane of the substrate

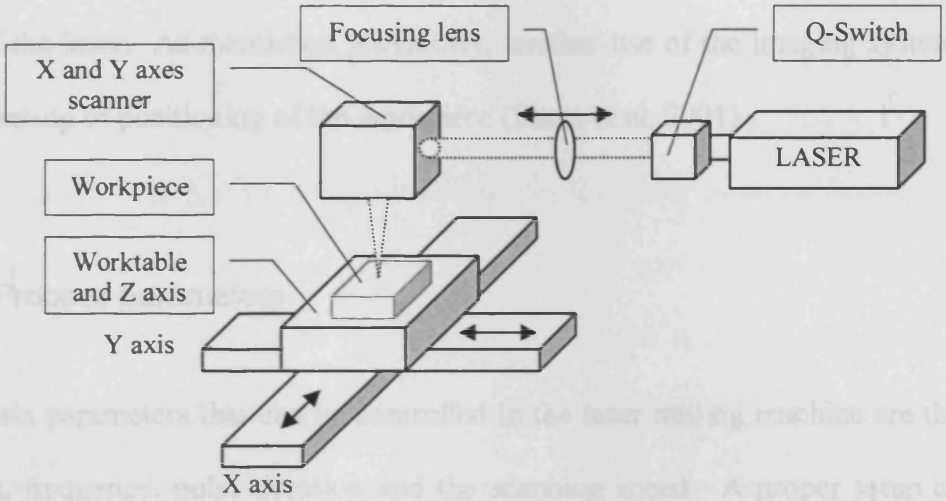

Figure 2.5 Schematic diagram of the employed laser milling system

to be scanned. This plane is brought into position by an NC table, so that it is inside the focal plane of the laser beam. A lens enables the beam to remain focused on the workpiece surface when machining vertical walls.

A video imaging system is provided, that can be employed to assess the progress of the machining operation, but it is not possible to do this while material is being removed, because during inspection the workpiece has to be taken out of the work area of the laser. As mentioned previously, another use of the imaging system is for initial set-up or positioning of the workpiece (Pham et al, 2001).

2.4.2 Process parameters

The main parameters that can be controlled in the laser milling machine are the lamp current, frequency, pulse duration and the scanning speed. A proper setup of these parameters is very important for a stable material removal process and is highly dependent on the target material. Since the laser pulse length was discussed earlier in this chapter, now we will take a closer look at the rest of the parameters.

2.4.2.1 Laser lamp current

The lamp current is the process parameter directly controlling the power that is delivered to the workpiece. It regulates the electric current that is going through the laser flashlamp and therefore the amount of energy that is contained in a single laser pulse. This is the parameter that is most influential on the material removal process, because the process exhibits threshold nature (see Figure 2.3) and a stable process

requires a constant layer thickness. That is the reason for the system have a built-in online layer thickness control.

The layer thickness control system is based on a feedback signal from a precise touch probe, that measures the material removed after a pre-set number of layers (usually 4 layers). The control then makes a decision based on that measurement to increase or decrease the laser current. The z-axis accuracy of the machine is highly dependable on the settings for this control system. There are two drawbacks of the system. First, in order for the touch probe to take a measurement, the workpiece has to be taken out of the laser machining area, thus interrupting the machining process. Second, the size of the touch probe limits its use in the micro feature applications. For the probe to reach the bottom surface of the structure there has to be enough lateral space so that the probe does not get in contact with the walls of the structure. If it does it will either produce an incorrect depth measurement, or even damage the feature.

Nowadays, a new in-process control system is being introduced, that does not require the interruption of the process. The new system is based on an optical sensor located in the path of the laser beam, and measures the distance to the target. This control loop operates on the same strategy as the touch probe, i.e. takes readings every given number of layers, and corrects the laser lamp current. Due to the optical measurement type, this control system proves not to be as accurate as the tactile device. Therefore, a combination of the two control loops is establishing as the most time and cost efficient option. The combination control system functions as usual with the optical sensor providing the in-process measurements every 4 layers. Then the touch probe takes measurements at a longer interval, i.e. every 16 layers. This superseding

measurement is used to correct the error of the optical sensor and thus improve the depth accuracy obtained from the laser milling process. Depending on the material and the settings of the laser milling process, the depth accuracy of laser milling is ± 20 μm.

Although, the laser lamp current is the most influential parameter for the material removal process, without the pulse frequency and the scanning speed there will be no laser milling.

2.4.2.2 Pulse frequency and scanning speed

The pulse frequency [kHz] and the scanning speed, as a combination, can affect the surface roughness, material removal and the overall process performance. The parameters work as a combination, because the ratio scanning speed V to pulse frequency f gives the distance between two neighbouring craters.

$$\frac{V}{f} = d \qquad \text{Eq. 2.1}$$

The distance between two neighbouring craters is usually set to 10 μm (Lasertech GmbH, 1999).

2.4.3 Slicing software and major parameters

Laser milling removes material in a layer by layer fashion. Each layer has a uniform thickness, typically 2 μm, and is machined by the laser beam traversing the topmost surface of the target. LpsWin is the software that is provided for machining data preparation and laser parameters setup. The software requires as an input a 3D closed volume that represents the material to be removed. The 3D model is usually created in a CAD package, such as Pro/Engineer, that can export it in STL format. The LpsWin is used to slice the 3D model into 2D layers as shown on Figure 2.6. A single layer is built from two different types of laser beam paths (see Figure 2.7). The first is the border cuts, which follow the outline of the geometry, and in reality constructs the outer walls of the geometry. The user can set the number of laser passes that form the border cuts. There is an option in the LpsWin software, that enables the users to apply two or more different laser parameters to the border cut, for achieving better wall quality.

The second type of laser beam path is the hatching. It is usually responsible for removing the bulk of the material. The key parameter for both border cuts and hatching is the step-over, which is the distance between two neighbouring laser beam traverses. For best surface quality, it is usually set to be equal to the distance between two neighbouring laser craters, that is defined by the scanning speed and the laser pulse frequency. Using different values will normally result in a variable surface topography, e.g. formation of a groove along the laser beam path.

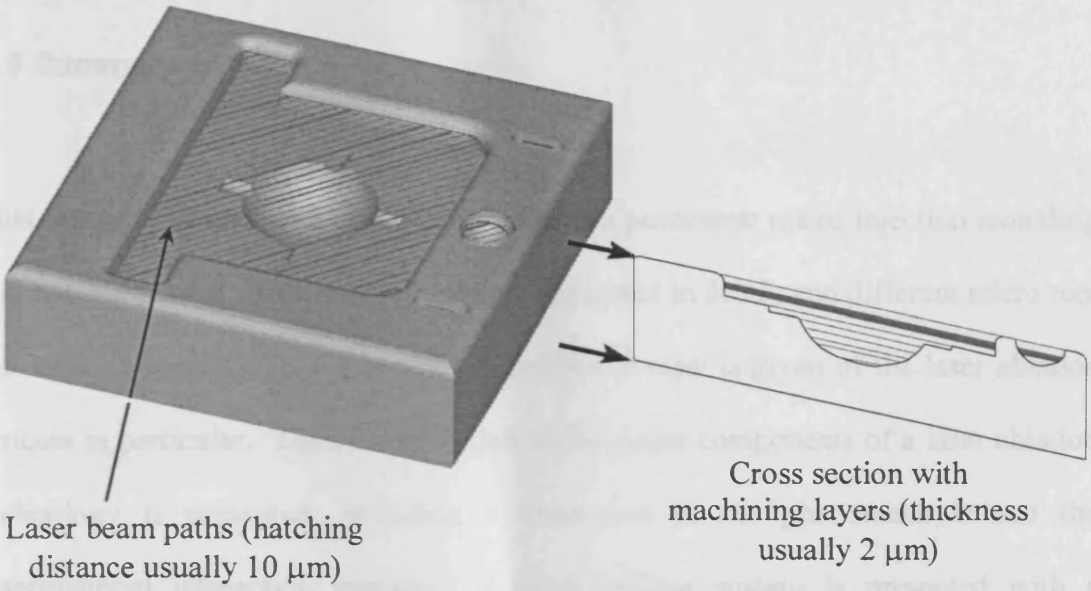

Figure 2.6 Slicing technique for laser milling

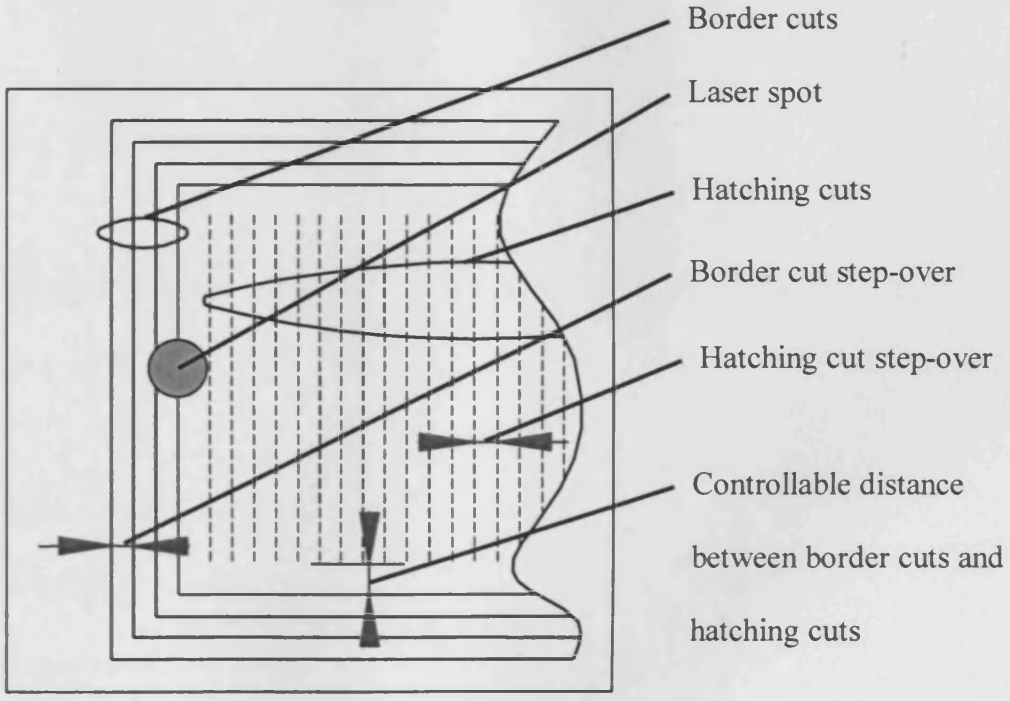

Figure 2.7 Single slice formation

2.5 Summary

This chapter has reviewed two micro fabrication processes: micro injection moulding and hot embossing. Both technologies are explained in detail, and different micro tool fabrication processes are discussed. A detailed review is given of the laser ablation process in particular. Then a description of the major components of a laser ablation technology is presented, including a discussion of the phenomena behind the laser/material interaction process. A laser milling system is presented with a summary of the most important process parameters.

Chapter 3 Investigation of laser milling characteristics

This Chapter introduces a set of process characteristics that define laser milling as a manufacturing process of micro tools. The investigation aims to establish the suitability of the laser milling process by a set of experiments and improve on the process characteristics where possible. These process characteristics are surface finish, aspect ratio, dimensional accuracy and minimum feature size.

3.1 Surface finish

Surface finish is an important aspect of the tool manufacturing industry, particularly with the current trend towards miniaturisation of consumer products. In the manufacture of microtools, surface roughness is much more crucial than normal, because the roughness can frequently be comparable to the feature sizes.

It is expected that the surface roughness is affected by the following three laser milling variables:

- *Laser lamp current*
- *Scanning speed*
- *Laser pulse frequency*

Laser power is relative to the electric current going through the laser flashlamp and signifies the amount of energy that is contained in a single laser pulse. The laser

frequency gives the repetition rate of laser pulses, and the scanning speed is the speed with which the laser spot travels on the target surface. The relationship between the frequency and the scanning speed defines the distance between the centres of two neighbouring laser craters. During planning for the experiment, it became clear that the relationship between any single variable and the resulting surface finish could not be identified, because the proposed test variables are not independent within the material removal process. In order for the laser milling machine to achieve a stable removal process, a constant layer thickness value of 2 μm is required. It was found that while applying a combination of values for the different variables, this layer thickness could not be maintained. Thus a test plan was proposed where five different sets of effective values were identified, covering the complete range for each factor. Each set of value ensures uniform layer absorption therefore a constant removal of the material.

One laser milling parameter, the pulse duration, is omitted from this test, although it is influential on the removal process and hence on the roughness. During the experiment the laser pulse duration is kept constant at 10 μs. This is due to the fact that decreasing the pulse duration leads to a decrease in the layer thickness, for example if at 10 μs the layer thickness is around the 2 μm, a pulse duration of 2 μs will produce a layer thickness under 1 μm. This contravenes with the layer thickness set for the experiment.

As a result, only a general relationship between a set of values for the three factors and the surface finish can be identified. Table 3.1 gives the five sets that were used in the experiment.

3.1.1 Experimental procedure

For the surface finish test, a straightforward geometry was used: a square with a pre-defined size. The chosen size will depend on the requirements of the roughness measuring equipment.

In order to avoid any interference from the texturing of the test surface, the test piece was prepared in advance with its test surface polished to under R_a = 0.2 μm. The measurements of the surface finish were to be made using contact surface roughness measurement equipment (SJ-201 Roughness Tester), which requires a standardised minimum measuring distance depending on the expected roughness. Thus for the expected roughness of 2 μm, the recommended measuring distance is 8 mm. This provides the minimum lateral size of the pocket to be machined. Given that the test workpiece was polished, the depth of the feature was chosen to be 50 μm, giving a total of 25 layers to be machined.

In normal working settings, the best surface finish is achieved with machining each separate layer at a random hatching angle (see Figure 2.6). In order to obtain a true representation of the attainable surface finish, throughout the experiment the scanning direction of the laser beam will be restricted to only *x-* and *y-axis*. This means that one layer will be machined with the laser scanning in the *x-axis* direction and at the end, start the next layer in the *y-axis*.

Test	*I*, %	*f*, kHz	*V*, mm/s
	90	45	400
	86	30	300
	82	20	200
	76	13	150
	71.5	9	100

Table 3.1 Experiment sets for the three factors

For each test sample, a total of 4 measurements of the surface roughness will be made, split in two groups at 90° angle to each other. This way, the influence of the scanning direction of the laser beam will be estimated.

3.1.2 Results

The experiment was carried out according to the prepared plan. All 5 tests were machined on the same workpiece, and a total of 25 surface roughness measurements were made. Table 3.2 gives the results of the roughness measurements in both *x*- and *y*- directions. Notice that test 3 has 3 measurements produced in the *x-axis*. This was called for by the considerable difference in the results of the two previous measurements of the same test. All other measurement pairs are within a 50 nm or less of each other, while the difference in the first two measurements of the test 3 are approximately 180 nm apart.

The lowest average result is obtained from test 5 and is just above the 1 μm surface roughness. The lowest single measurement also comes from *test 5* and is R_a = 0.962 μm. The highest average surface roughness is measured on *test 1*, and is over 0.5 microns more.

Test	R_a measurements in x and y, μm					Avg X	Avg Y	R_a avg
	#x1	#x2	#x3*	#y1	#y2			
1	1.442	1.482		1.563	1.594	1.462	1.579	1.520
2	1.094	1.079		1.155	1.160	1.087	1.158	1.122
3	0.977	1.150	1.057	1.176	1.084	1.061	1.130	1.089
4	1.071	1.064		1.132	1.104	1.068	1.118	1.093
5	1.042	0.962		1.032	1.066	1.002	1.049	1.026
					Total Avg	1.136	1.207	1.170

*third measurement of *test 3*;

Table 3.2 Results from the surface finish measurements (R_a)

Figure 3.1 shows the results from the surface roughness measurements against the experiment parameters. It is obvious that the combination of the lower parameter values produces the best result, although if one disregards the lowest and the highest results, the surface roughness seems rather constant around the 1.1 μm value. The following figure (see Figure 3.2) displays the relationship between the laser lamp current and the roughness, and also includes the graphs for the averaged results in the two axes. The difference in the results obtained from the *x*- and *y-axis*, shows that the roughness has a dependency on the hatching direction of the laser beam. For this experiment, a limitation on the cross-hatching was imposed; therefore a random angle hatching should produce even better results (Lasertech GmbH, 1999). The same figure illustrates the relationship of the laser power and the roughness. It becomes obvious that the minor change in the laser power produces a considerable difference in the output roughness. Comparing with the graphs for the laser pulse frequency and the marking speed, Figure 3.3 and Figure 3.4 respectively, it is evident that the same change in the output variable is achieved through great change in the input parameters. It is also worth mentioning again that the results are obtained from a set of parameters and so they provide a limited view of the influence of each parameter on its own. Nevertheless, the results suggest that the lower lamp current, speed, and frequency are more suitable when the surface finish is an issue. This will of course mean longer machining times, so it is a trade-off.

The good surface finish is very important as an attribute of laser milling, if it is to be established as a micro manufacturing process. Further investigation will be carried out through the development of a laser/material interaction model in the next chapter. The next process characteristic to focus on is the aspect ratio.

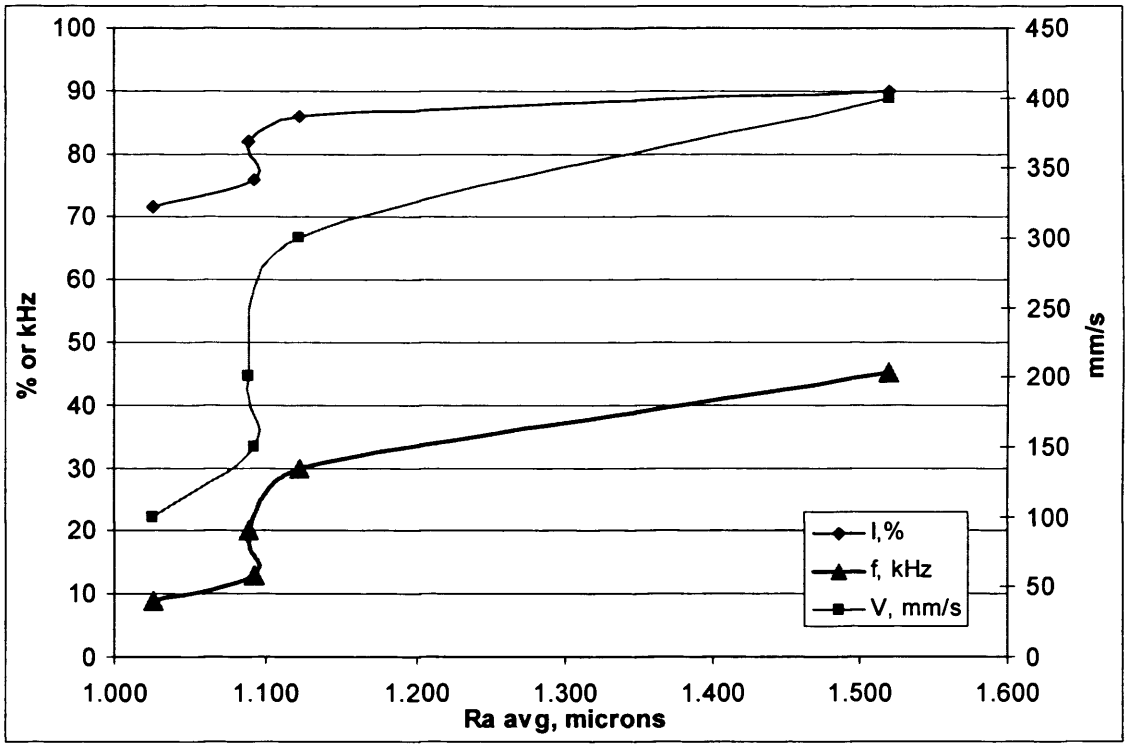

Figure 3.1 Graph of the three parameters I, f and V against the surface roughness R_a

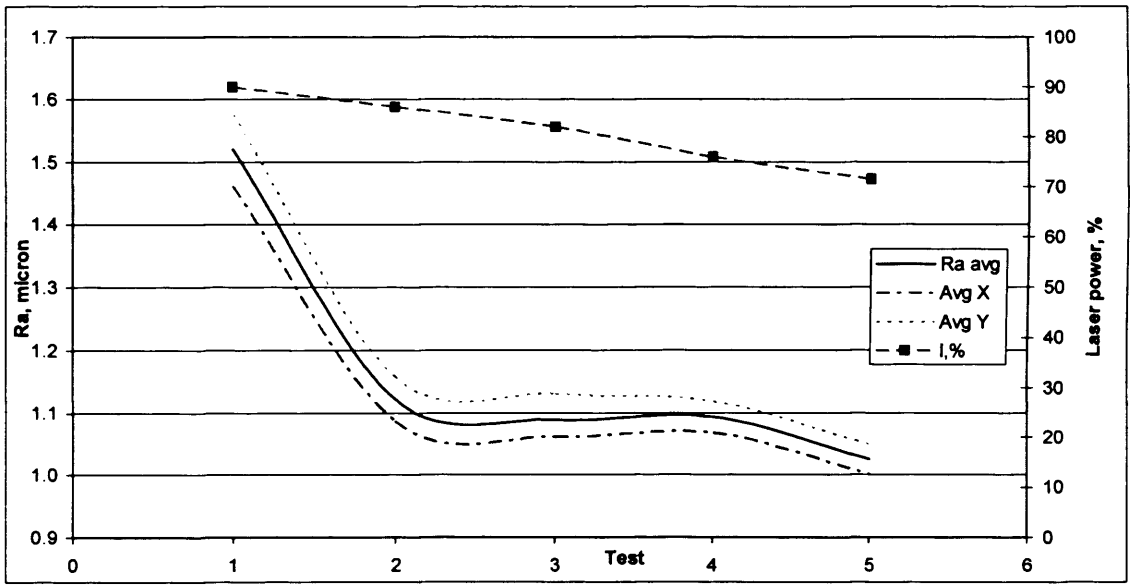

Figure 3.2 The average surface finish from X and Y and overall at the laser powers I used

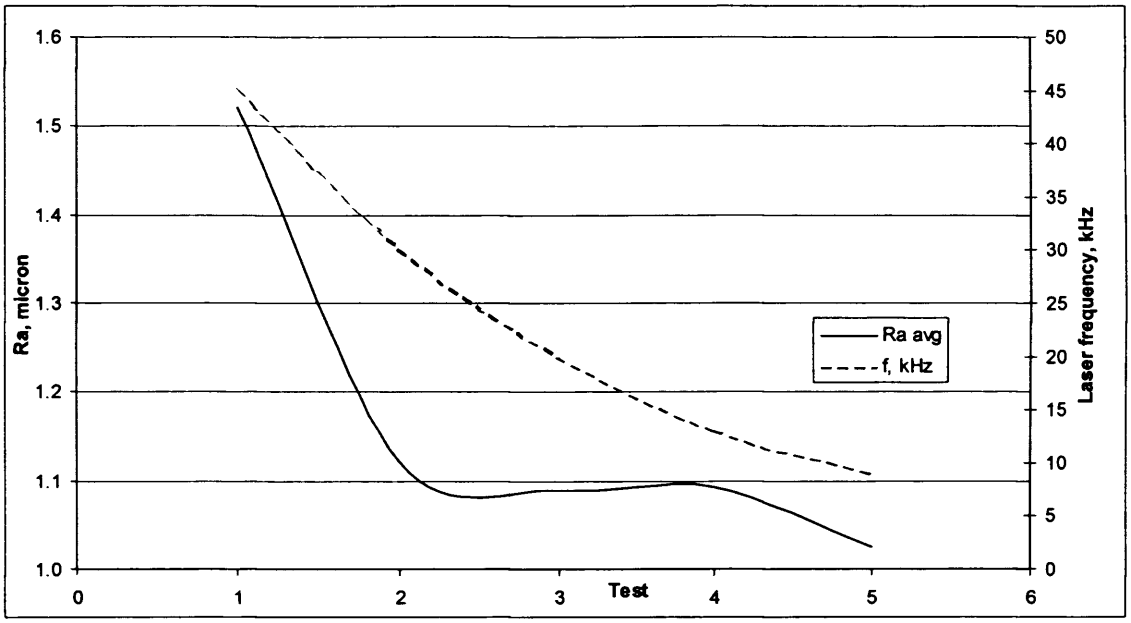

Figure 3.3 Average overall R_a and laser frequency f

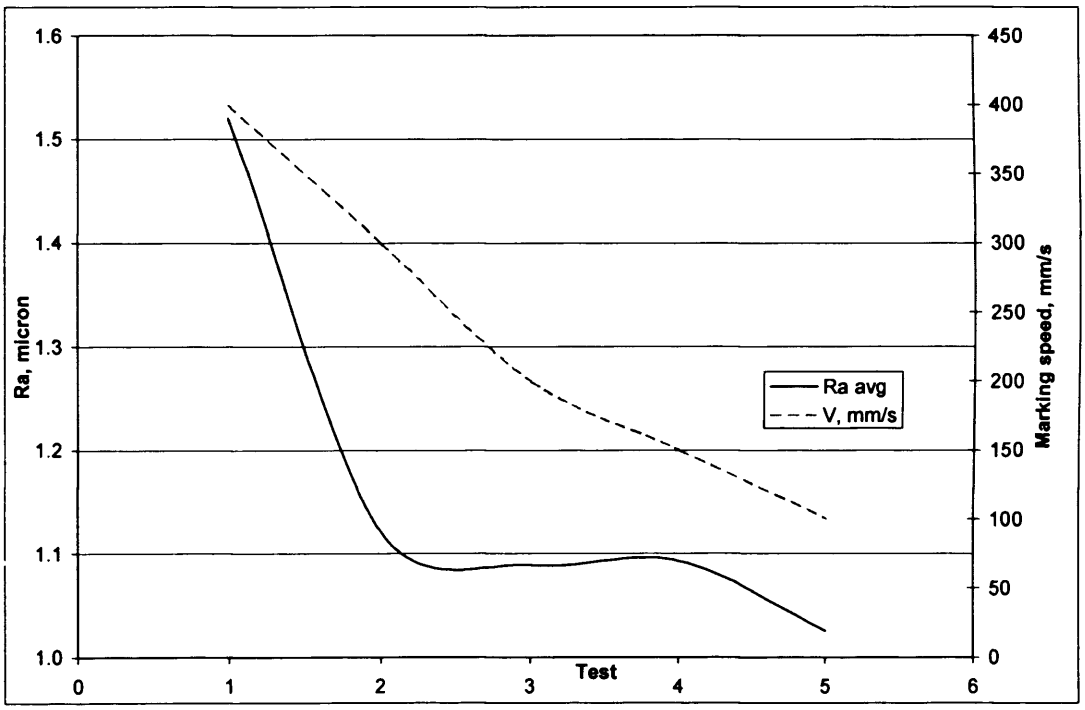

Figure 3.4 Average overall R_a and marking speed V

3.2 Aspect ratio

The definition of aspect ratio is the ratio of height to the width or the gap size of a concave structure. When manufacturing high aspect ratio free-standing structures, i.e. pillars, walls, the requirements to the manufacturing process are different from those raised from a concave geometry. Chang and Kim (2000) investigated the manufacture of high aspect ratio with the use of UV-LIGA process. They managed to fabricate structures from 5 to 130 μm with an aspect ratio for a gap equal to 25.

Since almost all manufacturing processes utilise some sort of tool, the aspect ratio of the concave geometry causes significant considerations to be examined, such as tool diameter and length. Given that laser milling makes use of a non-contact "tool", the aspect ratio is associated with another obstacle for the process: the manufacturing of vertical walls. Achieving a plane wall that is parallel to the laser *z-axis* is an issue for laser milling. This is due to the high dependence of the material removal process on the size of the laser spot, which enlarges when the beam is located close to a plane surface parallel to the laser axis (Pham et al, 2002). As a result of this all laser milled walls have draft angle. The draft angle is typically in the order of 5 to 10 degrees, and is directly proportional to the aspect ratio of the microstructure.

The successful manufacturing of vertical wall has been achieved through the use of an angular offset of the laser beam when machining the border cuts along the wall (see Figure 2.7 and Figure 3.5). Also it is possible to apply different set of laser

parameters for these cuts, such as laser power, scanning speed and frequency, but for investigating the actual influence of the angles, it will be neglected in this study. The use of only one set of parameters will be employed.

3.2.1 Definition of laser milling parameters

There are two parameters in the laser milling process that are expected to influence the aspect ratio:

- Minimum approach angle
- Maximum approach angle

The two approach angles refer to the minimum and maximum angles that limit the location of the laser beam during vertical walls manufacturing, and they lie in the vertical plane normal to the given wall (see Figure 3.5). During vertical wall machining, the laser axis can be positioned anywhere within the range specified by the two approach angles.

3.2.2 Experimental procedure

The structure to be used for aspect ratio test is a simple rectangular shape (pocket) as shown in Figure 3.6.

The proposed depths to be tested are restricted because of the manufacturer's specification of the machine: the manufacturer has listed a maximum of 2.5 aspect ratio. The following dimensions will be used for the test geometry:

- $w = 0.4$ mm
- $l = 1.2$ mm (length of the pocket)

The test parameter d (depth) will change in the range from 0.4 to 1.2 mm.

It was decided that the approach angle parameter would be divided into 6 value ranges (Minimum angle – maximum angle) as follows:

1. 12° – 13°
2. 13° – 14°
3. 14° – 15°
4. 15° – 16°
5. 16° – 17°
6. 17° – 18°

The upper and lower limits are also extracted from the machine specifications (LaserTech GmbH, 1999).

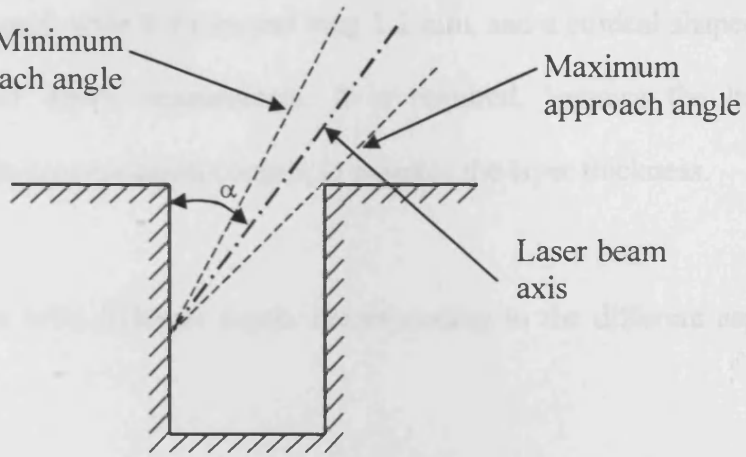

Figure 3.5 Laser approach angle

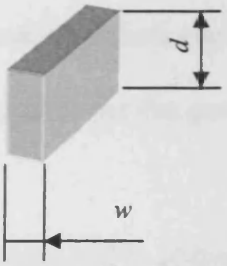

Figure 3.6 Aspect ratio test geometry (the figure shows the material to be removed) - d – depth (height), w – width

In order to shorten the manufacturing time, geometry with 6 different aspect ratio structures is proposed (See Figure 3.7). The experiment geometry consists of 6 separate pockets, each wide 0.4 mm and long 1.2 mm, and a conical shaped structure, which is used for depth measurement. It is required, because the laser-milling machine uses an in-process depth control, to monitor the layer thickness.

The 6 pockets are with different depth, corresponding to the different aspect ratios, see Table 3.3.

Thus for each range of the approach angle, a single experiment geometry has to be manufactured. However before that the geometry has to be sliced with *LpsWin* (company software). Since *LpsWin* is used to introduce the different slicing parameters, including the approach angle, 6 different control files (*.l4d) have to be produced for each of the different approach angle ranges. This control file (*.l4d) is used from the DML 40 SI to manufacture the geometry.

One option that is available in the *LpsWin* software is the possibility to calculate and visualise the collisions of the laser beam with the surfaces describing the geometry. The software is calculating the trajectory of the laser beam, which is constrained by the minimum and maximum approach angle. Taking into account, this trajectory and the laser beam geometry, the software calculates any overlapping or collisions that will occur with the geometry surfaces, and produces a new surface representing these collisions. Figure 3.8 shows the result of such collision calculation and the red areas on the walls of the pockets show where the laser beam will collide with the walls.

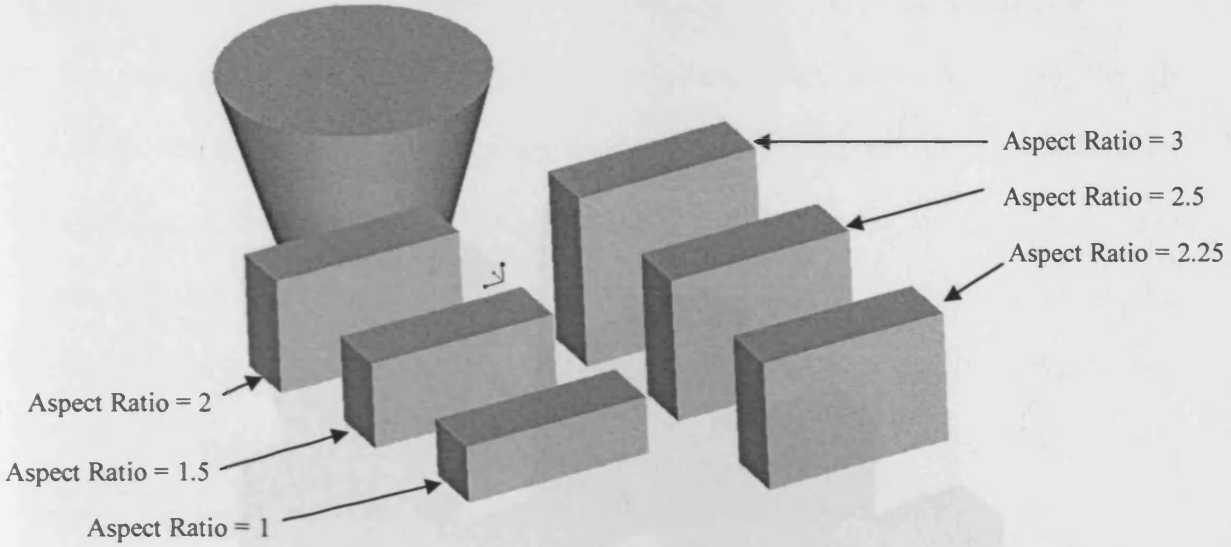

Figure 3.7 Solid model of the material to be removed

#	Aspect ratio	Depth, mm
1.	1.00	0.4
2.	1.50	0.6
3.	2.00	0.8
4.	2.25	0.9
5.	2.50	1.0
6.	3.00	1.2

Table 3.3 Depth corresponding to the aspect ratio

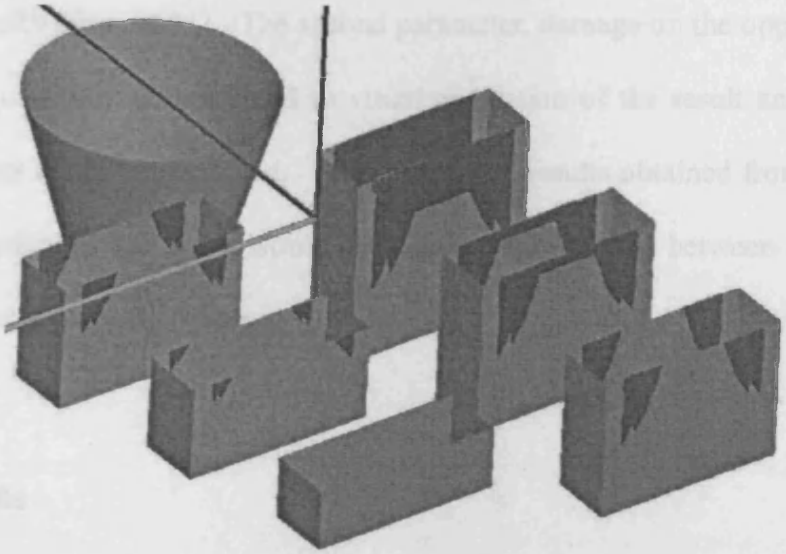

Figure 3.8 Collision calculation result (LpsWin software)

(min. approach angle = 17°, max. approach angle = 18°)

There are two output parameters that will be evaluated at the end of the experiment: the actual achieved depth and damage on the walls of the feature, as predicted from the software check. The machined depth will also give the actual depth accuracy of the process. Due to the small size of the features and without destroying the test results, the first output parameter can only be measured with the optical measurement system (QuickVision, 2001). The second parameter, damage on the opposite walls of the feature, can only be subjected to visual evaluation of the result and no tangible measurements could be produced. The preliminary results obtained from the *LpsWin* software predicted that there would be a direct relationship between the approach angle and the aspect ratio that can be achieved.

3.2.3 Results

The experiment was carried out according to the laid out plan without any problems. It was clearly visible that all 6 sets of experimental structures are showing some damage on the opposite walls on the high aspect ratio features. The best result was achieved in the first set with undamaged edge up to the feature with an aspect ratio of 2 (see Figure 3.9a). The next feature, with an aspect ratio of 2.25, is already exhibiting some minimal damage. The worst result was obtained, as expected, from the sixth set (see Table 3.3). The minimum aspect ratio that is achieved without any damage is AR = 1.5, while the feature with AR = 2 shows clearly visible marks from the laser beam on both opposite walls (see Figure 3.9b).

It is of great importance, to note that the results from the depth measurements of the experimental structures showed a large error (see Table 3.4). The average depth error

is 0.187 and it does not display any relationship to the depth of the experimental features (see Table 3.5 and Figure 3.10). One possible source of the error, is the optical measuring equipment, which use was imposed by the micro sized features. The accuracy of the optical measuring system is highly dependent on the light and reflection from the measured surface.

It was logical to expect that a depth error would increase with the increase in feature depth, but as illustrated in Figure 3.10 the error is almost constant through the whole depth range. From the same figure, it is obvious that the error is also independent from the test parameter, otherwise it would have invalidated the results of the experiment. On the other hand, the depth reference feature (see Figure 3.7), that forms a part of each experimental set, does not display the same sizeable error as the rest of the set (see Table 3.4). This is due to the fact that the in-process depth control uses a touch probe to measure the depth at the bottom of this reference point after a set amount of layers, and changes the laser power correspondingly. Thus the high depth accuracy is achieved at the reference feature, and at the rest of the features the accuracy is reduced. This makes the use of a separate reference features unsuitable for the laser milling process.

3.2.4 Discussion

Overall the experiment produced the expected results, with the exception of the error in the laser machining depth that occurred. The aspect ratio achieved with only minimum amount of damage was AR = 2.25 and the result was close to the predicted

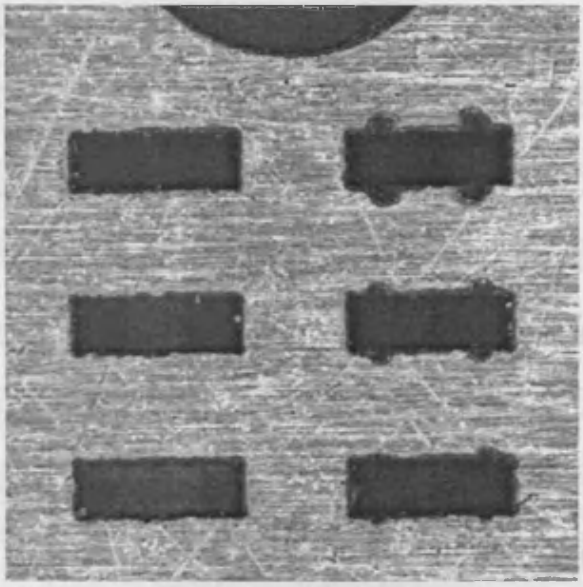

(a).

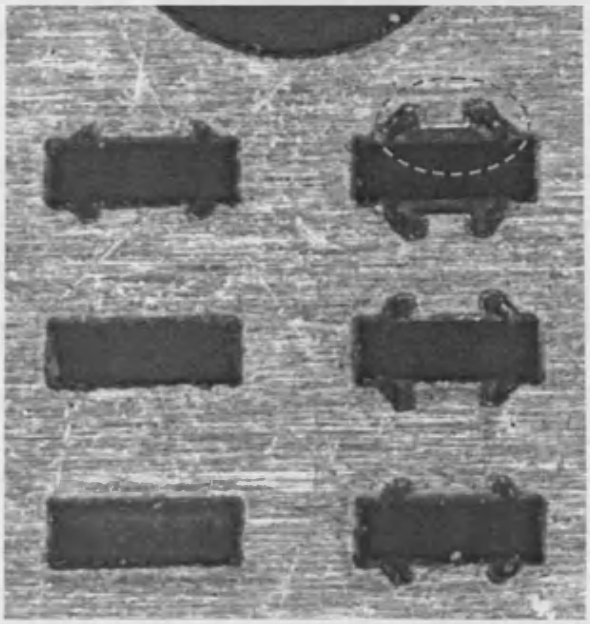

(b).

Figure 3.9 Top view of AR test sets :

(a) with min. approach angle = 12°, max. approach angle = 13°, (b) with min. approach angle = 17°, max. approach angle = 18°

Nominal	1st set		2nd set		3rd set		4th set		5th set		6th set	
mm	D, mm	AR	D, mm	AR	D, mm	AR	D, mm	AR	D, mm	AR	D, mm	AR
0.4	0.589	1.47	0.53	1.33	0.606	1.52	0.59	1.48	0.553	1.38	0.546	1.37
0.6	0.765	1.91	0.784	1.96	0.775	1.94	0.802	2.01	0.765	1.91	0.742	1.86
0.8	1.018*	2.55	0.986	2.47	0.989	2.47	0.993	2.48	1.003	2.51	0.953	2.38
0.9	1.14	2.85	1.138	2.85	1.094	2.74	1.064	2.66	1.107	2.77	1.116	2.79
1	1.227	3.07	1.203	3.01	1.182	2.96	1.171	2.93	1.215	3.04	1.157	2.89
1.2	1.403	3.51	1.381	3.45	1.411	3.53	1.386	3.47	1.359	3.40	1.379	3.45
1.2 Ref	1.208		1.180		1.185		1.189		1.189		1.183	

Table 3.4 Depth measurements of the 6 sets of the aspect ratio experiment

Nom. mm	1st set	2nd set	3rd set	4th set	5th set	6th set	Avg. Error
0.4	0.189	0.130	0.206	0.190	0.153	0.146	0.169
0.6	0.165	0.184	0.175	0.202	0.165	0.142	0.172
0.8	0.218	0.186	0.189	0.193	0.203	0.153	0.190
0.9	0.240	0.238	0.194	0.164	0.207	0.216	0.210
1	0.227	0.203	0.182	0.171	0.215	0.157	0.193
1.2	0.203	0.181	0.211	0.186	0.159	0.179	0.187
Overall Avg.							0.187

Table 3.5 Average depth error [mm] for each nominal depth and average error per set

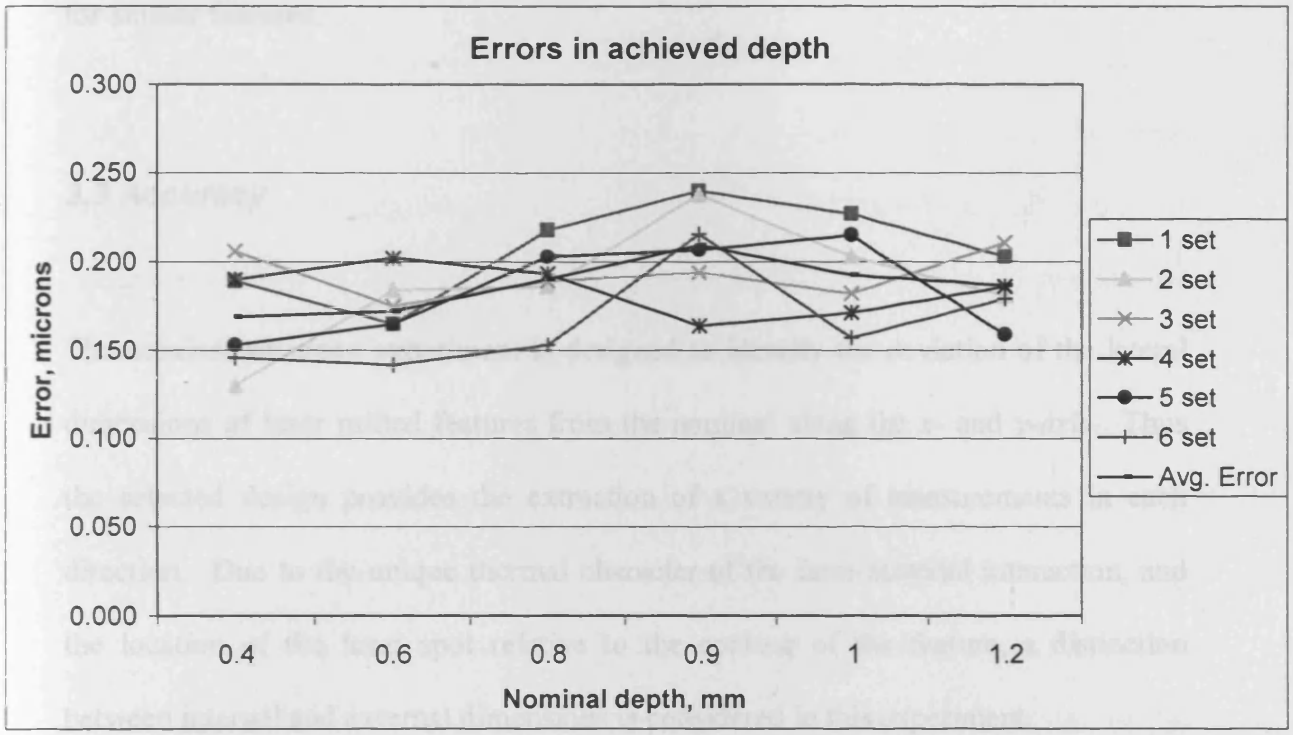

Figure 3.10 Error in achieved depth (measured)

value of 2.5. The influence of the approach angle on the aspect ratio was confirmed, with the best result achieved by the lowest range selected for the experiment. As a conclusion, the laser milling process equipped with the vertical wall machining option is still limited in its capabilities of producing grooves of high aspect ratio. The achieved result is in the low aspect ratio range of the replication process capabilities for similar features.

3.3 Accuracy

The nominal accuracy experiment is designed to identify the deviation of the lateral dimensions of laser milled features from the nominal along the *x*- and *y-axis*. Thus the selected design provides the extraction of a variety of measurements in each direction. Due to the unique thermal character of the laser/material interaction, and the location of the laser spot relative to the contour of the feature, a distinction between internal and external dimensions is considered in this experiment.

This experiment is carried out on two different metals to investigate the influence of the material properties. The two materials selected for the experiment are tooling steel H13 and commercial copper. The selected materials have previously shown a distinctive difference in the response to laser irradiation, and thus a wide range of laser milling parameters are employed in the material removal process. The major difference in the material properties of the two metals is in the thermal conductivity (see Table 3.6). Commercial copper exhibits a thermal conductivity that is 2.5 times higher than that of the tooling steel. Due to the thermal nature of the material removal

process during laser milling, the parameter set-up for the machining of the two materials will be significantly different.

3.3.1 Experimental procedure

The 'nominal accuracy test' measures the deviation of the dimensions of the machined features from the nominal in both x- and y-axes. Hence the workpiece should allow for the extraction of various measurements in these directions. Also, the test geometry should have internal and external dimensions, and so to provide the possibility for analysis of the influence of the effective laser spot relative to the contour of the geometry. Figure 3.11 helps explain the meaning of the dimension types. It shows that for the external dimension, the hatching is performed on the outer side of the contour, thus the laser spot is also located outside. Conversely, positioning the laser spot on the inside of the closed contour forms the internal dimensions. The foundation behind this distinction is that the measured dimensions will depend on the laser/material interaction and any difference between the diameter of the actual laser spot and the assumed diameter will result in a uniform error around the contour. Therefore it is expected that the measured external dimensions will be larger than the nominal; hence, the opposite is anticipated for the internal dimensions.

The final design of the experiment geometry is shown in Figure 3.12. The overall dimensions and designations can be found in Appendix B.

Material properties of:	**Copper**	**H13**	**Units**
Density @ 21°C	8800	7750	kg/m^3
Thermal conductivity @ 21°C	52	17.6	W/mK
Thermal expansion (21 – 93 °C)	17	10.4	$mm/mm/°C \times 10^6$
Specific heat capacity @ 21°C	420	460	J/kgK
Melting point	1300	1700	K
Boiling point	2843	3100	K
Modulus of elasticity @ 21°C	128	207	GPa
Hardness @ 21°C	28	51	Rockwell C

Table 3.6 Physical properties of copper and H13

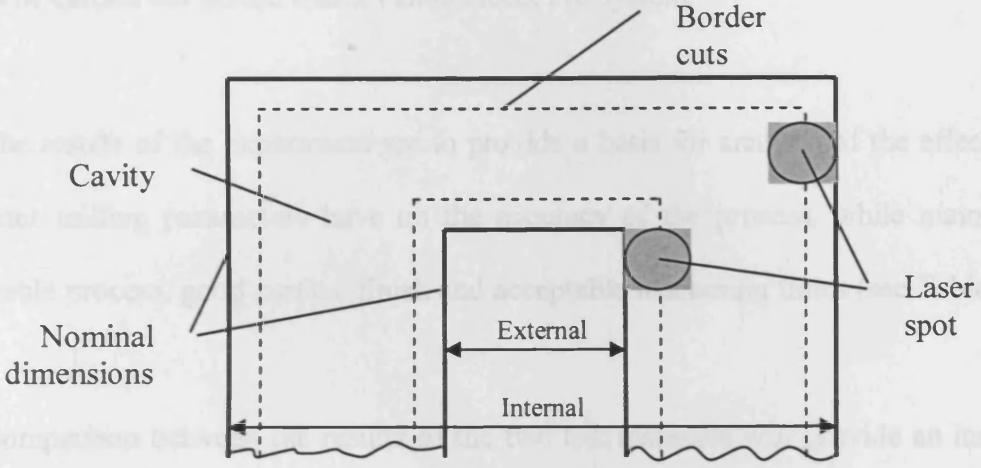

Figure 3.11 Dimension types

Two experimental parts were machined for each of the test materials, with laser milling parameters previously identified as giving best results and with reasonable difference in the laser scanning speeds for the each material (see Table 3.7). The machined parts were to be cleaned in an ultrasound bath, and then the measurements to be carried out on the QuickVision Accel Pro system.

The results of the experiment are to provide a basis for analysis of the effect that the laser milling parameters have on the accuracy of the process, while maintaining a stable process, good surface finish and acceptable machining times (see Table 3.7).

Comparison between the results of the two test materials will provide an insight into the influence that the material properties have on the accuracy of the laser milling process. The results can also highlight the areas, which will need further research for optimising the quality of the laser milling features.

3.3.2 Results

There were two test features machined on each of the test materials. After ultrasound bath cleaning of the samples, measurements in both *x*- and *y*- directions were taken and analysed. The laser milling process settings used to machine the test pieces can be found in Table 3.7.

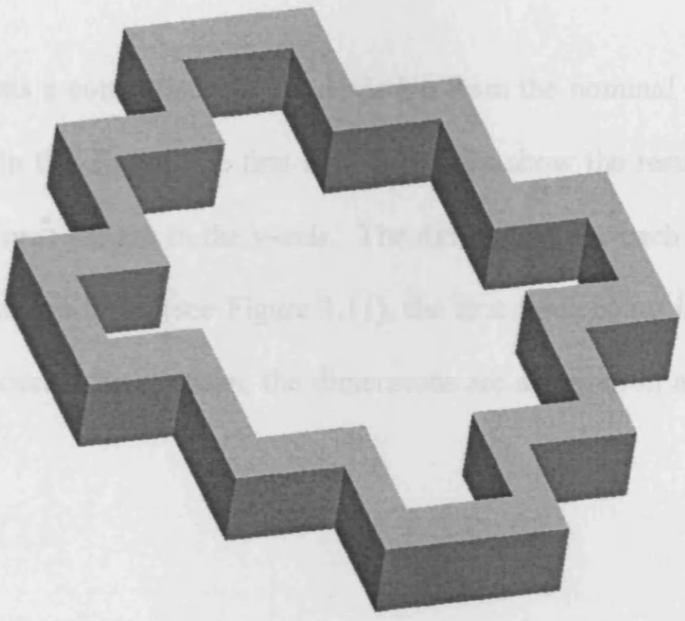

Figure 3.12 CAD model of experiment geometry (material to be removed)

Table 3.8 has the results from the measurements of the four test features. The deviation provided in the table equals the measured value subtracted from the nominal value for the given dimension. Table 3.8 also presents the ISO International Tolerance Grade (IT) for each of the measured values.

Figure 3.13 presents a comparison of the deviation from the nominal dimensions for all test features. In this figure, the first six dimensions show the results from the *x-axis*, whereas the next six are in the *y-axis*. The dimensions for each axis were split into the two dimension types (see Figure 3.11), the first three being internal and the next three - the external. In addition, the dimensions are arranged in ascending order from the nominal.

3.3.3 Discussion

From the results, it is obvious that Copper provides better accuracy than the tooling steel H13. Both copper tests have lower average deviation and the lowest value of 0.026 mm is achieved with the Cu_1 test parameters. Of the H13 tooling steel tests, marginally better result are obtained from the H13_1 parameters, but since the difference is below the accuracy capabilities of the measuring equipment, this result is not significant. Another consideration would be that the feature edges of the H13 were not clearly defined, which led to the accumulation of errors during the measurement of the results. Under the magnification of the measuring equipment,

Test	Laser lamp current, I [%]	Laser pulse frequency, f [kHz]	Scanning speed, V [mm/s]
H13_1	64	30.5	305
H13_2	69	39.2	392
Cu_1	58.7	11.3	113
Cu_2	62.9	15.7	157

Table 3.7 Process parameters for accuracy experiment

Dimension			H13_1		H13_2		Cu_1		Cu_2	
Nominal, mm	Designation	Type*	Deviation, mm	IT grade	Deviation, mm	IT grade	Deviation, mm	IT grade	Deviation, mm	IT grade
X axis										
0.7	D12	I	-0.049	11	-0.049	11	-0.03	10	-0.046	11
2.1	D13	I	-0.055	11	-0.053	11	-0.036	10	-0.047	11
3.3	D11	I	-0.070	11	-0.061	11	-0.046	10	-0.052	11
1.2	d1	E	0.026	9	0.043	11	0.013	8	0.037	10
2.6	d5	E	0.039	10	0.035	10	0.013	8	0.036	10
3.8	d6	E	0.027	9	0.024	9	-0.004	4**	0.034	10
Y axis										
0.6	D10	I	-0.035	10	-0.048	11	-0.031	10	-0.017	9
2.7	d8	I	-0.077	12	-0.064	12	-0.044	11	-0.036	10
4.3	d9	I	-0.071	11	-0.069	11	-0.053	11	-0.052	11
1.4	d2	E	0.025	9	0.041	11	0.016	9	0.022	9
3.4	d3	E	0.019	9	0.032	10	0.011	8	0.021	9
5.0	d4	E	0.028	9	0.023	9	-0.011	8**	-0.016	9**
		Avg	0.043		0.045		0.026		0.034	

*dimension type (see Figure 3.11) **absolute value assumed

Table 3.8 Results from accuracy experiment

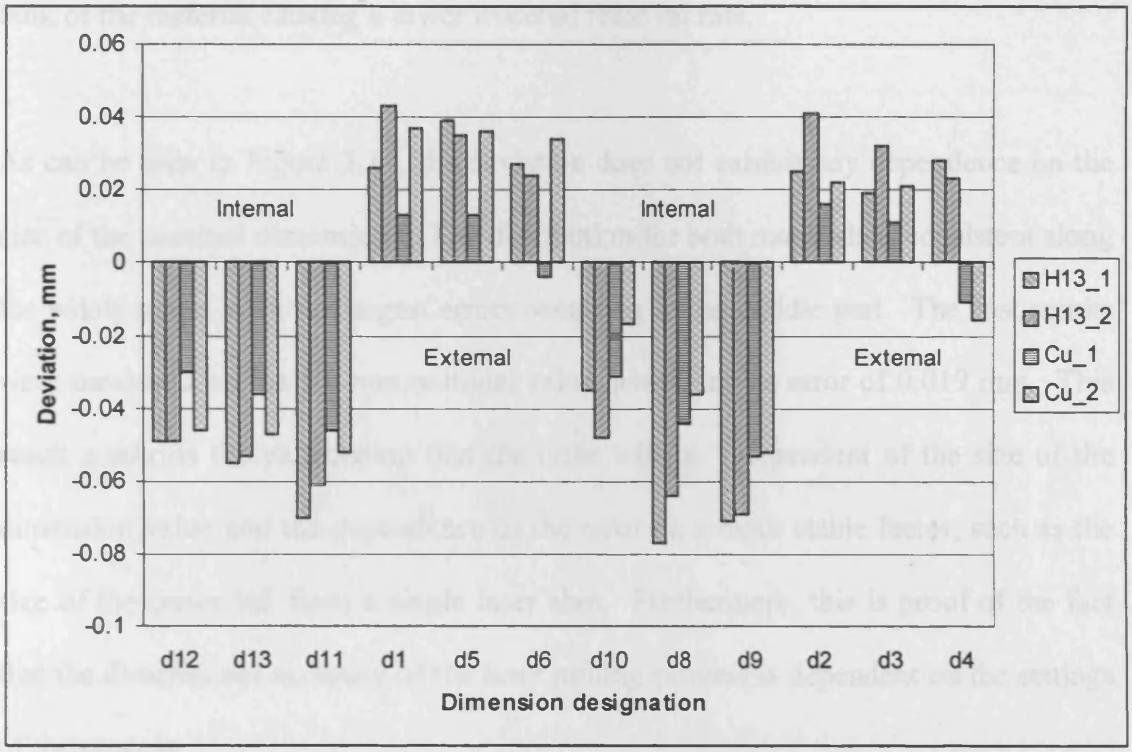

Figure 3.13 Comparison of the deviation from the nominal dimensions for all experiments

H13 displayed a considerable recast layer, larger than copper, which further complicated the process of measuring the actual feature dimensions.

The difference in the accuracy obtained from both materials is largely contributed to the different physical properties, and in particular the thermal properties. Copper has a larger heat conductivity coefficient; therefore more laser power dissipates in the bulk of the material causing a lower material removal rate.

As can be seen in Figure 3.14, the deviation does not exhibit any dependence on the size of the nominal dimensions. The distribution for both materials is consistent along the whole range, with the largest errors occurring in the middle part. The best results were measured on the 5.0 mm nominal value, averaging an error of 0.019 mm. This result confirms the expectation that the error will be independent of the size of the dimension value and the dependence of the error on a more stable factor, such as the size of the crater left from a single laser shot. Furthermore, this is proof of the fact that the dimensional accuracy of the laser milling process is dependent on the settings of the process.

The most significant outcome of the experiment is the different accuracy achieved when machining different materials. The importance comes from the conclusion that just by changing the workpiece material, the accuracy of the laser milling process could be improved. Further investigation is required to widen the scope of workpiece materials.

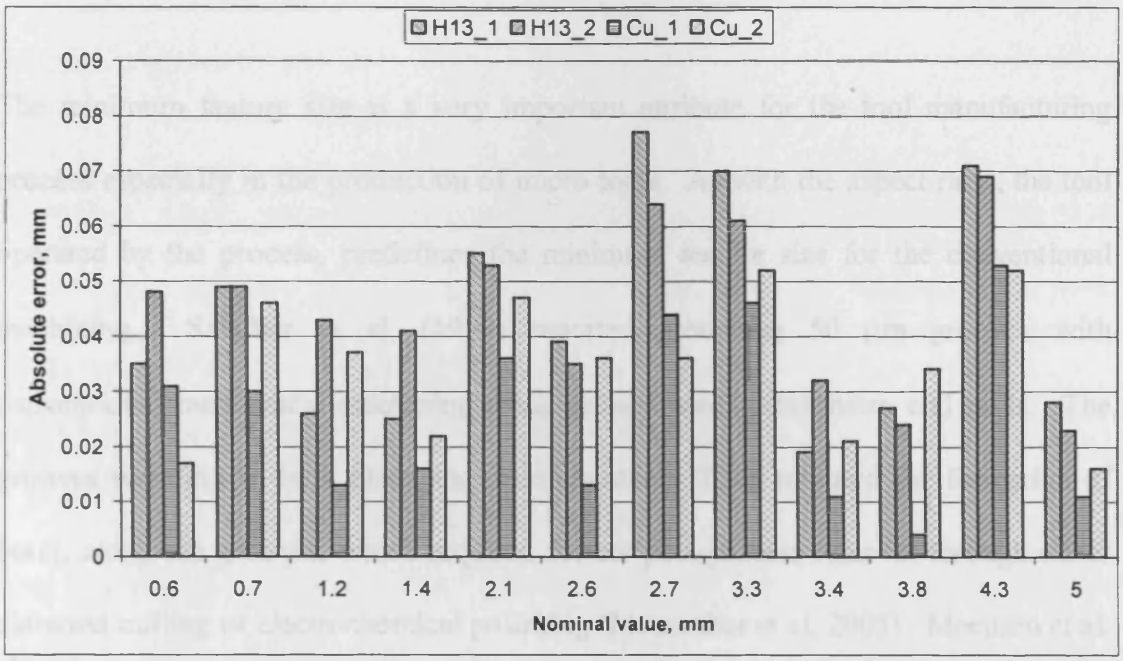

Figure 3.14 Nominal dimension versus absolute error

Secondly, the outcome of the nominal accuracy experiment was better than the manufacturer's specification for the machine. LaserTech GmbH (1999) has specified a 50 μm precision for the system, therefore the result obtained on the H13 workpiece is on average 7 μm better, and the Copper one almost half that – on average 25 μm.

3.4 Minimum feature size

The minimum feature size is a very important attribute for the tool manufacturing process especially in the production of micro tools. As with the aspect ratio, the tool operated by the process, predefines the minimum feature size for the conventional machining. Schaller et al, (1999) reported producing 50 μm grooves with conventional mechanical machining using ground hard metal micro end mills. The grooves were cut in both brass and stainless steel. They reported the formation of burrs, along the grooves, which required further post-process removal through either diamond milling or electrochemical polishing (Mecomber et al, 2005). Meeusen et al. (2001) introduced the micro Wire Electro Discharge Grinding (WEDG) as a micro tool shaping process. They managed to produce micro features that were later polymer replicated, by dressing an electrode down to 30 μm diameter. The paper described the application of WEDG process for producing shaped electrodes for the machining of microstructures. The size of the electrode was the major factor when aiming for the smallest possible size of the features.

3.4.1 Experimental procedure

The study is looking at the minimum feature dimensions, that can be achieved with the laser milling process. General feature types are proposed for this test:

- Groove
- Rib (or wall)

The geometry proposed for the experiment is given in Figure 3.15. The advantages of this type of geometry are:

- With a single test run identify the minimum groove width with relation to a constant size ribs – the proposed test structure has 320, 160, 80 and 40 μm wide groves;
- Constant width walls/ribs of 40 μm;

This experiment will also provide information for the aspect ratio of the convex feature – wall or rib. When machining a free standing feature, such as a wall, without any neighbouring features that could act as obstacles for the tool, a different aspect ratio is generally anticipated. In this situation, other restrictions come into consideration, such as tool/workpiece contact, tool-induced vibrations and the workpiece material properties. Therefore, laser milling being a non-contact process has a distinct advantage. In addition, the vertical walls option was included in the experiment, so as to avoid the formation of a draft angle on the walls of the structure.

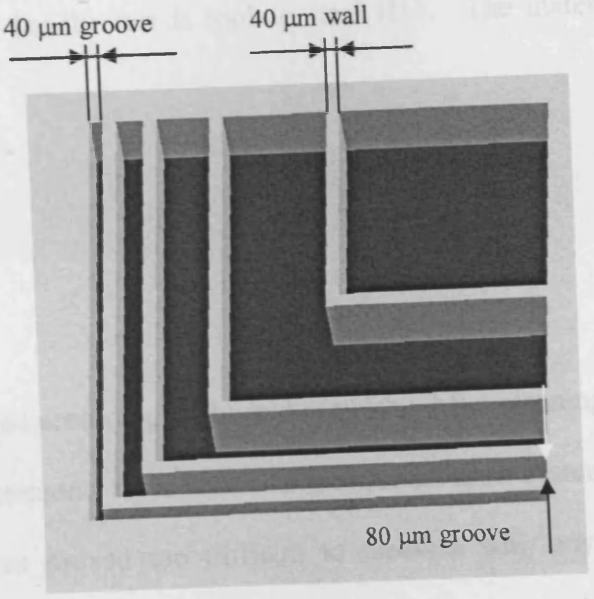

Figure 3.15 CAD model of the resulting geometry

The only variable, expected to have an effect on the minimum feature size is the *diameter of the focused laser beam spot.* It is set by the aperture of the optical train and has only two values 1 and 1.3, where the diameter of the spot is roughly ∅45 and ∅80 μm respectively. Since, we are looking for the minimum the test is carried out with the smallest possible aperture.

The material chosen for the test is tooling steel H13. The material properties are listed in Table 3.6.

3.4.2 Results

The test was executed according to the laid out plan. After cleaning of the workpiece, a number of measurements were taken on the QuickVision system, but the depth of the smallest grooves proved too difficult to measure with any conclusive result. Therefore, the resulting structure was observed and estimates were produced under scanning electron microscope (SEM) (Scanning electron microscopy, 2004). Figure 3.16a shows an overall top view of the fabricated structure, and Figure 3.16b and Figure 3.16c display close-ups of a corner and a wall, respectively, taken with the SEM.

3.4.3 Discussion

From the resulting shape, it is obvious that the microstructure was close to exceeding the capabilities of the process. The 40 μm groove was not machined to the final depth

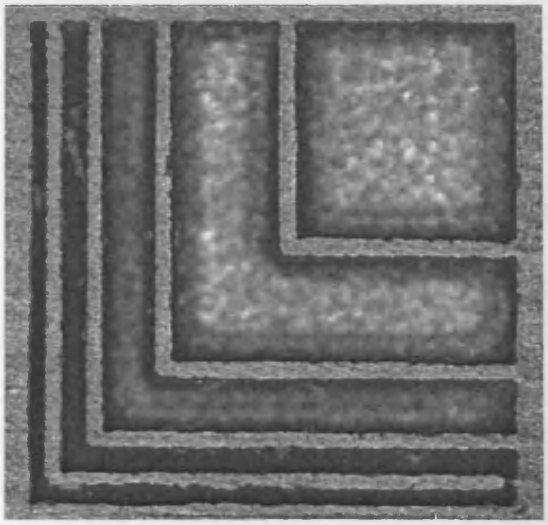

a). Top view

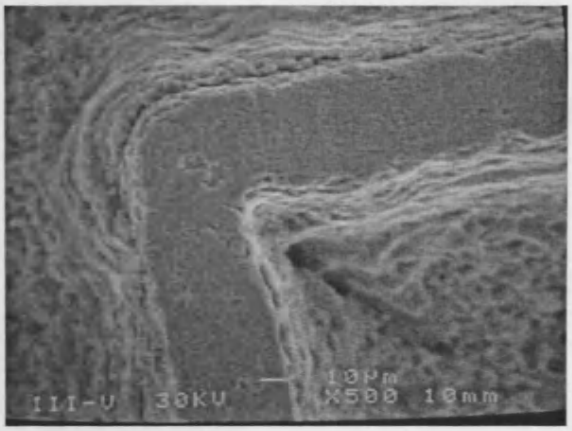

b). Close-up of right-angle corner wall – wall thickness 40 μm (SEM)

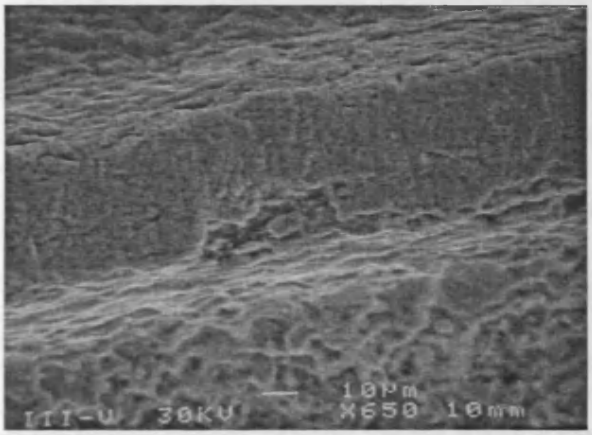

c). close-up of wall segment

Figure 3.16 The resulting geometry for the minimum feature size study

of 120 μm. The achieved depth was difficult to measure because the bottom surface of the groove was not flat. The 80 μm groove was machined to the desired final depth, but there was a rounded corner present in the transition from the walls to the bottom surface.

On the other hand, the 40 μm thick walls are well formed (see Figure 3.16), and with their depth of 120 μm the obtained aspect ratio for a wall was equal to 3.

3.5 Summary

In this chapter, four characteristic features of the laser milling process were investigated: surface finish, aspect ratio, accuracy and minimum feature size.

The best surface roughness that was achieved in the presented experiment was R_a = 1 μm, which was an improvement for the laser milling process, which usually produces R_a = 2 μm. However, the achieved roughness is still high for the replication processes, due to the fact that the polymer replication processes copy the surface topography almost exactly. High surface roughness results in a texturing effect being replicated onto the components. Further investigation is required to improve the surface finish produced by the laser milling process.

The aspect ratio that can be reproduced by hot embossing or microinjection moulding is much higher than laser ablation can produce. Aspect ratios of 2.25 for gaps and 3 for walls are rather low. Nevertheless, the achieved result is still impressive given the

tooling material used, and the fact that the only competition comes from silicon-based manufacturing processes, such as lithography.

The laser milling accuracy is shown to be highly dependent on the laser machining parameters and more importantly on the target material used. Still, the machined features were all within the expected tolerance of 50 μm, and copper proved to be a considerable improvement achieving almost half the expected tolerance – on average 25 μm.

The minimum feature size obtained from laser machining on the specially designed test structures made it obvious that the thermal nature of the laser milling process is the only obstacle to machining micro grooves and walls. However, the process was capable of machining vertical walls of 40 μm thickness with an aspect ratio of 3. The micro grooves proved to be more difficult, and the smallest width achieved fully was 80 μm.

After the process characterisation is complete, it is evident that although laser milling is capable of producing a wide variety of moulding tools for the micro-replication processes, the process is still greatly handicapped by the high surface finish that it can achieve.

Chapter 4 Laser material interaction

Chapter 2 introduced the basic physical phenomenon behind the laser material interaction. In this chapter, a more detailed view of the physical processes and the governing parameters will be presented. A discussion of the available theoretical models and their characteristics is carried out. Later in the chapter, a theoretical model of material heating induced from an incident microsecond laser pulse is developed. Experimental confirmation of the model is also included with two different materials as test targets.

4.1 Existing models of laser material interaction

In a pulsed laser material removal system, it is of crucial importance to develop an understanding of the physical phenomena that take place during the machining process. The short pulse duration and the micro size make a direct experimental investigation difficult to carry out. Consequently, developing a numerical simulation instead of experimentation is a vital opportunity for better understanding and optimisation of the parameters of material removal process through the use of a laser.

Considerable theoretical as well as experimental studies have been carried out on laser material heating and processing. Most mathematical models of the heat flow phenomena in laser material processing were based on the application of the classical heat conduction equation for stationary solid, using the concept of an instantaneous

heat source for an infinite volume. Cases with and without phase change and a variety of radiation or source conditions have been studied.

The simplest case without a phase change arises when a semi-infinite half-space is heated uniformly over its entire boundary surface. Carslaw and Jaeger (1959) initially investigated this type of problem. The next step was applying a pulsed source, and this problem was addressed by Carslaw and Jaeger (1959), White (1963) and Rykalin et al (1967).

Further improvement on the theoretical models was attained by assuming the laser beam to have a Gaussian temporal and spatial distribution, i.e., the laser intensity decreases exponentially from the centre of the beam with the square of the radial distance (Ready, 1971; Cline and Anthony, 1977). An analytical solution to the three-dimensional quasi-stationary heating in a finite depth and width solid with a circular Gaussian moving heat source was developed by Manca et al (1995).

The problem is considerably more complicated when the material goes through a phase change. In the case of rapid material removal by melting and/or evaporating, most of the laser energy is utilised in the phase transitions (melt and evaporate) of the solid, while only a small portion is lost to heat conduction into the bulk of the material. Cline and Anthony (1977) derived a model for laser heating and melting of material for Gaussian source moving at a constant velocity. The derived conduction model was for continuous wave (CW) high power laser, scanning the top surface of semi-infinite geometry. They calculated the temperature distribution and depth of the melting zone as a function of laser beam diameter, velocity and power. A three-

dimensional heat transfer model was developed by Mazumder and Steen (1980) for a laser beam striking the surface moving with uniform velocity. The model was solved by a finite difference method and the results were presented for temperature distribution and melt depth. The model also allowed for the formation of the groove by considering the grid points within the groove as part of the conducting network but operating at high temperature after vaporization. The model is capable of forecasting the temperature profile, the maximum processing speed and the heat affected zone.

Lately, an investigation into short and ultrashort pulse laser machining is attracting more attention (Lunney and Jordan, 1998). Modest (1996) developed a three-dimensional, transient model of laser machining through ablation/ decomposition of materials. The produced model could predict the shape of the resulting hole/groove that is formed by ablation of material, caused by a stationary or moving laser. The model was used to carry out calculations to study the qualitative differences in material removal starting from CW and down to 100 ns pulse length. Fähler and Krebs (1996) formulate a model of heating of a pure metal target (i.e. Fe) including material removal resulting from 30 ns laser pulses. Their model takes into account the absorption of the incident laser radiation by the ablated material and the heat conduction within the target, evaporation and the cooling effect on the target surface by the heat of evaporation and the partial absorption of the incident laser beam in the evaporated material.

A thorough examination of the physics of ultra-short pulse laser/matter interaction that leads to material breakdown and ablation was presented by Liu et al. (1997). The authors discuss the differences in ablation mechanisms between ultrashort and long

pulses and they conclude that for ultrashort laser pulses the ablation mechanism is mainly direct vaporisation of the target material. The results from a number of micrometer and submicrometer features are also presented, achieved from a micromachining experiments with femtosecond lasers. The presented theoretical model is applied to investigate the evaporation and melt layer thickness for the two pulse regimes.

Yilbas et al. (2000) introduced the electron-kinetic theory approach and solved a three-dimensional model of laser heating. A moving laser source is taken into account provided that the laser scans the material surface at a constant speed. The model computes the thermal stresses induced by the incident laser beam and the thermal expansion along the laser axis is predicted.

4.2 Modelling of a single crater

A theoretical model has been developed to investigate the influence of a number of laser parameters on the temperature distribution, heat flow, material removal (e.g. crater) and general laser/material interaction during a microsecond laser pulse irradiating a metal target.

The presented model accounts for:

- Target absorption of the incident laser pulse
- Heat diffusion into the bulk material
- Temporal and spatial pulse shape (Gaussian)

- Material phase transition from solid to liquid to gas state

4.2.1 Theoretical model

When an optical high-energy beam strikes a material surface, a large fraction of the energy contained in the beam will be absorbed into the material. The rest of the energy will be either reflected from the surface of the target or transmitted. This energy will be therefore lost to the environment and will reduce the efficiency of the absorption process. Higher absorption of the material means a higher absorption coefficient for that material for the laser wavelength; therefore more energy will enter the substance and will be transformed into heating. Depending on the magnitude of the material heating, there will be a phase change in the material, usually from solid to melt to vapour.

In laser processing of metals, the fraction of energy that is absorbed in the material is readily transformed into heat. The extent of heating is dependent on three major components and their properties: laser beam, target material and their interaction. The laser beam is characterised by its wavelength, laser power level, spatial and temporal power distribution and the beam spot size. The physical (i.e. density) and thermal (i.e. thermal conductivity) properties are generally used to describe the target material. The laser/material interaction is governed by the interaction time – pulse duration and the absorption coefficient.

4.2.1.1 Laser beam

In most laser applications it is necessary to focus, modify, or shape the laser beam by using lenses and other optical elements. In general, laser-beam propagation can be approximated by assuming that the laser beam has an ideal Gaussian intensity profile, corresponding to the theoretical TEM_{00} (transversal electromagnetic mode 00) mode. Unfortunately, the output from real-life lasers is not truly Gaussian (Wilson and Hawkes, 1987). In order to adapt to this variance, a quality factor, M^2, has been defined to describe the deviation of the laser beam from a theoretical Gaussian. For a theoretical Gaussian, $M^2 = 1$; for a real laser beam always $M^2 > 1$. In all cases, the M^2 factor, which varies significantly, influences the intensity distribution characteristics of the laser beam (Melles Griot, 2004).

In order to gain an appreciation of the principles and limitations of Gaussian beam optics, it is necessary to understand the nature of the laser output beam. In TEM_{00} mode, the beam emitted from a laser begins as a perfect plane wave with a Gaussian transverse irradiance profile as shown in Figure 4.1. The Gaussian shape is truncated at some diameter $2w_0$ either by the internal dimensions of the laser or by some limiting aperture in the optical train. To specify and discuss the propagation characteristics of a laser beam, one must define the $2w_0$ diameter in some way. The commonly adopted definition is the diameter at which the beam irradiance (intensity) has fallen to $1/e^2$ (13.5%) of its peak, or axial value.

The power $P(r)$ contained within the beam at a radius r is obtained by integrating the intensity distribution from 0 to r to yield (O'Shea, 1985):

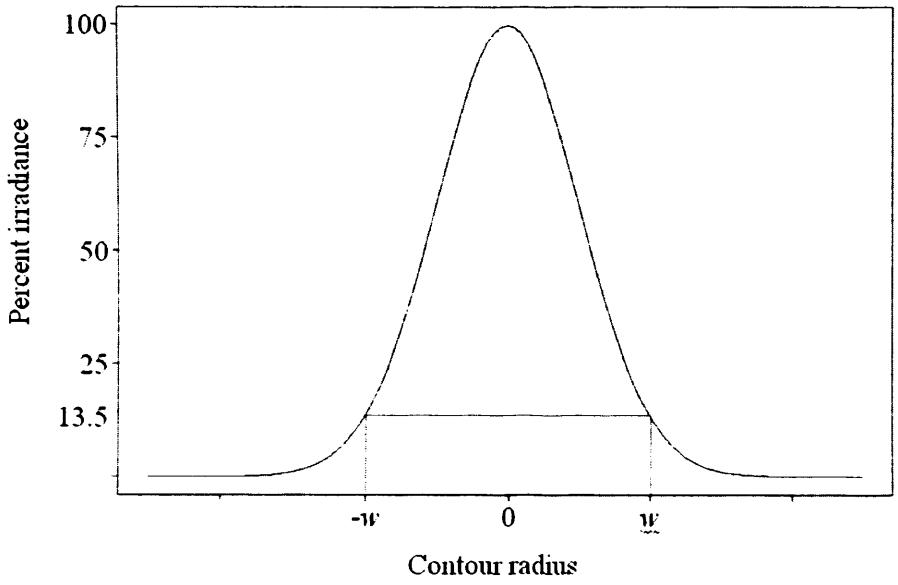

Figure 4.1 Gaussian beam profile – theoretical TEM_{00} mode (adapted from Melles Griot, 2004)

$$P(r) = P(\infty)\left[1 - e^{\frac{2r^2}{w_0^2}}\right] \qquad \text{Eq. 4.1}$$

where $P(\infty)$ [W] is the total power delivered from the laser source, r is the distance from the axis.

For an ideal Gaussian beam, the focal spot diameter $2w_0$ can be calculated in terms of the laser beam parameters from the following equation (O'Shea, 1985):

$$2w_0 = 4\frac{\lambda}{\pi}\frac{s_2}{D} \qquad \text{Eq. 4.2}$$

where s_2 is the focus distance between the lens and the focal spot, D is the diameter of the input beam at the last lens (see Figure 4.2).

However, when a multimode, or distorted Gaussian beam is focused, the equation becomes:

$$2w_0 = 4M^2\frac{\lambda}{\pi}\frac{s_2}{D} \qquad \text{Eq. 4.3}$$

The wavelength of the laser source was discussed earlier in Chapter 2. Now that the laser beam is defined in this way: wavelength, beam spot, power distribution in the spatial and temporal domains, next step is to take a look at the target material.

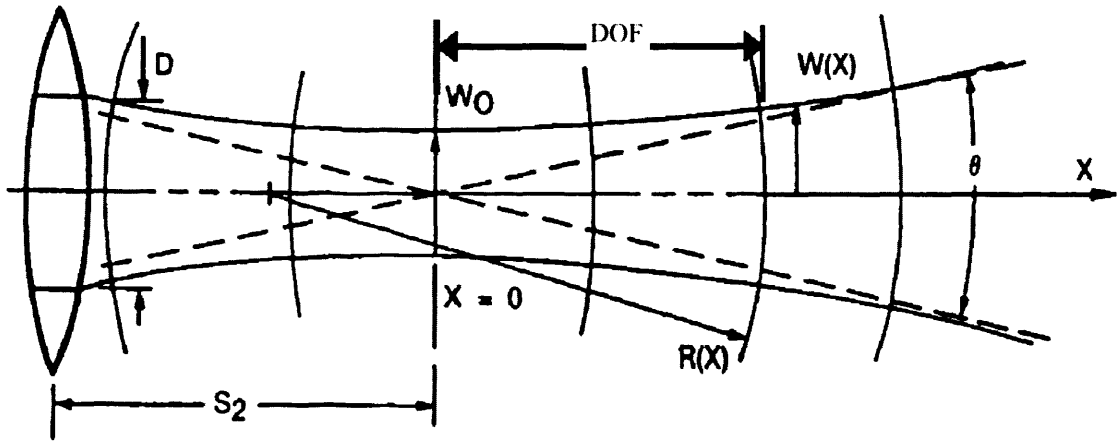

Figure 4.2 Collimated Gaussian beam

4.2.1.2 Material

The material is defined by its properties, namely physical and thermal. The physical property that is required for the description of the target is the material density. The thermal properties are thermal conductivity, specific heat capacity, melting and boiling point, and the latent heat of melting. Usually all this data is available for a wide range of pure materials from reference books, but the composite materials used for this model proved rather difficult to identify especially the boiling point and latent heat of melting.

The developed model is based on conventional heat diffusion equation with a heat source, including the Gaussian temporal and spatial profiles of the laser pulse, the relation between temperature and energy density, and the material change of state. The model does not take into account the heat diffusion in the gas phase of the material, because it is assumed the liquid-to-gas transition as removal of the material.

The general 2D Heat Conduction Equation is the basis of the present simulation (Incropera, 2002):

$$\rho C_P \frac{\partial T(x,z,t)}{\partial t} = k\left(\frac{\partial^2 T}{\partial x^2} + \frac{\partial^2 T}{\partial z^2}\right) + A(x,z,t) \qquad \text{Eq. 4.4}$$

where ρ is the density of the material [kg/m^3]; C_p – specific heat capacity [J/kg.K]; k – thermal conductivity [W/mK]; x, z – space domain dimensions [m] (see Figure 4.3); T – temperature [K]; t – time variable [s].

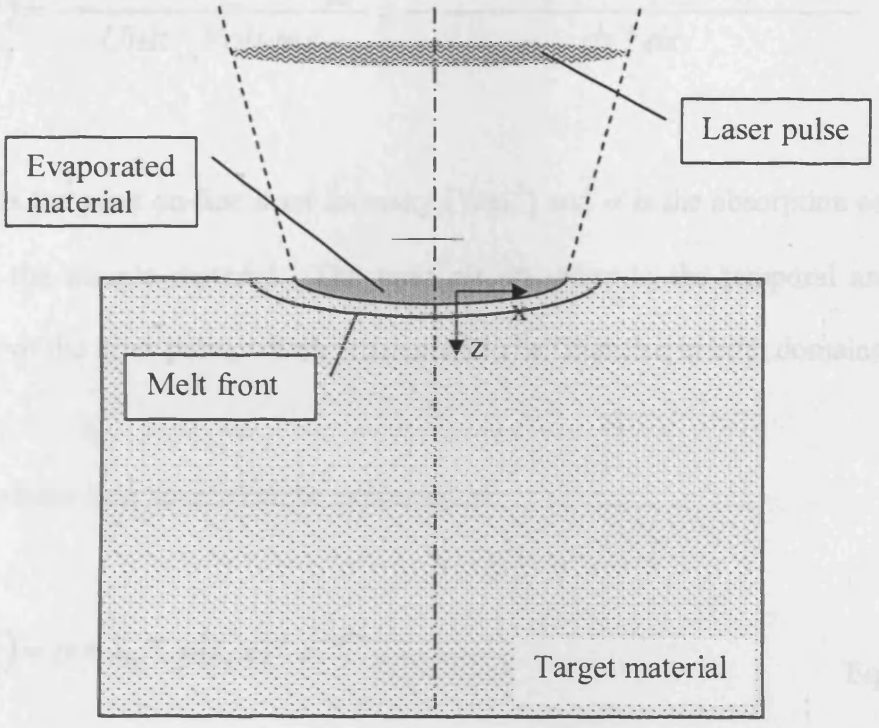

Figure 4.3 Assumptions for the simulation spatial domain

The term A(x, z, t) is the volume heat source (the absorbed laser energy in a given unit of material volume):

$$A(x,z,t)=\frac{Absorbed\_Energy}{Unit\_Volume}=\frac{\alpha * dz * I_0 * ds * p(t,x,)* e^{-\alpha * z}}{dz * ds} \quad \text{Eq. 4.5}$$

where I_0 is the peak on-line laser intensity [Wm^{-2}] and α is the absorption coefficient [m^{-1}] for the sample material. The term p(t, x) refers to the temporal and spatial geometry of the laser pulse, which is assumed to be Gaussian in both domains.

So, the volume heat source can be expressed as:

$$A(x,z,t)=\alpha * I_0 * p(t,x)* e^{-\alpha * z} \quad \text{Eq. 4.6}$$

where the peak laser intensity I_0 is:

$$I_o=\frac{Peak\_Power}{Area}=\frac{P_{peak}}{\pi w_0^2}=\frac{E_p}{\tau\pi w_0^2}=\frac{P_{av}}{f\tau\pi w_0^2}=\frac{P_{av}T_f}{\tau\pi w_0^2} \quad \text{Eq. 4.7}$$

where f is the laser pulse frequency (repetition rate), T_f is the pulsing period.

4.2.1.3 Laser/material interaction

The basic parameters from the laser/material interaction are expressed in Eq. 4.6. The physical phenomena involved in the absorption of the incident laser light by the medium are given by the exponential absorption law:

$$I(x) = I_0 e^{-\alpha z} \qquad \text{Eq. 4.8}$$

where *I(x)* is the light intensity penetrating to depth *z*. The incident laser intensity is I_0; and for the purposes of this model, we neglect the fraction of light that is reflected. The absorption coefficient is available readily for pure chemical materials from optical properties reference books (Billings, 1972; Palik, 1985). The data for composite materials is difficult to attain, and is generally obtained from personal experimentation.

Table 4.1 summarises the physical, optical and thermal properties for the two tooling materials selected for the experimental validation of the theoretical model, namely stainless steel Grade 316 and aluminium 6082, which are used in the simulation calculations.

4.2.2 Numerical solution of the heat equation

Often for problems that require the solution of heat flow or unsaturated water flow, there may be no analytic solutions or neat equations describing the physical process. In such cases a numerical approach is applied to define a solution. One possible approach is the forward finite-difference method (Incropera, 2002).

Properties	Units	Aluminium 6082	Stainless steel Grade 316
Melting point, T_m	K	933	1670
Boiling point, T_v	K	2753	3173
Density, ρ	kg/m^3	2710	8238
Specific heat capacity, C_p	J/kgK	894	468
Thermal conductivity, k	W/mK	154	13.4
Thermal diffusivity, D	m^2/s	6.35×10^{-5}	3.48×10^{-6}
Latent heat of melting, L_m	kJ/kg	400	300
Absorption coefficient @ 1064 nm	m^{-1}	123×10^6	5.45×10^7

Table 4.1 Physical and thermal properties of the experiment materials (Sources: Incropera, 2002; Nath et al., 2002; Weaver et al., 1981; Billings, 1972)

In contrast to an analytical solution, which allows for temperature determination at any point of interest in a medium, a numerical solution enables determination of the temperature at only discrete points.

From the general heat equation Eq. 4.4:

$$\frac{\partial T}{\partial t} = D\left(\frac{\partial^2 T}{\partial x^2} + \frac{\partial^2 T}{\partial z^2}\right) + \frac{D}{k} A(x,z,t) \qquad \text{Eq. 4.9}$$

where D is the thermal diffusivity [m^2s^{-1}] for the simulation material and is equal to:

$$D = \frac{k}{\rho * C_p} \qquad \text{Eq. 4.10}$$

Applying the forward finite difference approximations of the derivatives to Eq. 4.9 and considering the assumptions made in Table 4.2:

$$\left(\frac{\partial T}{\partial t}\right)_{i,j,k} = \frac{T_{i+1,j,k} - T_{i,j,k}}{\Delta t} \qquad \text{Eq. 4.11}$$

$$\left(\frac{\partial^2 T}{\partial x^2}\right)_{i,j,k} = \frac{T_{i,j+1,k} - 2T_{i,j,k} + T_{i,j-1,k}}{(\Delta x)^2} \qquad \text{Eq. 4.12}$$

$$\left(\frac{\partial^2 T}{\partial z^2}\right)_{i,j,k} = \frac{T_{i,j,k+1} - 2T_{i,j,k} + T_{i,j,k-1}}{(\Delta z)^2} \qquad \text{Eq. 4.13}$$

Substituting in the general heat equation and solving for the temperature $T_{i+1,j,k}$:

Dimension	Index	Step	Number of steps
t	i	Δt	n_t
x	j	Δx	n_x
z	k	Δz	n_z

Table 4.2 Assumptions for the numerical solution

$$T_{i+1,j,k} = T_{i,j,k}\left(1-2\frac{\Delta tD}{\Delta x^2}-2\frac{\Delta tD}{\Delta z^2}\right)+\Delta tD\left[\frac{(\Delta z)^2\left(T_{i,j+1,k}+T_{i,j-1,k}\right)+(\Delta x)^2\left(T_{i,j,k+1}+T_{i,j,k-1}\right)}{\Delta x^2\Delta z^2}\right]+$$
$$+\frac{\Delta tD}{k}A(t,x,z)$$

Eq. 4.14

Eq. 4.14 is *explicit* because unknown temperatures for the new time are determined exclusively by known temperatures at the previous time. In this way, the transient temperature distribution is obtained by marching out in time, using intervals of Δt.

The accuracy of the finite-difference solution may be improved by decreasing the values of the temporal and spatial increments. Of course, the number of interior points that must be considered increases with the decreasing of the spatial increments, and the number of time intervals required to compute the solution to a prescribed final time increases with decreasing Δt. Therefore, the computational time increases. The choice of Δx is typically based on a compromise between accuracy and computational requirements. Once the Δx has been selected, however, the value of Δt may not be chosen independently. It is, instead, determined by stability requirements.

An undesirable characteristic of the explicit solution is that it is not unconditionally stable. In a transient problem, the solution for the nodal temperatures should continuously approach final, steady-state values with the increase of time. However, the iterative nature of the explicit method can numerically induce oscillations, thus causing the solution to deviate from the actual result. In order to prevent this erroneous result, the value chosen for Δt must be below a certain limit, which depends

on Δx and other system parameters. This limit is termed a *stability criterion*, and can be obtained mathematically (Incropera, 2002).

Applying the stability criterion to Eq. 4.14 we get:

$$1-2\frac{\Delta tD}{\Delta x^2}-2\frac{\Delta tD}{\Delta z^2}\geq 0 \qquad \text{Eq. 4.15}$$

therefore, the largest time increment is:

$$\Delta t \leq \frac{1}{2}\frac{\rho C_p \Delta x^2 \Delta z^2}{k\left(\Delta x^2+\Delta z^2\right)} \qquad \text{Eq. 4.16}$$

This provides a relationship between the spatial increments Δx and Δz and the largest value of the time increment.

Substituting the heat source in Eq. 4.14 and applying the same principles of finite-difference, we get:

$$T_{i+1,j,k}=T_{i,j,k}\left(1-2\frac{\Delta tD}{\Delta x^2}-2\frac{\Delta tD}{\Delta z^2}\right)+\Delta tD\left[\frac{(\Delta z)^2\left(T_{i,j+1,k}+T_{i,j-1,k}\right)+(\Delta x)^2\left(T_{i,j,k+1}+T_{i,j,k-1}\right)}{\Delta x^2\Delta z^2}\right]+$$
$$+\frac{\Delta tD}{k}\alpha * I_0 * p(t,x) * e^{-\alpha(z_k-h_j)} \qquad \text{Eq. 4.17}$$

The distribution of the laser power in space x and time t is assumed to be Gaussian and is given by:

$$p(t,x)=\int_{-\infty}^{\infty} e^{-\left(\frac{x}{R_0}\right)^2} dx \int_{0}^{\infty} e^{-\left(\frac{t}{\tau}\right)^2} dt \qquad \text{Eq. 4.18}$$

After applying the numerical scheme, we get:

$$p(t_i,x_j)=e^{-\left(\frac{\Delta x\left(j-\frac{n_x}{2}\right)}{R_0}\right)^2} e^{-\left(\frac{i\Delta t-2\tau}{\tau}\right)^2} \qquad \text{Eq. 4.19}$$

Substituting again in Eq. 4.17:

$$T_{i+1,j,k}=T_{i,j,k}\left(1-2\frac{\Delta tD}{\Delta x^2}-2\frac{\Delta tD}{\Delta z^2}\right)+\Delta tD\left[\frac{(\Delta z)^2\left(T_{i,j+1,k}+T_{i,j-1,k}\right)+(\Delta x)^2\left(T_{i,j,k+1}+T_{i,j,k-1}\right)}{\Delta x^2\Delta z^2}\right]+$$
$$+\frac{\Delta tD}{k}\alpha I_0 * e^{-\left(\frac{\Delta x\left(j-\frac{n_x}{2}\right)}{R_0}\right)^2} * e^{-\left(\frac{i\Delta t-2\tau}{\tau}\right)^2} * e^{-\alpha(z_k-h_j)} \qquad \text{Eq. 4.20}$$

4.2.2.1 Initial and boundary conditions:

In order to solve this parabolic equation, an initial condition and three boundary conditions are required.

The initial condition is providing the temperature of the material just before the start of the pulse:

$$T(0,x,z)=293K$$

The three boundary conditions apply constraints to the temperature with respect to the space domain:

$$T(t, x \to -\infty, z) = 293K$$
$$T(t, x \to +\infty, z) = 293K$$
$$T(t, x, z \to -\infty) = 293K$$

Transitions between solid, liquid, and gaseous phases typically involve large amounts of energy compared to the specific heat (Smurov et al, 1991). If heat were added at a constant rate to a mass of material to take it through its phase changes from condensed to liquid and then to gas, the energies required to accomplish the phase changes (called the latent heat of melting L_m and latent heat of vaporization L_v) would lead to plateaus in the temperature *T[℃]* vs time *t[s]* graph (see Figure 4.4).

Thus, in the simulation when a cell reaches the melting point of the simulation material, the following temperature adjustment is added:

$$T_{new} = T_{old} - \frac{L_m}{C_p} \qquad \text{Eq. 4.21}$$

In the model are not consider the heat diffusion in the gas phase, because it is assumed that the evaporated material is directly removed from the system. A cell that has reached sufficient energy density to vaporise is set to melting temperature for the given material (Nantel et al, 2001). In subsequent calculations, adjacent cells will recognise that temperature and ignore those cells as possible heat sources/sinks. The

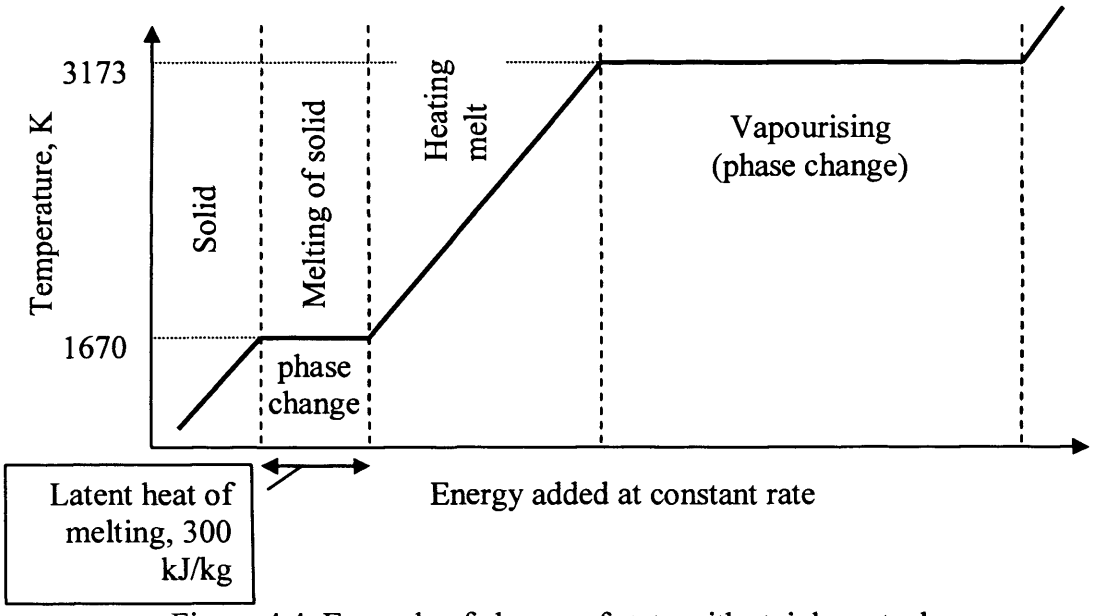

Figure 4.4 Example of change of state with stainless steel

model will also disregard them as an absorption material, and still deliver the correct amount of energy to the now "top-surface" cells.

An experimental confirmation of the proposed theoretical model was carried out. A description of the experiment procedures and results is provided hereafter.

4.3 Experimental procedures

The goal of the experiment was to obtain the profiles and depth of the craters created from laser ablation in two target materials, i.e. stainless steel grade 316 and aluminium 6082. The experiment was created to correspond as closely as possible to the conditions in the theoretical model.

4.3.1 Apparatus

All experiments were performed on an Nd:YAG (FOBA Laser F 94S) laser ablation system with 1064 nm wavelength and the Q-Switch pulse duration was set to 10 μs. The average power delivered from the laser to the workpiece was measured with laser power meter equipped with high power laser sensor (Coherent, 2004) for different laser flashlamp current levels and varying pulse frequency.

4.3.2 Procedure

The experiments were carried out on two workpieces from stainless steel grade 316 and aluminium 6082. Beforehand the selected surfaces on both sample materials were polished to achieve a very good surface finish, and then in order to decrease the reflection of the laser light from the top surface, it was matted.

Since the normal work settings of the machine could not be used, specific settings were created for achieving single craters. In normal working conditions, the crater centres are displaced 10 μm from each other, which meant that with a diameter of around 50 μm the craters were overlapping on average 80%. For the needs of the experiment, single craters were required, which meant that new operating settings had to be selected. The new settings, provided parallel lines of single crater 125 μm apart, see Figure 4.5.

After completing the experiments, the test pieces are cleaned in an ultrasonic bath, to remove any contamination and debris from the surface. Then a 3D surface profile of any 3 craters from each experiment set is taken with the use of the white light interferometry equipment (MicroXAM, 2003).

4.4 Results and discussion

A study of transient single pulse laser heating in a metal substrate is presented. The infrared laser heating source is representative of pulse from a Nd:YAG laser (λ = 1064 nm) with an intensity that has Gaussian time and space profiles. The e^{-2} pulse

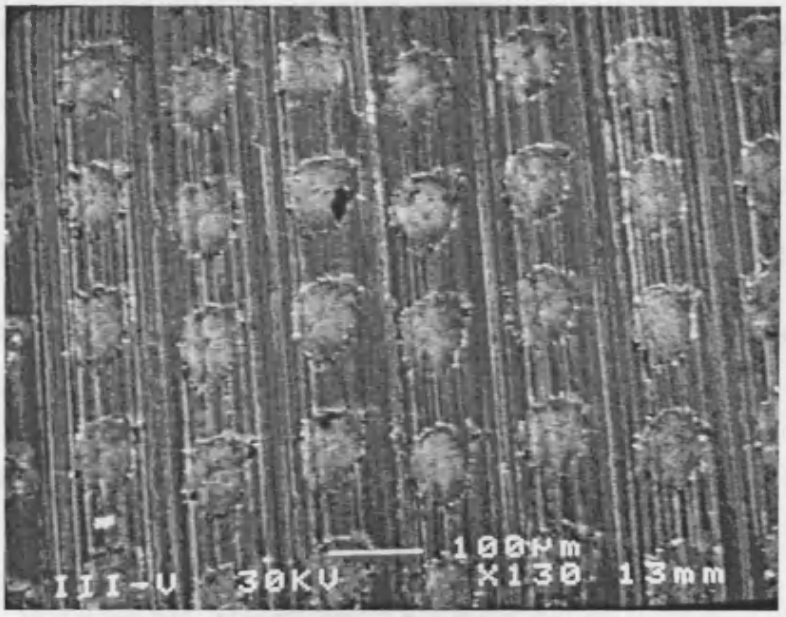

a). Spaced out hatching, (not operational, separate craters clearly visible)

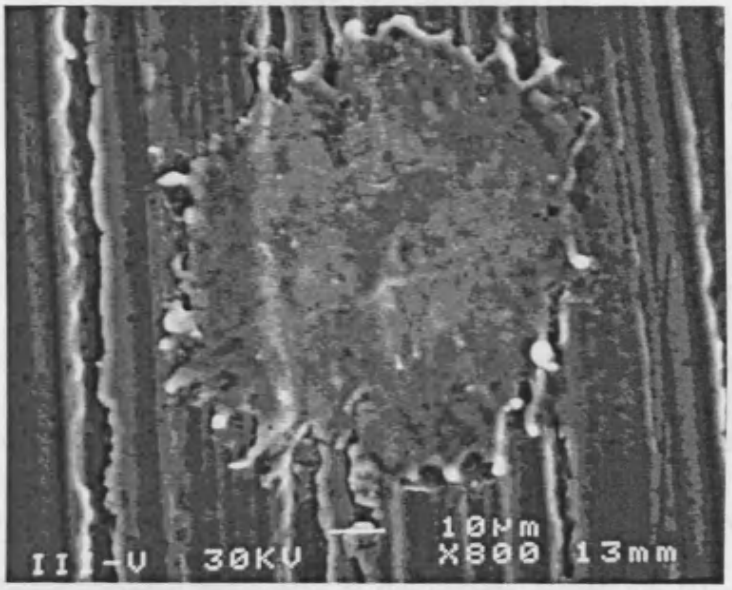

b). close up of a single laser crater

Figure 4.5 SEM pictures of laser craters

duration was assumed to be $\tau = 10$ μs for all experiments. The origin of the time axis ($t = 0$ s) was set so that the maximum laser intensity during the pulse to occur at $t = 0.5\tau$, i.e. the beginning of the pulse and the start of the simulation were coinciding.

The simulation code was written in C++ and was run on standard Windows PC. The calculation times were highly dependent on the parameters of the calculation. Thus, as it was concluded that results with sufficient accuracy and still detailed enough for the scope of the problem can be achieved, the following values were used for all simulation runs (unless otherwise stated):

- Increment in x direction $\Delta x = 2$ μm
- Increment in z direction $\Delta z = 0.4$ μm
- Time step $\Delta t = 1 \times 10^{-8}$ s for stainless steel 316 and $\Delta t = 1 \times 10^{-9}$ s for aluminium 6082;

It is worth noting, the different spatial increments in x and z. This was brought on by the expected results for stainless steel, i.e. the estimated depth (z axis) was expected to be in the range of 2 to 8 μm while the radius of the crater (x axis) was anticipated to be between 40 and 80 μm. The difference in the time steps for the two materials is due to the different material properties of the targets, which are taken into account when calculating the stability criterion for the simulations.

Figure 4.6 illustrates the evolution of the temperature in depth (z axis) and time for both validation materials. It is evident from the figure, that both target materials start melting before $t = 3$ μs. Although both materials have different boiling temperatures

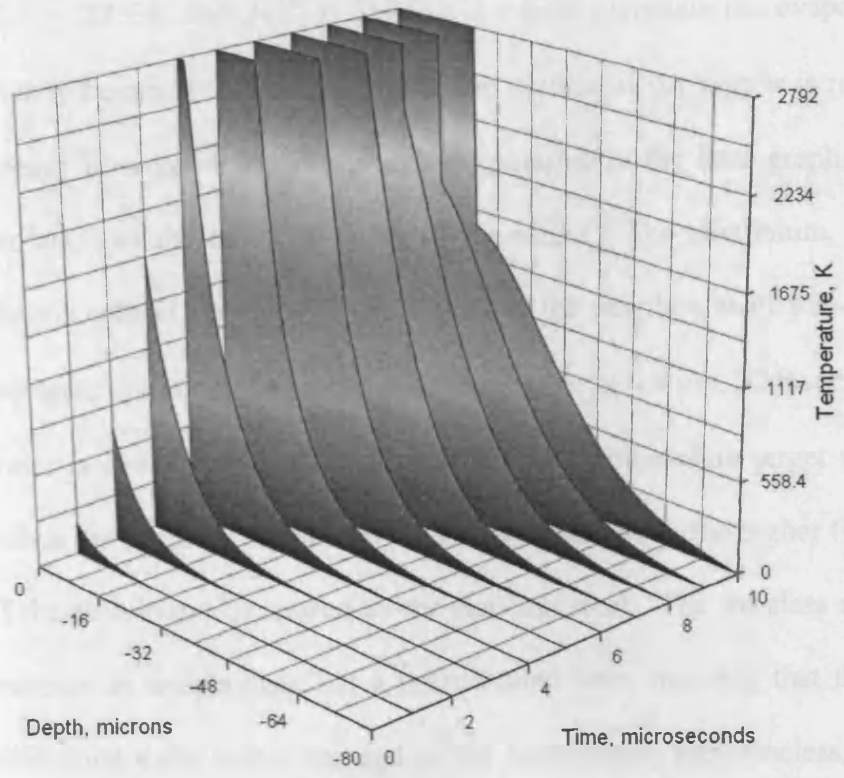

a). Aluminium 6082

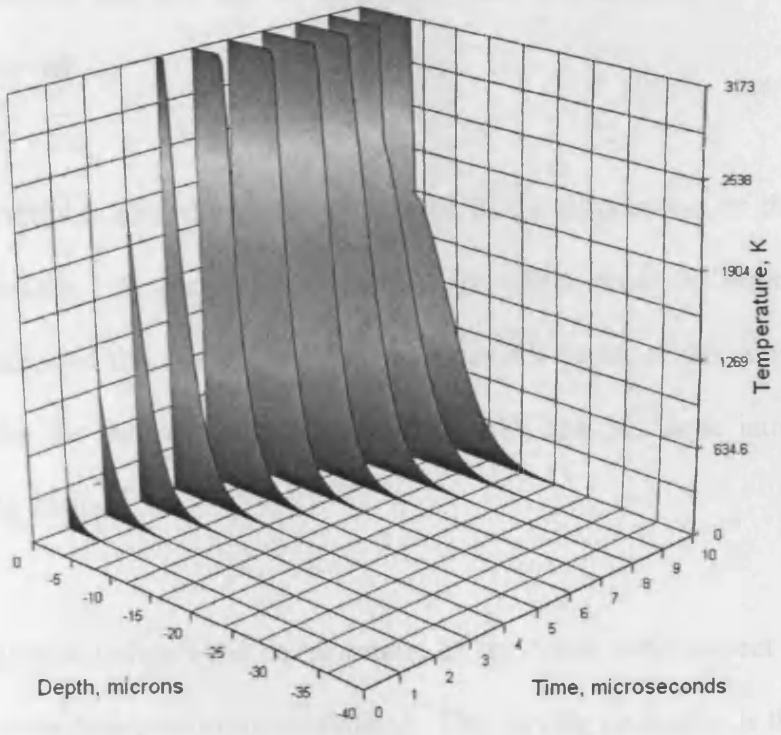

b). Stainless steel 316

Figure 4.6 Temperature distribution along the *z* axis from a laser pulse with fluence

$$F_0 = 2.56 \text{ Jcm}^{-2}$$

(T_v^{Al} = 2753K and T_v^{316} = 3173K), for both materials the evaporation process has already begun at t = 4 μs. The flat top surface of the graphs is representative of the already removed material through evaporation in the later graphs and describes the evolution of the crater in depth of the target. The aluminium, reaches its highest crater depth at time t = 7 μs, while for the stainless steel the depth of the crater increases until t = 8 μs reaching its max value of 6.8 μm. Conversely, the aluminium crater is already at depth 18.8 μm. Also, the aluminium target starts cooling down before the stainless steel at t = 8 μs, and this is due to the higher thermal conductivity of the aluminium compared to the stainless steel. The stainless steel also exhibits a decrease in temperature but a microsecond later, meaning that the target is already solidifying even before the end of the laser pulse. Nevertheless, the crater depth is preserved and can not be decreased once it is assumed that the material has been removed.

Figure 4.6 also shows the difference in the distribution of the temperature in both materials. At the end of the pulse, the effects from the laser induced heating have penetrated the aluminium to almost the full depth of the simulation space (80 μm), while for the complete pulse duration, the heat has gone into the stainless steel for only 25 μm.

Figure 4.7 shows the development of the crater with respect to the increasing laser fluence delivered to the workpiece. The varying parameter is the average laser power, because it is directly measurable with the use of laser power meter. The average power P_{av} = 8.8 W is calculated to produce a laser fluence that is equal to F_0 = 2.8 Jcm^{-2}. The lowest value of the incident laser power included in the simulation

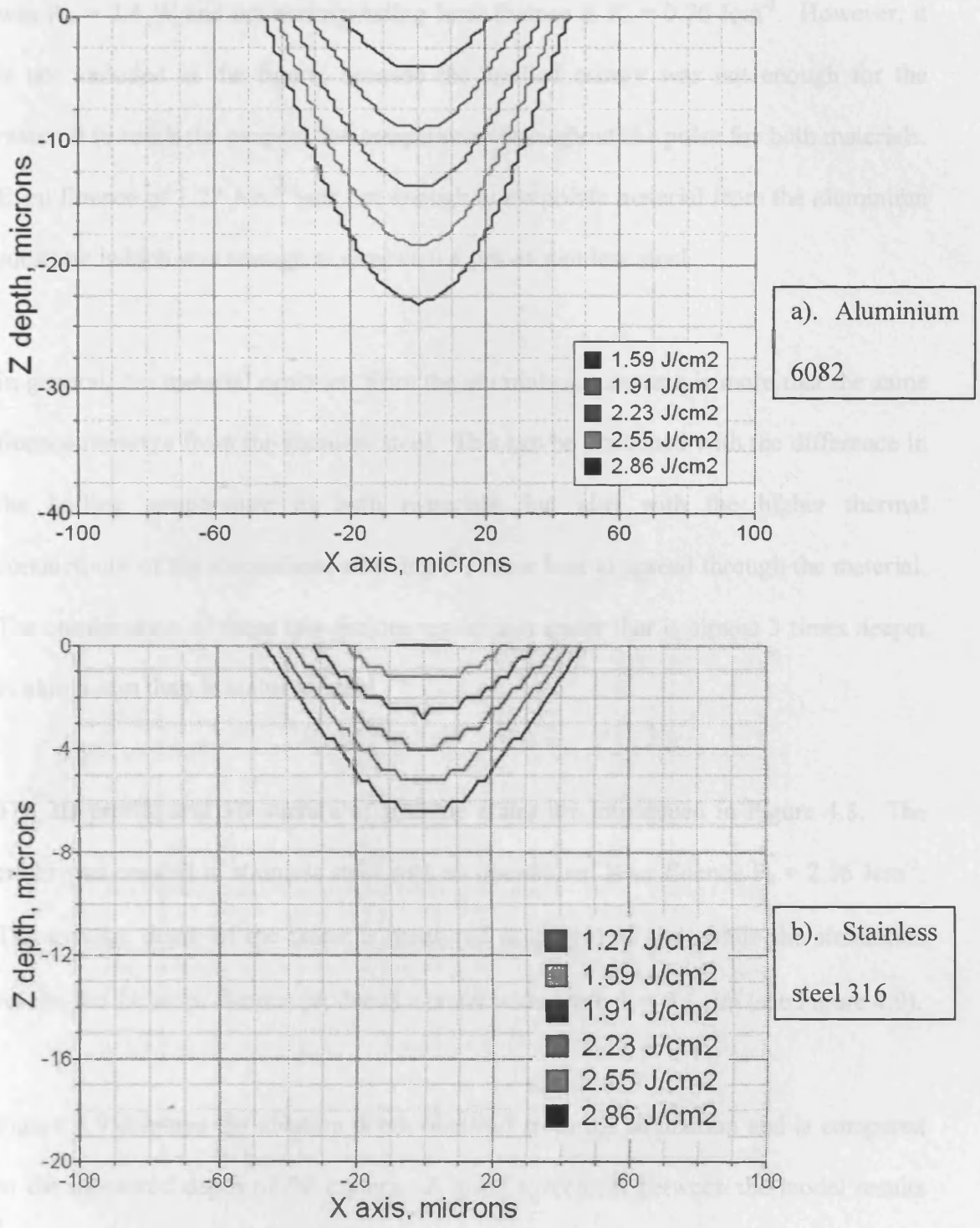

Figure 4.7 Simulation crater depths obtained from varying laser fluence

was P_{av} = 2.4 W and the corresponding laser fluence is F_0 = 0.76 Jcm^{-2}. However, it is not included in the figure, because the applied energy was not enough for the material to reach the evaporation temperature throughout the pulse for both materials. Even fluence of 1.27 Jcm^{-2} was not enough to evaporate material from the aluminium substrate, which was enough to remove 0.4 μm of stainless steel.

In general, the material removed from the aluminium substrate is more that the same fluence removes from the stainless steel. This can be explained with the difference in the boiling temperature of both materials, but also with the higher thermal conductivity of the aluminium, allowing for more heat to spread through the material. The combination of those two factors results in a crater that is almost 3 times deeper in aluminium than in stainless steel.

The 2D profile and 3D surface of a single crater are introduced in Figure 4.8. The crater was created in stainless steel with an operational laser fluence F_0 = 2.56 Jcm^{-2}. The average depth of the crater is measured at d_m = 4.65 μm, while the simulation results for the same fluence produced a crater with depth d_s = 5.1 μm (see Figure 4.9).

Figure 4.9 displays the ablation depth obtained from the simulation and is compared to the measured depth of the craters. A good agreement between the model results and the experiment is achieved on the absolute rate. There is a significant difference in the ablation threshold value, the model predicting the start of the material removal through evaporation at around F_0 = 0.76 Jcm^{-2}, while the experiment was still removing material at F_0 = 0.36 Jcm^{-2}. However, the removed material depth was less than the depth increment (Δz = 0.4 μm) used in the model.

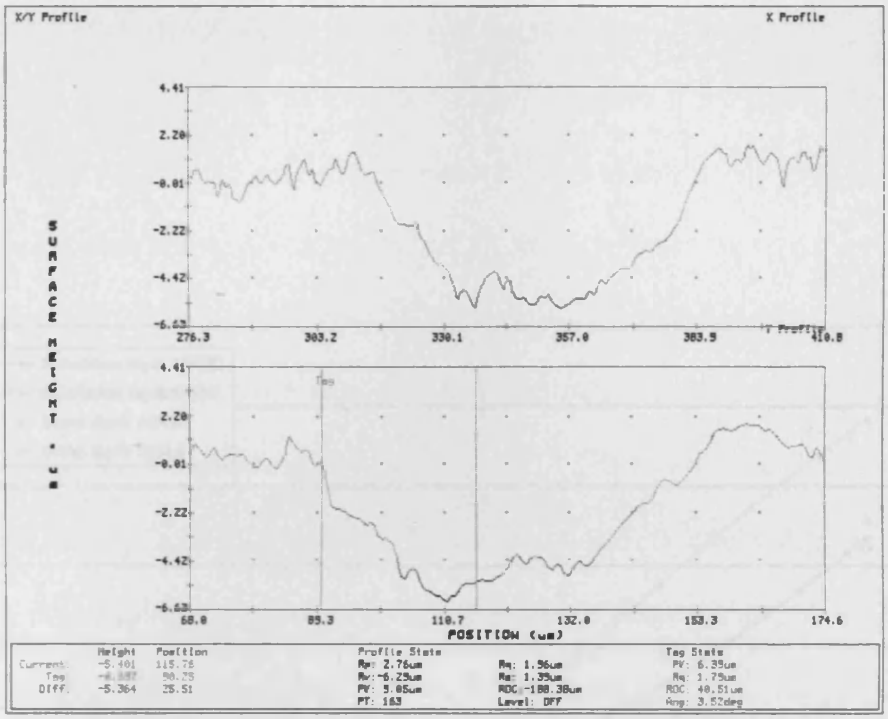

a). 2D profiles in two directions *x* and *y*

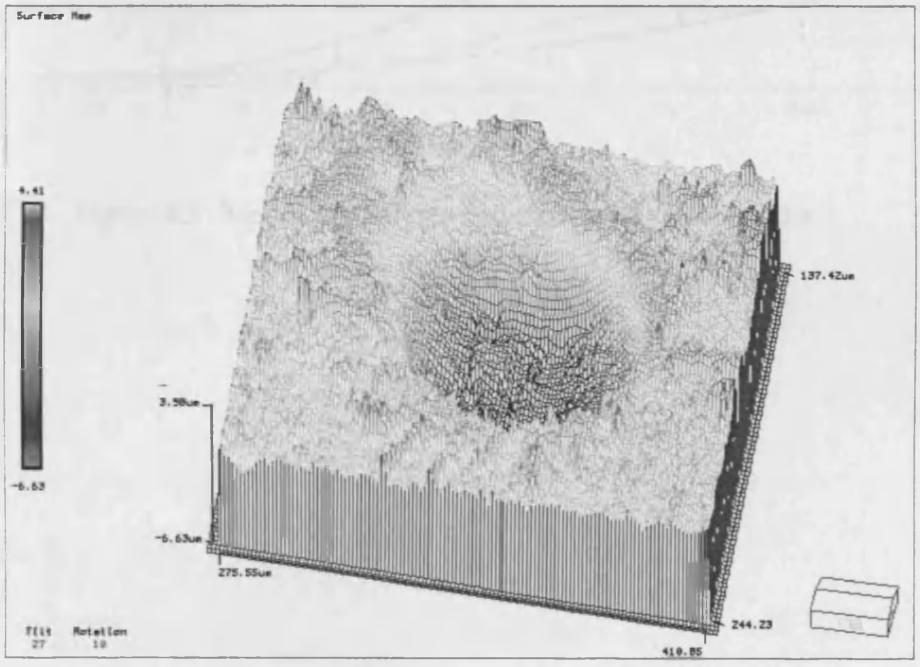

b). 3D representation of a crater from the surface profile measuring equipment

Figure 4.8 Profile of a single crater

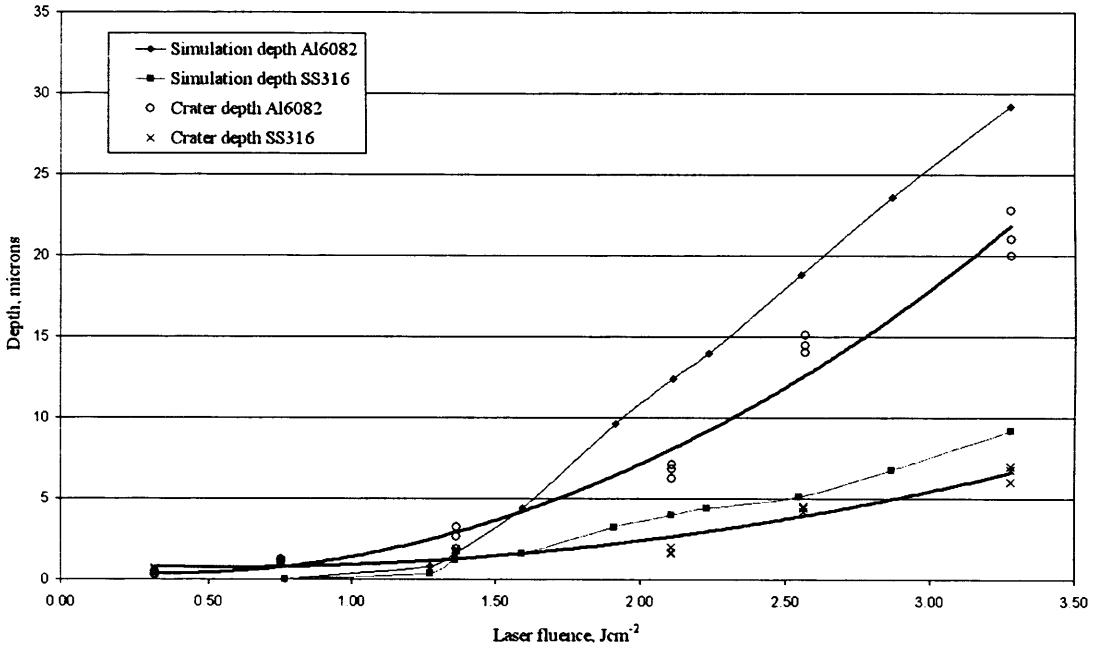

Figure 4.9 Model predictions and measured crater depths

It can be seen in Figure 4.9 that, at high fluence, the model predicts that more material will be evaporated from the target. And at low fluence, the simulation produces lower removal rates. This could be explained by the simplification of the absorption process into the evaporated material. The more material is evaporated, the more energy is absorbed into it, thus letting a smaller amount of energy to reach the target surface.

Figure 4.10 provides a detailed view of the temperature evolution in stainless steel from a laser pulse with fluence F_0 = 2.56 Jcm^{-2}. There are 10 snapshots of the temperature, with a 1 μs step. All graphs have the same arrangement; the *x* axis of the graphs also represents the *x* axis of the models with the origin located in the middle, the graphs' *y* axis is the *z* depth into the material, thus the zero being at the top of the graph. From the temperature's progress into the material, one also can judge the characteristics of the recast layer, i.e. the target material that has been melted and then re-solidified.

The melt front is the temperature gradient at which the target material changes state from solid to liquid (melt). The melt front propagates through the material ahead of the evaporation front, which forms the craters. The location of the melt front at time t = 9 μs, can be observed on Figure 4.11. The line representing the melt front is located at the melting temperature for the stainless steel T_m = 1670 K. The recast layer in that case has a thickness of 5 μm, i.e. this is the distance between the melt front and bottom of the crater.

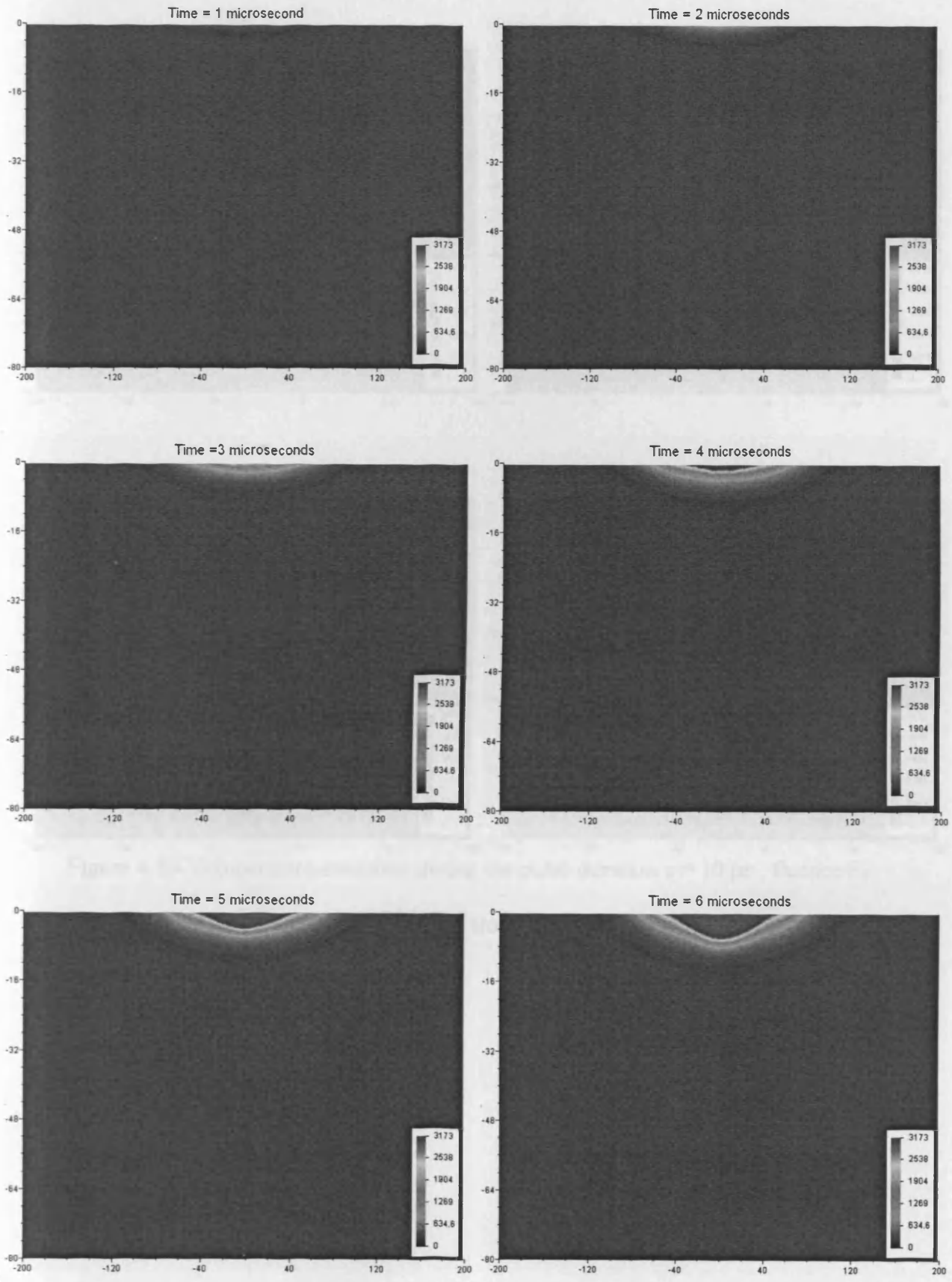

Figure 4.10 Temperature evolution during the pulse duration (cont'd on next page)

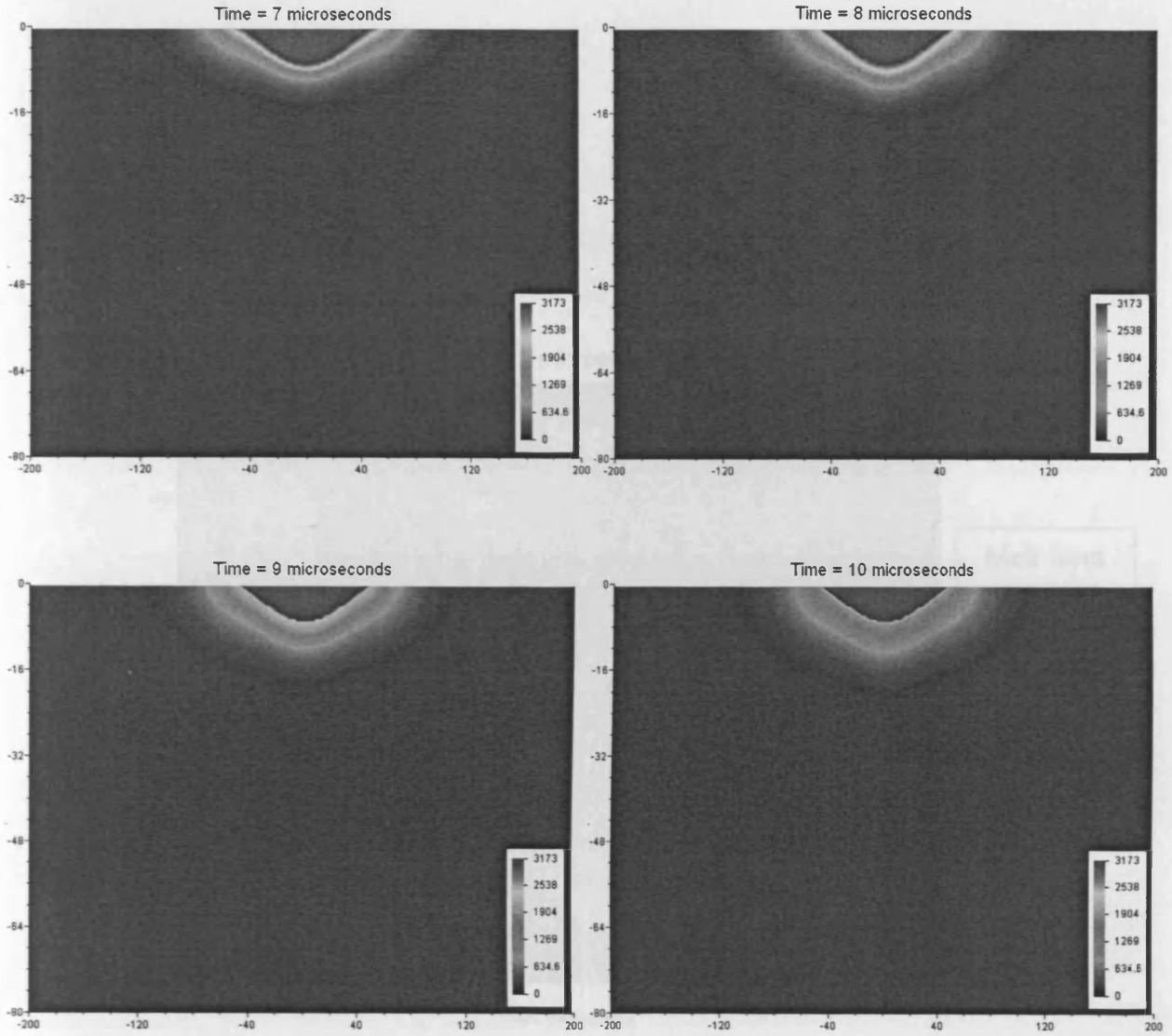

Figure 4.10 Temperature evolution during the pulse duration $\tau = 10\ \mu s$, fluence $F_0 =$ $2.56\ Jcm^{-2}$ (cont'd from previous page)

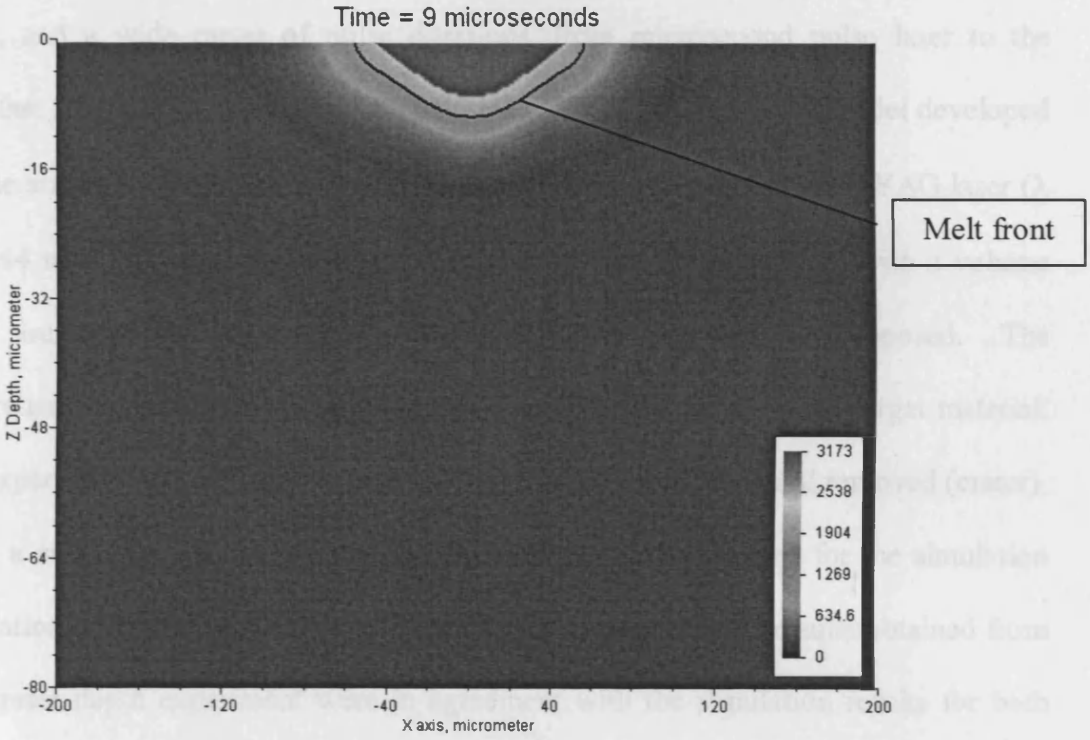

Figure 4.11 Melt front location at t = 9 μs - simulated recast layer thickness

4.5 Summary

This chapter, has presented a comprehensive account of the latest and classical theoretical models of laser ablation. These models cover a wide range of laser ablation processes: continuous wave (CW) and pulsed laser, stationary and moving laser, and a wide range of pulse durations, from microsecond pulse laser to the ultrafast femtosecond. Then a description is given of the theoretical model developed by the author to simulate the material removal from a microsecond Nd:YAG laser (λ = 1064 nm). A numerical solution for the heat conduction equation with a volume heat source resulting from the absorption of the laser light is proposed. The theoretical model also takes into account the change of state for the target material. An experiment was carried out to measure the profile of the material removed (crater) from a single laser pulse. Two different materials were selected for the simulation validation: aluminium 6082 and stainless steel Grade 316. The results obtained from the crater depth experiment were in agreement with the simulation results for both target materials. The simulation results also provide an insight into the effects of laser pulses with different power/energy levels.

Chapter 5 Complex surface formation

In the last chapter, a theoretical model of laser ablation was presented, and the results showed a good conformity with the measurements of the crater from a single laser pulse. This chapter presents models developed for more complex surface topography, to better understand the formation of the surface roughness generated from laser milling. The factors are separated in two groups. The first group is responsible for the formation of the base surface. Such factors are the crater profile and the overlapping of neighbouring craters. The overlapping of the craters is a very important parameter of the laser milling process, because it is directly dependent on the frequency of the laser f [kHz] and the scanning speed V [mm/s]. The second group of factors is generally factors that degrade the surface quality. The occurrence of debris and recast formations are such factors, thus estimation of their effect on the final surface topography is attempted. Another factor is the power distribution of the real laser beam spot, which leads to the real crater shape differing from the ideal model.

5.1 Base surface formation

The formation of the base surface in laser milling is determined from the overlapping of the craters. Figure 2.6 presents the basic 3D geometry and the slicing technology in laser milling and in Figure 2.7 the formation of a single slice is described. For the formation of the base surface, mainly the single slice will be dealt with (see Figure 2.7), and therefore a more in-depth description is provided below.

5.1.1 Single slice formation

A single slice contains two different types of laser beam paths (see Figure 2.7). The first is the border cuts, which follow the outline of the geometry, and constructs the outer walls of the geometry. This type of laser beam path provides the user with the option to apply two or more different laser parameters for machining the geometry walls, thus achieving better wall quality.

The second type of laser beam path is hatching. It is usually responsible for removing the bulk of the material and the formation of the resultant surface topography. The key parameter for both border cuts and hatching is the step-over, which is the distance between two neighbouring laser beam traverses (see Figure 5.1 and Figure 4.5a). For uniform surface quality in both axes, it is usually set to be equal to the distance between two neighbouring laser craters, that is obtained as a result of the combination of the scanning speed and the laser frequency. This distance is also the major parameter, when calculating the overlapping of the neighbouring craters.

5.1.2 Crater overlapping

Assuming that the 2-D projection of the craters created from the laser material removal are ideal circles with a given radius R, the following equation can be derived for the area of the circle-circle intersection (see Figure 5.2):

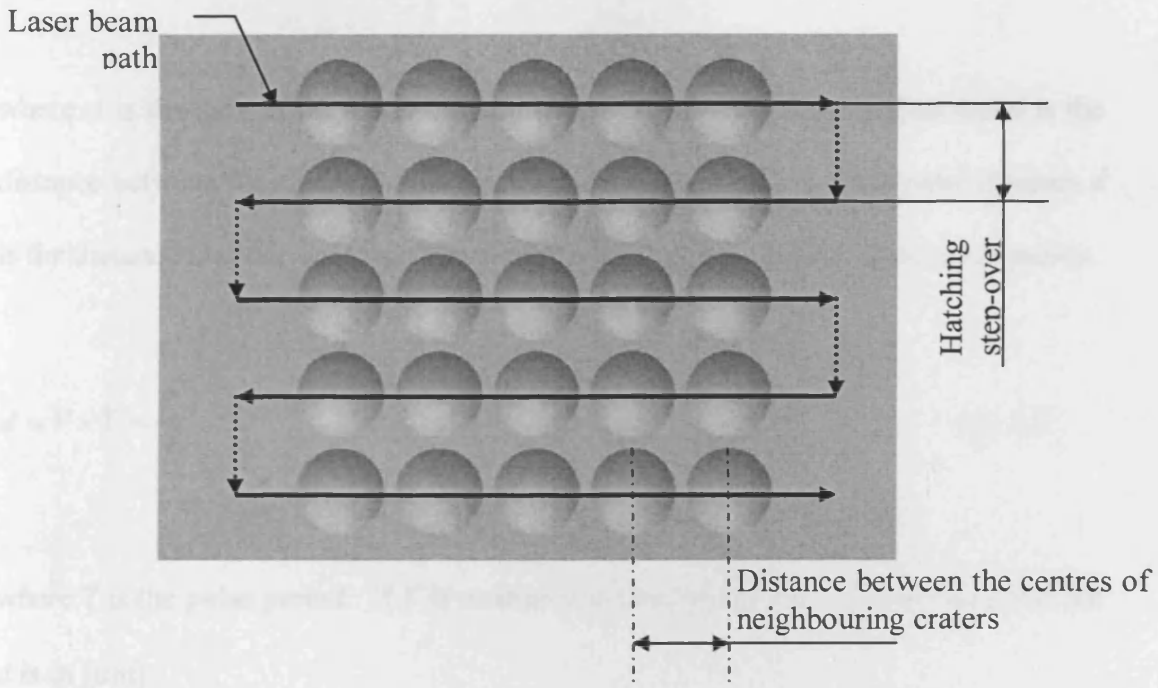

Figure 5.1 Formation of a hatching slice

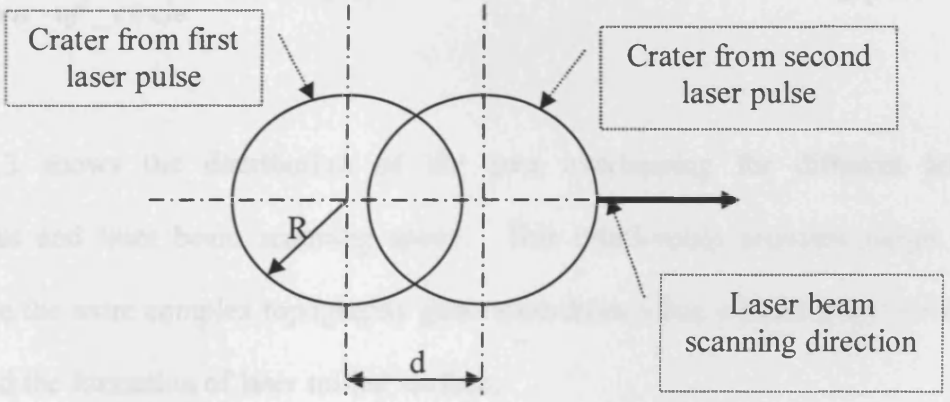

Figure 5.2 Overlapping craters

$$A = 2R^2 \cos^{-1}\left(\frac{d}{2R}\right) - \frac{d}{2}\sqrt{4R^2 - d^2} \qquad \text{Eq. 5.1}$$

where A is the area of the circle-circle intersection, R is the crater radius and d is the distance between the centres of the two circles or pulse distance. The pulse distance d is the distance that the laser beam traverses in the time between to consecutive pulses:

$$d = V \times T = \frac{V}{f} \qquad \text{Eq. 5.2}$$

where T is the pulse period. If V is measured in [mm/s] and f is in [kHz], the result for d is in [μm].

In order to find the percentage of overlapping area, apply the following formula:

$$A_o = \frac{Overlapping\_Area}{Area\_of\_circle} \times 100\%, \text{ [\%]} \qquad \text{Eq. 5.3}$$

Figure 5.3 shows the distribution of the area overlapping for different laser frequencies and laser beam scanning speed. This relationship provides means to investigate the more complex topography generation from a line of craters and further understand the formation of laser milled surface.

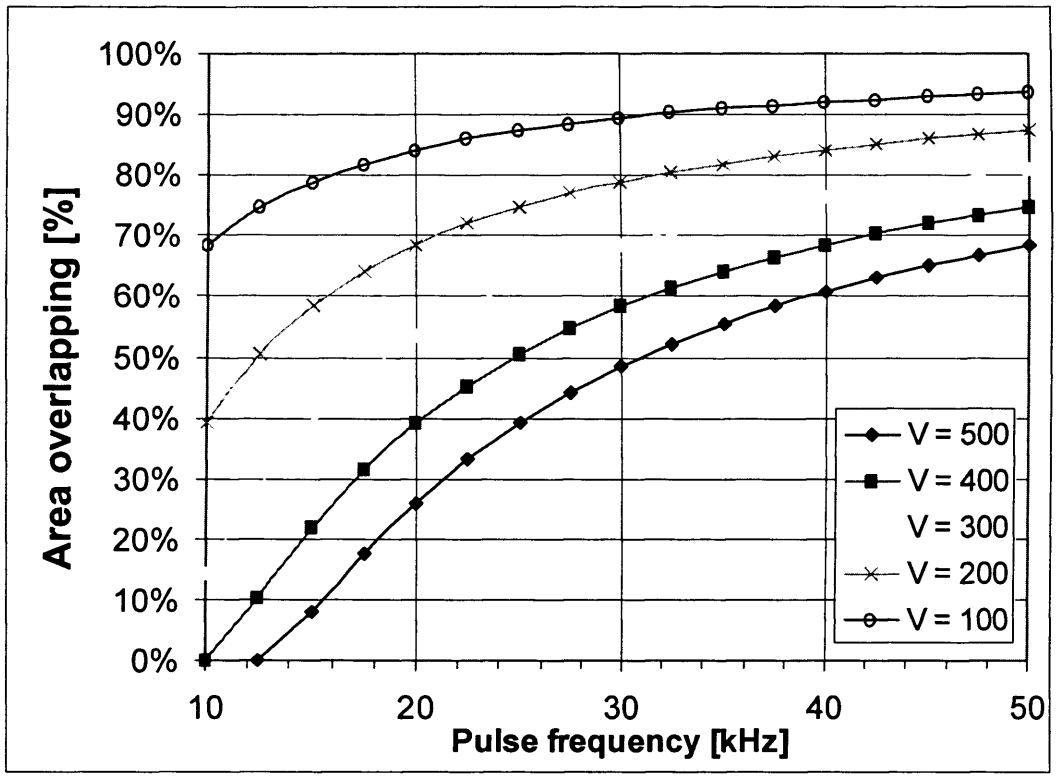

Figure 5.3 Area overlapping of craters, as a function of pulse frequency f and scanning speed V

5.1.3 Surface of 3D craters

In the previous chapter, the profile of a single crater was investigated, and the 2D cross-sections of such craters obtained for different laser beam intensities (see Figure 4.7). With the help of modern CAD packages, the obtained profiles can be used to create a 3D representation of the material removed from a single laser shot. Considering the relationship describing the behaviour of the moving pulsed laser beam together with the slice formation, one can interpolate a representation of the surface topography resulting from machining a single slice with laser milling.

Figure 5.4 presents a simulation of material removal from a block of material, following the described laser milling parameters. The first figure shows a surface created with an equal crater spacing in both axis x and y. The second utilises two different values for the crater spacing in each axis. The difference in the resultant surface is obvious: the even spacing produces a surface that follows an even pattern in each direction, while the varying spacing produces a clear creased topography. Depending on the difference in the spacing, i.e. the area overlapping of the craters due to the laser milling parameters, the surface roughness will be different in each direction.

The more important question is what is the optimal area overlapping in order to achieve the best possible surface roughness. Since the size and geometry of the craters is strongly dependent on the power of the laser beam, therefore one can expect to have different values for the optimal overlapping for different laser power levels.

Figure 5.5 presents the effect of the varying crater depths on the absolute R_y of the resulting surface. The simulation is created with constant hatching distance in both *x-* and *y-directions* and is equal to 10 μm. The varying crater depths represent the different power levels of the laser, thus indirectly the figure shows the effect of the power on the surface roughness.

While Figure 5.5a displays almost linear relationship between the R_y surface parameter and the crater depth for the stainless steel, the relationship for the aluminium shown in Figure 5.5b is completely different. The graph still has a linear section below 12 μm depth. Above that the graph gradually flattens and even there is a slight drop in R_y above 20 μm depth. It is worth mentioning the values for the crater depths in both materials correspond to the same fluence range for the laser.

Therefore, it becomes obvious from Figure 5.5, that the large craters created in the aluminium workpiece, also produce a higher surface roughness. Still, the effect of the deeper craters is limited, and above a certain point, the effect reversed.

The combined effects of the varying hatching distance and crater depth on the R_y surface parameter, is introduced in the next Figure 5.6. The figure shows the predicted effects of varying the distance between the craters, when both directions are equal.

The hatching distance has a definite effect on the R_y of the resulting surface for both considered materials. The relationship for both materials is almost identical, and the

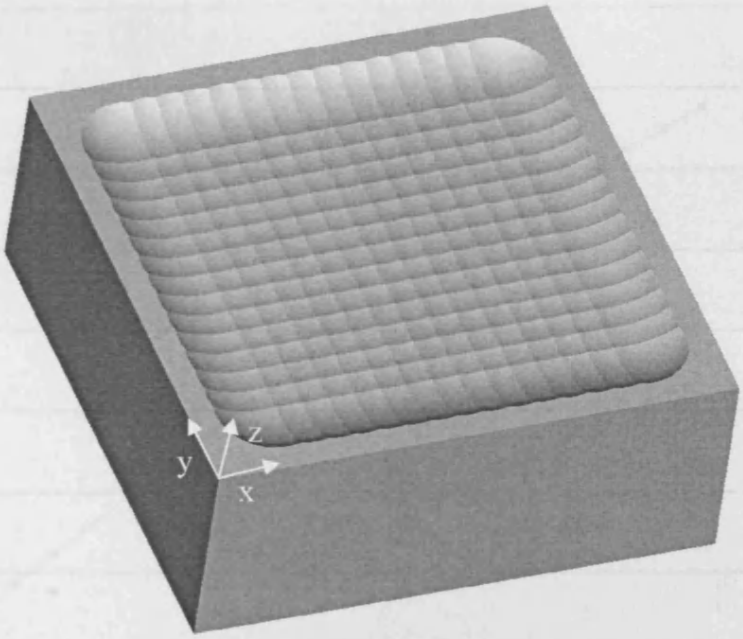

a). equal spacing in both x and y

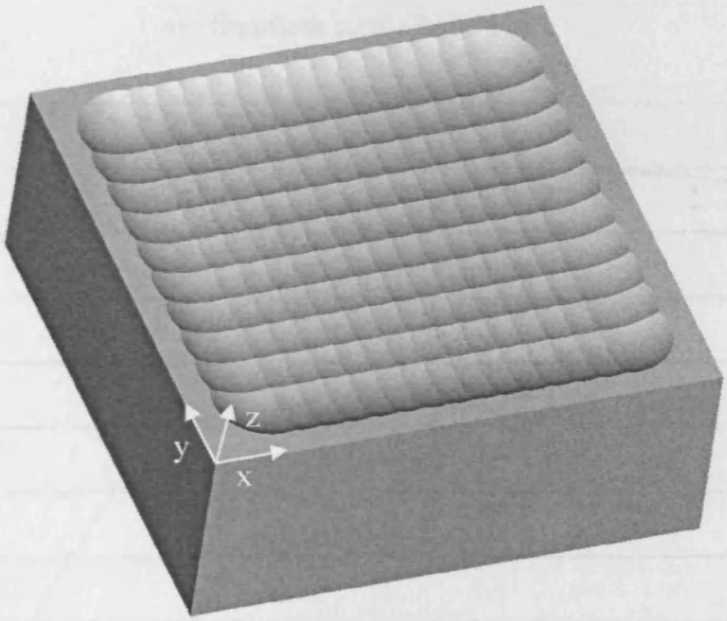

b). different spacing in x and y

Figure 5.4 Formation of the base surface in laser milling

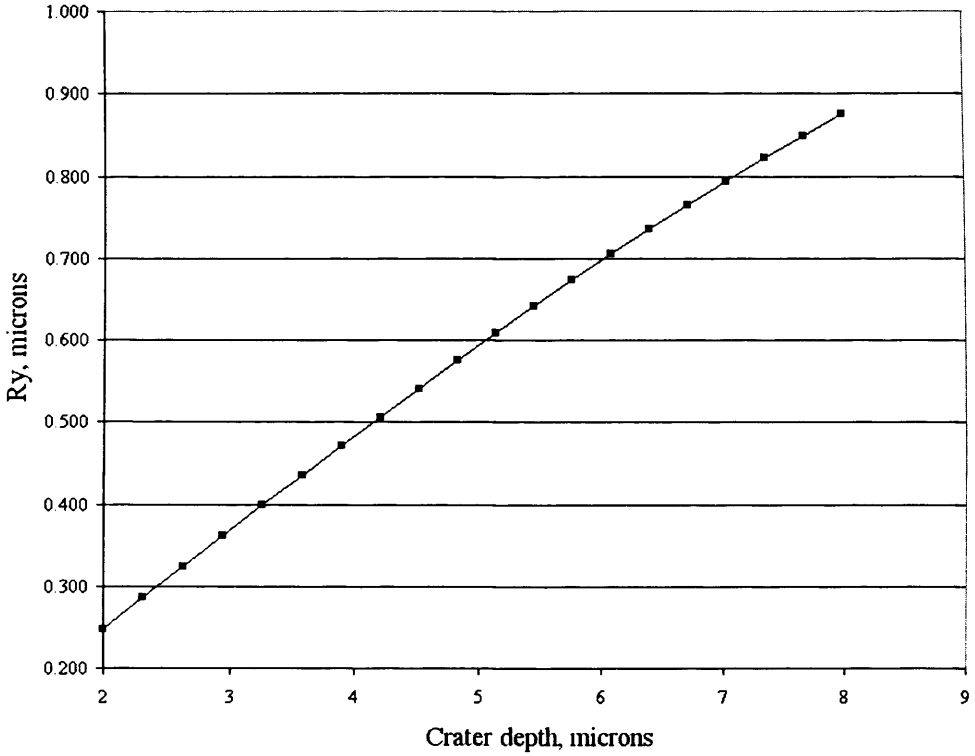

a). Stainless steel Grade 316

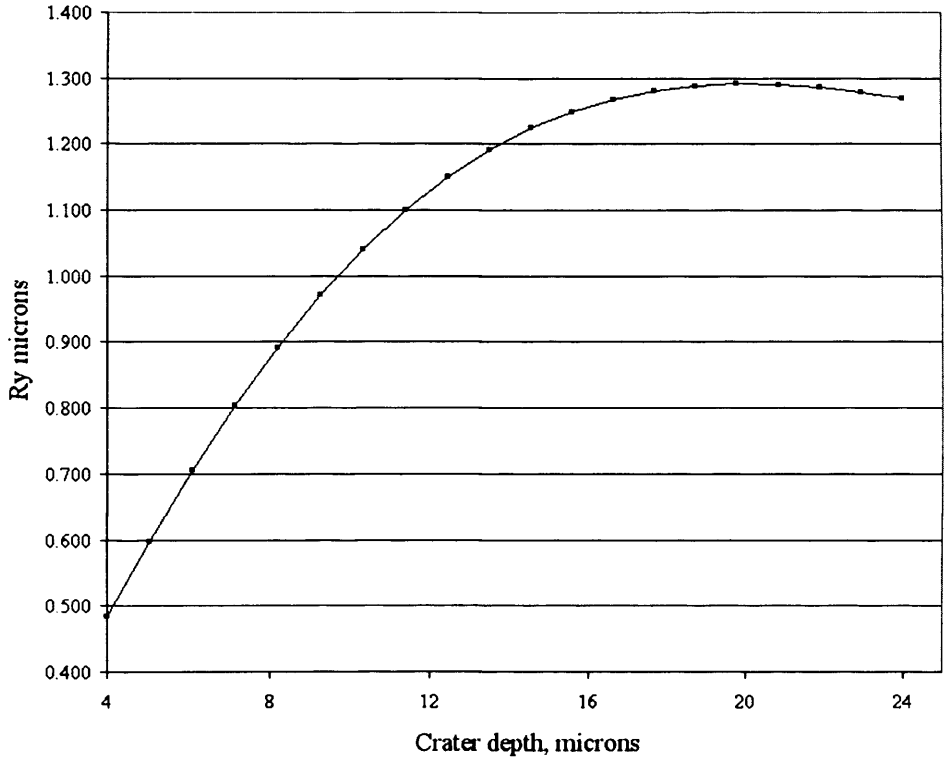

b). Aluminium 6082

Figure 5.5 Graphs of R_y for varying crater depths

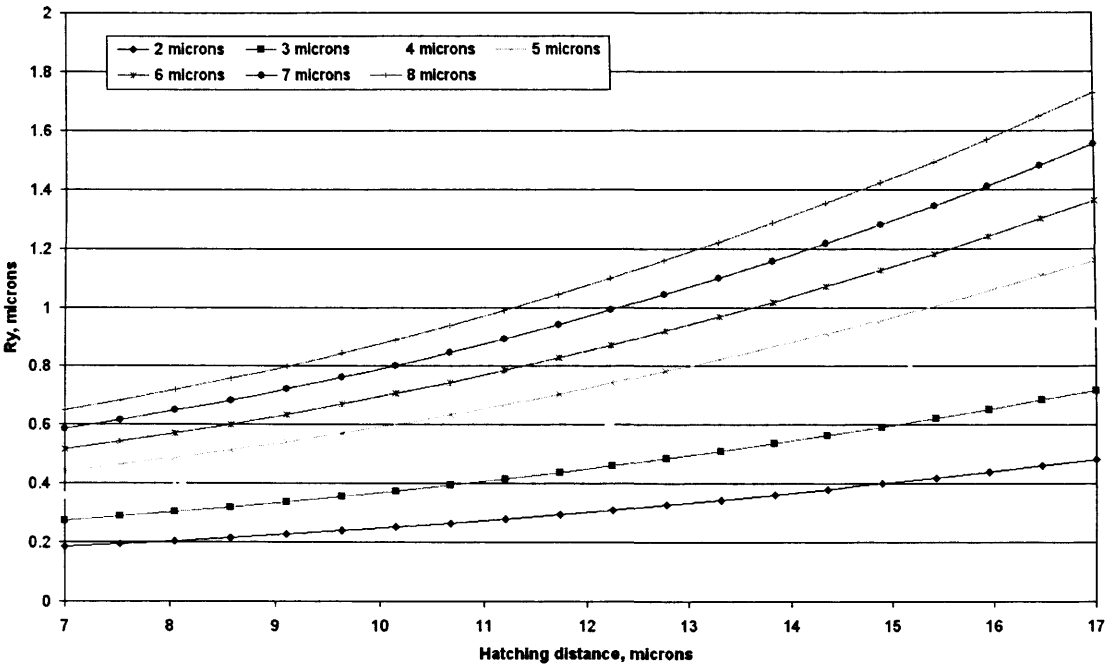

a). Stainless steel Grade 316

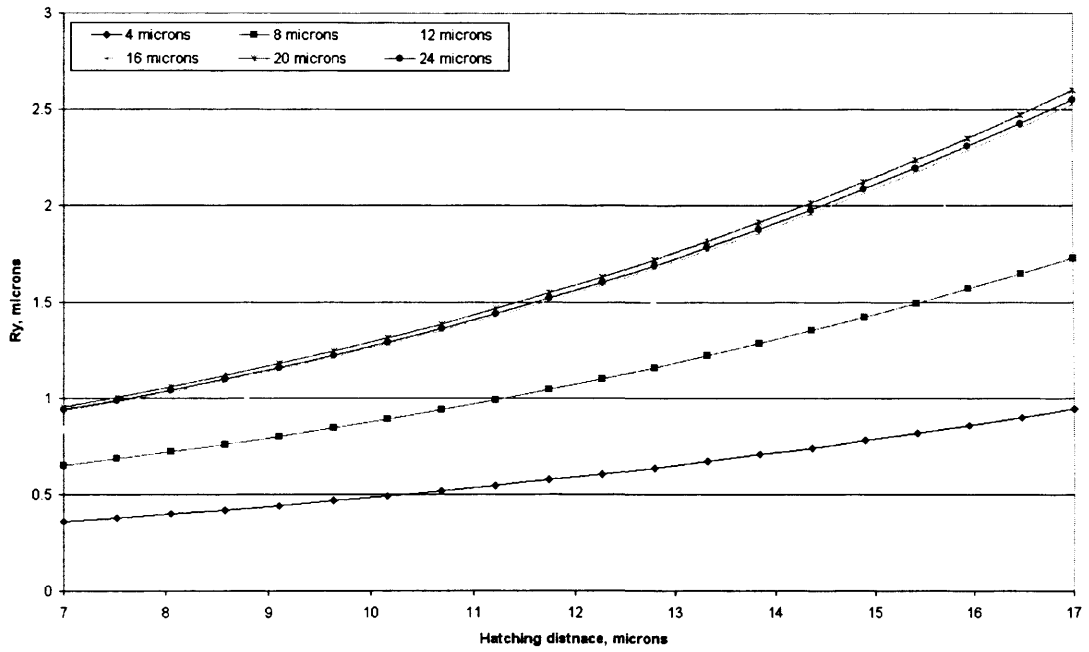

b). Aluminium 6082

Figure 5.6 Graphs of R_y for varying hatching distances and crater depths

overall effect of the different materials is only obvious with the changing crater depths. Nevertheless, the effect of the hatching distance on the R_y parameter is considerably weaker than the laser power. For example in stainless steel, the increase in R_y is 0.3 μm and 1.1 μm for the 2 μm and 8 μm deep craters respectively.

Another very significant factor in forming the surface roughness is the recast debris that falls down on the material surface near or inside the crater itself.

5.2 Secondary surface formation effects

The secondary surface formation effects are basically the negative effects of the real material removal process as opposed to the ideal case scenario, considered in the base surface formation. We will consider the effects on the final surface topography from the debris and recast formations (Zhu, 2000), and crater shape imperfection.

5.2.1 Debris and recast formations

Figure 4.8(b) shows 3D view of the surface profile from a single crater created from laser fluence $F_0 = 2.56 \times 10^{-5}$ Jcm^{-2}. The crater is clearly distinguishable, and the surrounding material surface is covered in molten debris ejected from the crater during the laser pulse and re-solidified. Since the location and the amount of debris are result of random factors, which are impossible to predict in advance, it is reasonable to simplify the task and only investigate the detrimental effect that they have on the surface roughness.

Comparing the surface profiles for single craters created from different laser milling system parameters, can provide a reasonable approximation of the amount of material ejected from the crater and deposited on the surface, very much the same way that it was done for the material removal. Calculating the volume and measuring the average height of the recast debris is possible from the surface profiles of the single craters and will provide a quantitative measure of the detrimental effects on the formation of the final surface topography. Also it is reasonable to assume that the volume of the debris will be in direct relationship to the volume of material removed for the formation of the initial "parent" crater.

5.2.1.1 Volume and height of debris

To calculate the volume of debris, re-solidified on the top surface of the target substrate, it is assumed that initially the top surface is flat. After producing the craters everything above the top surface is debris deposited from the material removal process that formed the crater.

Calculating the volume of material above the top surface of the substrate was based on the data from the surface profiles of the craters, reported in the previous chapter. The profiles are created on a white-light interferometry surface profiler (MicroXAM, 2003). The native data format of the system was not described in detail, thus an export of the data was required in a standard text format. The files obtained in this way could be readily processed with any spreadsheet software.

In order to filter out the noise in the data, a threshold value was introduced. The threshold was set at 1000 times the depth increment of the MicroXAM equipment. The depth increment was different for all data sets, but generally around 10^{-4} micrometers. Values, lower than the threshold, were disregarded in calculating the total volume of the debris.

Figure 5.7 shows a comparison between the volume of the craters for different laser powers, calculated on the basis of the simulation results from the previous chapter and the volume of the surface debris. There is a substantial correlation between the two graphs, although at the lower powers, the amount of debris is larger than the volume of the crater. This is obviously due to the fact that the model was also predicting less material removal (a smaller volume crater) at lower laser power levels, than in reality. At the 10W average power, over 70 % of the material taken away from the crater was deposited on the surface and re-solidified.

Figure 5.7 also contains a graph of the average height of formations above the top surface of the sample. It shows that the average height of the debris, has a lower dependence on the volume of the crater, and although there is smaller volume of molten material at the lower power settings, there is still debris with average height over 1 μm. The worst result was obtained from the highest laser power setting, and is over 2 μm.

These results show that, as expected, the effect of the debris and recast formations on the resultant surface topography is considerable. If we assume that the average height of the debris will transform directly in a real surface roughness, then the obvious

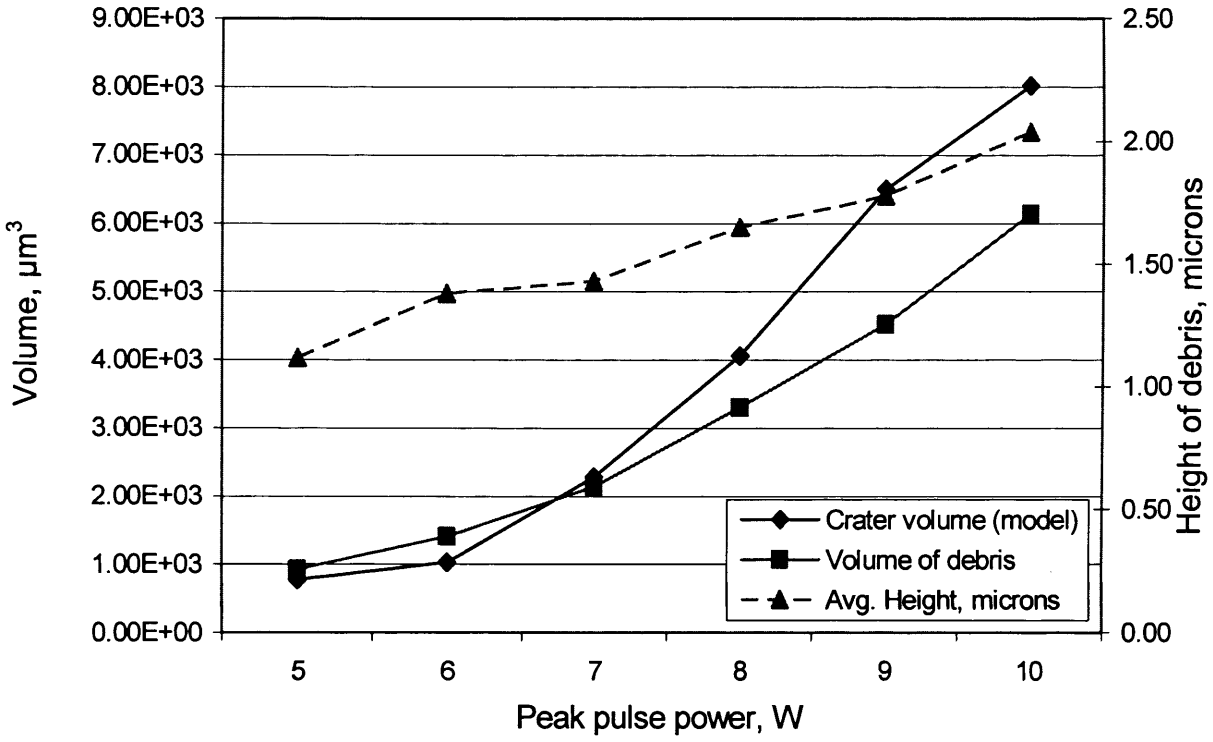

Figure 5.7 The volume of the craters for different powers compared to the volume of surface debris (stainless steel 316)

conclusion is that the less laser power is applied to the workpiece, the better the surface finish. Less power means, that there will be less material removed by a single pulse, therefore the overall time to finish a given job will increase.

5.2.2 Crater shape imperfection

In Section 5.1.3, it was discussed to recreate the surface topography resulting from the laser machining a single layer from the target. For the purpose of the simulation, an ideal shape, an approximation to the shape of the real laser pulse crater was used. Such an idealised shape made the simulation easier to handle and provided enough accuracy and information for the formation of the base surface.

Since in reality, the crater does not have the ideal shape, but a shape that varies from one pulse to the next, it is reasonable to introduce the difference between the ideal and the real shape as a factor that has a detrimental effect on the final surface roughness.

It is presumed that the random crater deformations are due to a couple of major factors:

- Non-uniform power distribution of the laser pulse
- Debris and recast formations in the crater

The last factor is associated with the debris and recast formations, which were discussed in the previous Section of this chapter. It is logical to assume that some of the debris that burst out of the crater, and then fall back down to the top surface of the substrate, some of them will fall back in the crater itself, and re-solidify there.

The first factor has to do with the quality of the laser source and the optics that are employed. The intensity distribution of the Nd:YAG laser is presumed to have Gaussian distribution in space, but the quality and age of the laser source generate distortions in the spatial profile of the laser beam. The quality of the optics, such as lenses and mirrors, introduces additional deformations, which further distort the beam profile (see Figure 5.8).

The overall result is that the shape of the craters will greatly affect the final surface finish that can be obtained from laser machining. The effect of the debris is still random in its nature, and the measurement of the laser beam profile requires expensive equipment, that was not currently available. This compelled the use of other means to assess the effect of the crater deformities on the resulting surface topology.

Since only the bottom portion of the crater cross-section is of interest (see Figure 5.9), which constructs the final surface following the overlapping from the neighbouring craters. This type of measurement is very subjective, because the boundaries of the bottom surface of a crater are assigned arbitrarily by the user. Thus, the following rules were introduced for the measurement of maximum and minimum points inside the crater itself. Firstly, the minimum is easily located, as it is the lowest point of the crater. Second, the maximum is the highest value where there is a change in the sign of the gradient of the curve below the surface level (see Figure 5.9).

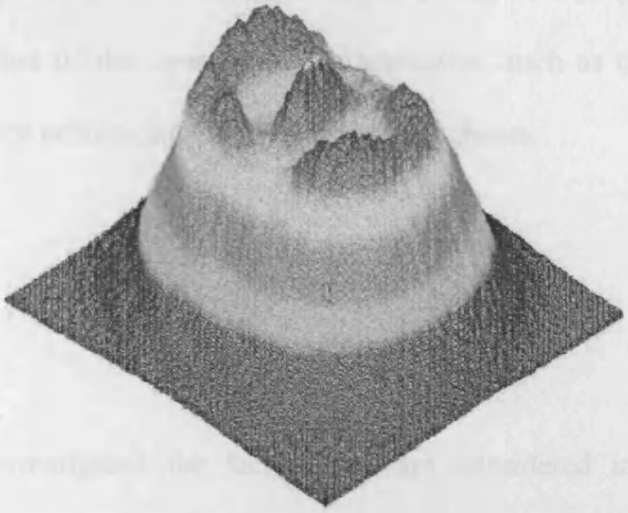

a). Measurement of real laser beam profile (Spiricon Inc, 2003)

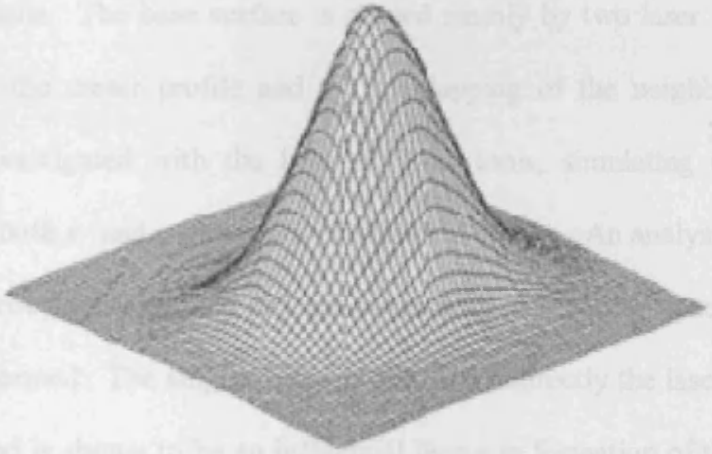

b). Ideal Gaussian beam profile

Figure 5.8 Laser beam intensity profiles

An example of the minimum and the maximum points in the cross-sections of two craters created with different laser powers is shown in Figure 5.9. Although, the difference for both power levels is not considerable (around 0.5 μm), it still becomes obvious that the effect of the laser beam characteristics, such as optical focus and power distribution, are influencing the final surface roughness.

5.3 Summary

This chapter has investigated the factors that are considered influential in the formation of the complex 3D surface topography resulting from laser machining. The factors are separated in two groups: formation of the base surface and secondary surface formations. The base surface is shaped mainly by two laser milling process characteristics: the crater profile and the overlapping of the neighbouring craters. These were investigated with the help of CAD tools, simulating the operational overlapping in both *x*- and *y-directions* of idealised craters. An analysis of the effects on the surface roughness of such process parameters as scanning speed and hatching distance is performed. The single crater profile, and indirectly the laser power, is also investigated, and is shown to be an influential factor in formation of the base surface topography.

The secondary surface formations generally refer to factors that are detrimental to the surface finish achieved in laser milling. The factors studied here are volume and size of debris and recast formations, and the crater shape imperfections. The volume and height of the debris and recasts deposited around the single crater is measured and compared to the volume of the crater. The crater shape itself, inherits

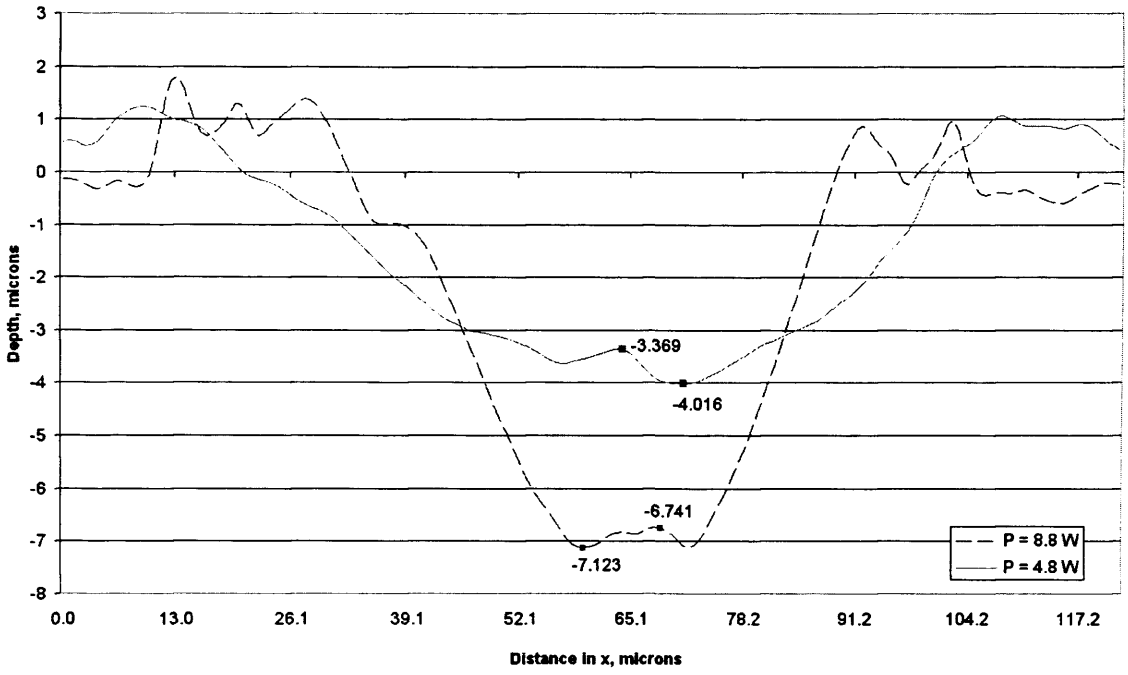

Figure 5.9 Crater cross-sections from two different pulse powers

a considerable distortions compared to the idealised crater used earlier. The quality of the laser beam and the optical properties of the beam path contribute to a deformed power distribution that plays an influential role in the formation of the crater achieved through laser milling.

Chapter 6 Cleaning of laser machined surfaces

So far, the work presented has concentrated on the laser machining process and the direct results from the interaction of the laser beam and the target material. The previous chapter presented 3D surface considerations from the laser beam traversing the topmost surface of the substrate, such as crater overlapping, debris and recast formations. This chapter will introduce cleaning techniques for removing the debris and contamination from the sample, thus further improving the surface quality of the finished product. Four diverse techniques will be investigated here: laser "cleaning", ultrasonic cleaning, deoxidisation (or *pickling*), and electro-chemical polishing.

6.1 Laser cleaning

6.1.1 Description of the process

Laser cleaning is founded on the same principles as laser milling, but instead of having the target material in the focal point of the laser beam, an offset is introduced to the extent that there is not enough fluence for material removal (Tam et al, 1992; Shao et al, 2005; Hsu and Lin, 2005). The substrate material is only heated enough to reach the melting point for the given material and in this fashion any debris and other recast contaminants are "flattened".

Figure 6.1 presents the set-up for the normal laser ablation operation, when the laser beam is focused on the top surface of the substrate, in order to achieve a maximum power density which is sufficient to raise the temperature of the material to the boiling point. Any deviation from the accurate focal distance normally results in a decrease of the volume of material that is removed from the target, thus this has a detrimental effect on the outcome characteristics of the laser milling process. Since this is usually an undesirable effect during normal laser milling, there is an optical sensor system that measures the distance to the top surface and modifies the power output of the laser system so that it produces a constant removal rate.

Laser cleaning actually operates the system in this defocused state (see Figure 6.1). This way, the laser beam does not reach enough power density to essentially perform material removal, but only to soften the top-most surface layer and any debris that were deposited from the machining of the previous layer. Therefore, this technique is best used as the last layer when machining a feature, or applying it when the laser beam follows the border cuts (see Figure 2.7). The two options cover potential features created with laser milling from all possible sides. The last layer to be machined forms the bottom surface of the features and the sidewalls are cleaned with border cuts operating the cleaning technology. Nevertheless, the cleaned sides will always display a fraction of the improvement that is achieved on the flat surfaces, because of the inherent problem with laser ablation, also responsible for the draft angle on the sidewalls.

In order to further investigate the surface roughness improvement that can be achieved with the application of the laser cleaning technique, a straightforward experiment was carried out.

6.1.2 Experimental set-up

The presented experiment was developed to investigate the effect on the surface roughness that can be achieved from laser cleaning. The experiment focuses only on flat bottom surface of the feature geometry, because sidewalls and inclined surfaces are always disadvantaged when laser ablation is employed.

The materials to be used in the experiment were chosen to be stainless steel 316 and industrial copper. The initial target surface was polished under R_a = 0.5 μm to avoid any inheritance from the original surface topography to the surface roughness of the machined experimental features. The materials were chosen for their different laser milling characteristics: 316 usually produce a better surface finish than copper, though it produces and retains more recast layer and debris. In order to avoid the effects of the recast layer and debris on the final surface roughness, both materials are cleaned in an ultrasound bath before the measurements are performed.

The experiment variable is the offset of the focal spot from the topmost surface of the target. The focal offset is varied from -3 mm to 3 mm. The assumed reference surface finish is measured on the experiment patch with the offset equal to zero, which is the normal machining operation of the system. To obtain the best settings for parameters of the laser milling system, an optimisation set-up session is carried out on

each material workpiece. The optimisation starts with some already established parameter values for the given material, and the system is then run on the workpiece for a number of layers. With every given number of layers, the machined depth is measured, providing the average material thickness removed per layer. The aim is to achieve a stable layer thickness, usually equal to 2 μm. The optimised laser settings for both experiment materials are given in Table 6.1. The physical and thermal properties of the two materials are given in Table 3.6 and Table 4.1 for copper and stainless steel respectively.

Under review, the greatest difference in the thermal properties of both materials comes from the thermal conductivity. The thermal conductivity of copper is 4 times larger than the one of stainless steel 316. This can explain the considerable difference between the machining parameters of the laser milling process for the two target materials. Specifically, the average laser power applied to machine copper is significantly less than that used for the stainless steel. The pulse frequency and scanning speeds for both materials also differ with a factor of 4. Again the stainless steel utilises the higher setting of 400 mm/s compared to 100 mm/s for the industrial copper. Thus in order to properly machine stainless steel, in comparison to copper, the laser milling process needs more powerful pulses, with a shorter pulse period and scans along the workpiece surface at a higher speed. If one considers only a single crater, neglecting the laser frequency and the scanning speed, one can see that in order to remove the same amount of material, the process applies four times the average power.

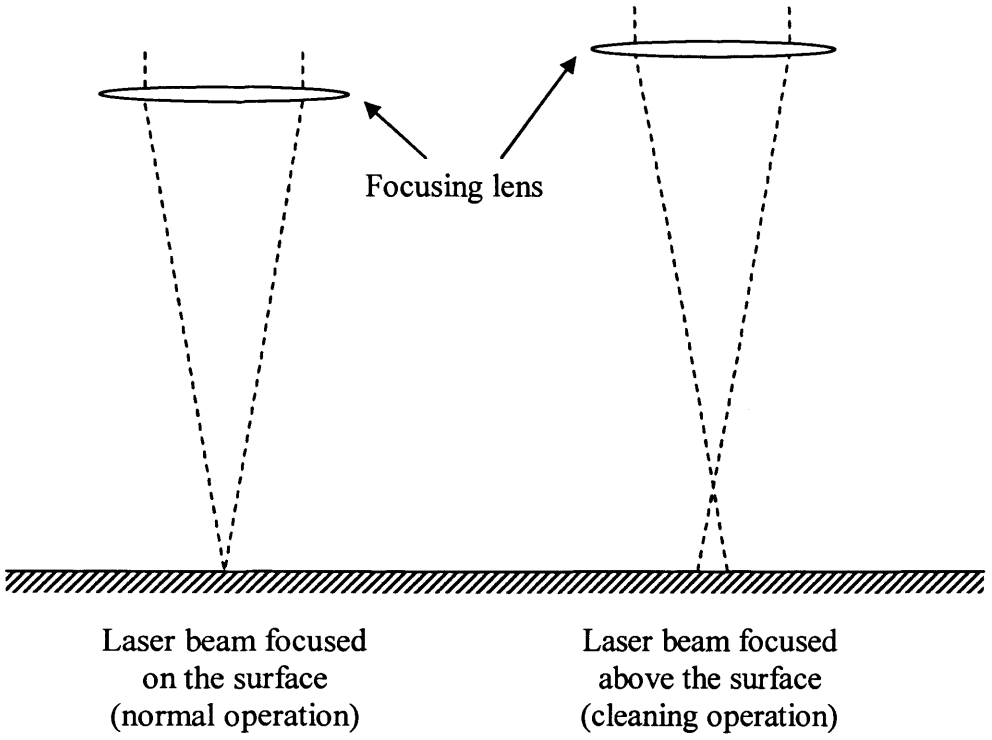

Figure 6.1 Normal and cleaning operation of the laser milling system

Parameter	Industrial Copper	Stainless steel 316
Laser flashlamp current, I [%]	59.6	71
Average laser power P_{av} [W]	2.36	7
Frequency f [kHz]	10	40
Scanning speed V [mm/s]	100	400
Pulse duration τ [μs]	10	10
Hatching distance [μm]	10	10
Sample size, mm	2 × 2	2 × 2

Table 6.1 Laser milling settings for the focal spot offset experiment

The following section presents the results obtained from the performed experiment on the effect of the offset of the laser focus on the surface roughness obtained from laser milling.

6.1.3 Results

The proposed experiment was carried out successfully. A total of 9 test patches were machined on each test workpiece. The surface roughness was measured at two different locations for each patch on the MicroXAM surface profiler.

Figure 6.2 introduces the average surface roughness obtained from the two experiment materials: stainless steel grade 316 and industrial copper. As expected the average surface roughness achieved on the copper is higher than what was measured on the 316. The lowest values acquired on both the copper and the 316 are R_a = 4.98 μm and R_a = 1.7 μm respectively. Also both graphs exhibit different characteristics. The graph for the surface roughness of the stainless steel is almost symmetrical around the zero offset, while the copper is asymmetrical.

The best result R_a = 4.98 μm, measured on the copper was with the offset equal to – 2 mm. Nevertheless, it is marginally better than the one measured for the normal operational offset. It is important to emphasise the fact that the graph does not show a similar result for the offset equal to + 2 mm. As can be seen on Figure 6.2 the stainless steel graph is closer to symmetrical about the zero offset, which is reasonable

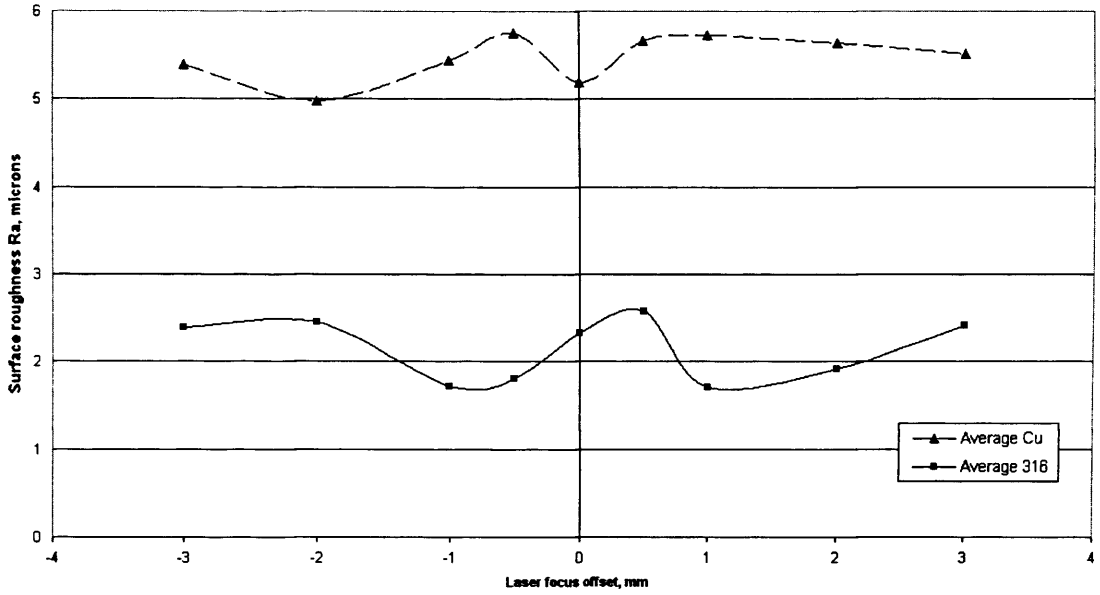

Figure 6.2 Surface roughness vs. the offset of the laser focal spot

to expect from the symmetrical optical de-focussing process. The copper's surface roughness is so high that the effect of the de-focussing is actually the opposite, instead of improving, there is a marginal increase in the measured roughness. This is the other significant difference between the two materials: while the copper sample has one of the best results at the zero offset, and its surface finish generally deteriorates as you move away from it. Contrary, the stainless steel measurements shows that there is a maximum in the middle of the graph, around the zero, then the graph drops indicating an improved surface roughness at the ±1 mm offset with around 27 % improvement. Going further out it becomes obvious that the effect of the de-focussing on the roughness decreases and it returns to the reference value.

Figure 6.3 introduces the 3D profiles from the surface roughness measurements of the reference (0 mm) and -1 mm patches. Under inspection the differences between the two regimes becomes obvious, and especially the effect of the de-focussed laser on the final target topography. The difference in the surface roughness can be observed in the more smooth profile of the -1 mm patch compared to the coarse and irregular reference.

This effect can also be observed in Figure 6.4, which presents line profiles taken from the same patches as in Figure 6.3. The line for the reference test is again erratic and irregular as opposed to a smoother line from the -1 mm patch.

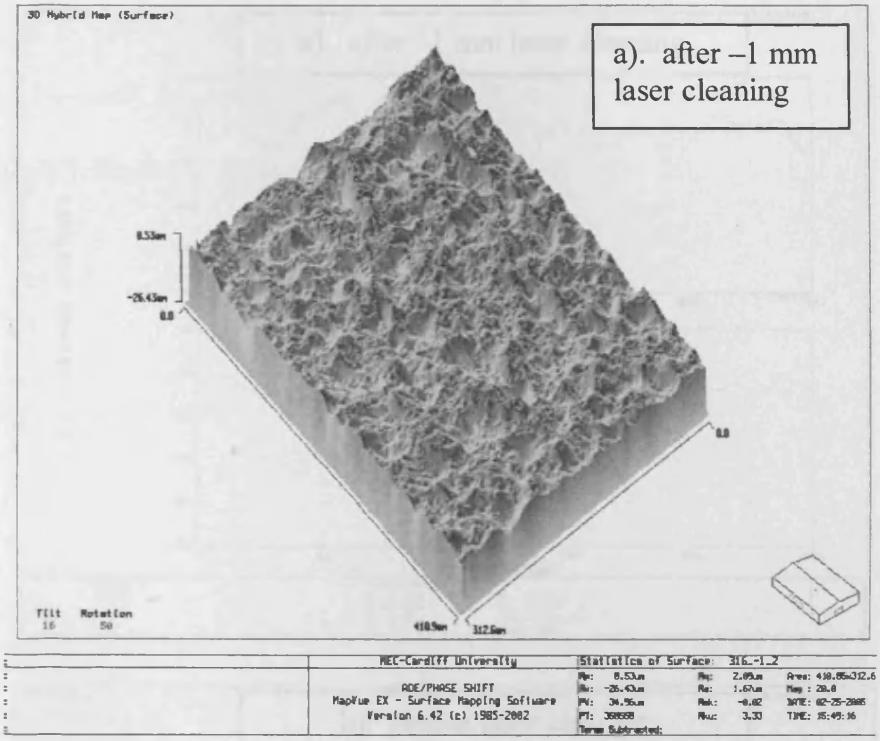

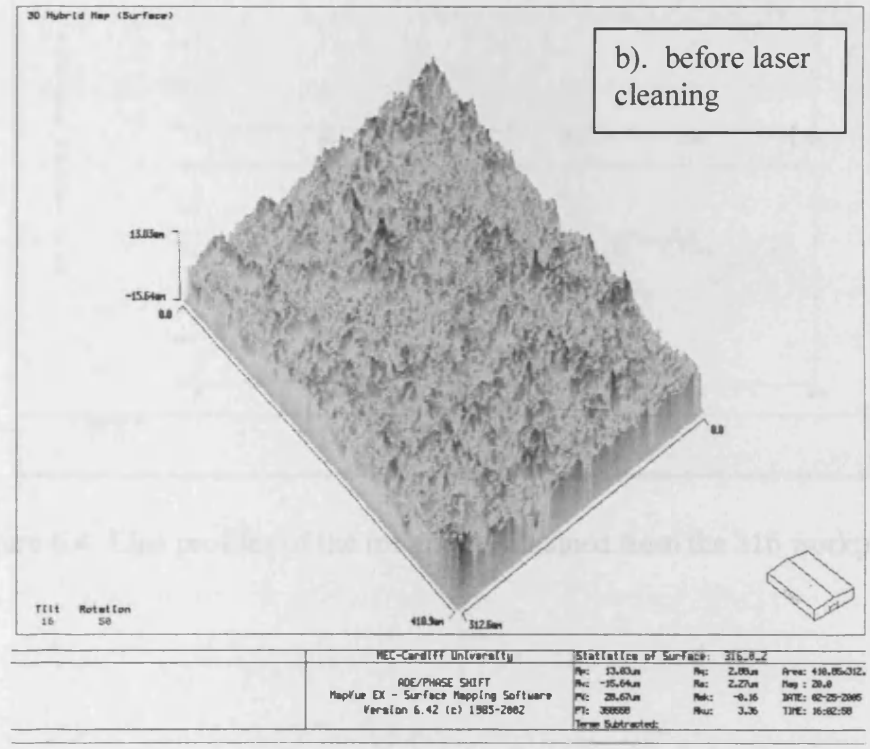

Figure 6.3 3D surface profiles of stainless steel 316

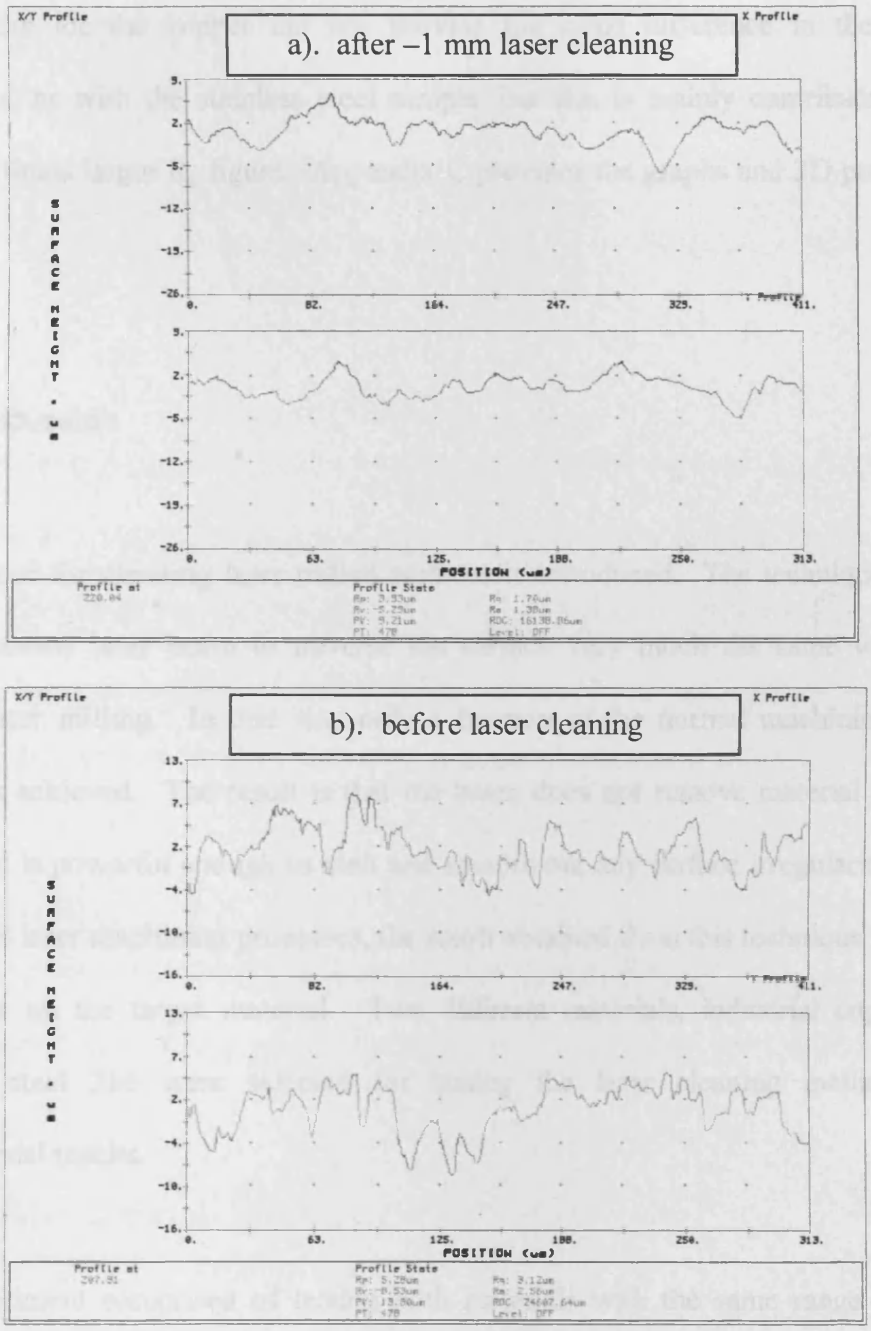

Figure 6.4 Line profiles of the roughness obtained from the 316 workpiece

The results for the copper did not provide the same difference in the surface roughness, as with the stainless steel sample, but this is mainly contributed to the almost 3 times larger R_a figure. Appendix C provides the graphs and 3D profiles for copper.

6.1.4 Discussion

A technique for cleaning laser milled surfaces is introduced. The technique utilises the de-focused laser beam to traverse the surface very much the same way as in normal laser milling. In that way only a fraction of the normal machining power density is achieved. The result is that the beam does not remove material from the target, but is powerful enough to melt and smooth out any surface irregularities. But as with all laser machining processes, the result obtained from this technique is highly dependent on the target material. Two different materials, industrial copper and stainless steel 316 were selected for testing the laser cleaning method, with controversial results.

The experiment comprised of testing both materials with the same range of focus offset, considering the reference point for examining the results to be the offset equal to 0. The range selected for the offset was from -3 to +3 mm. The laser settings were selected for each material based on an optimisation technique, aimed at achieving a stable and uniform laser milling process. The process parameters were not optimised for better surface roughness, in order to resemble normal machining conditions.

The results obtained from both materials, see Figure 6.2, provide an insight into the laser milling process. Copper produces a high surface roughness, and the laser cleaning has a small or no effect at all. On the contrary, the stainless steel sample attains a low surface finish, and then improves on it through the laser cleaning process.

Another difference between the two test materials is the expected symmetry in the effect of de-focussing the laser beam. Since this is an optical process, and the selected range for the offset was selected symmetrically around the normal focus distance for the system, it was expected that the experiment would produce symmetrical results. And the results from the stainless steel workpiece confirm this assumption. The copper, on the other hand, produced results with asymmetrical characteristics.

The laser cleaning technique is still a part of the laser milling process. The following sections introduce cleaning techniques that are applied post laser machining.

6.2 Cleaning and deoxidisation

All surfaces that have been machined with the long-pulse laser possess the same negative characteristic: oxidised recast debris. The range that is contaminated with such debris is not limited to only the machined surface, but it usually spreads around the machined feature and can reach or damage neighbouring structures. In order to clean this debris, two separate methods are described: ultrasound bath and chemical de-oxidation.

6.2.1 Ultrasonic cleaning

Ultrasound cleaning is an established process for removing micron-sized particles from an object without the need for additional cleaning agents. The ultrasonic cleaning operates by exerting mechanical oscillations of high frequency (Qi and Brereton, 1995; Goode et al., 1998). Ultrasonic cleaners used in manufacturing lines are mostly composed of an electrical oscillator and a mechanical vibrator. The mechanical vibrator, whose transducers transform an electrical signal into a mechanical vibration, is submerged in or attached to a cleaning tank that contains a cleaning liquid. The workpiece to be cleaned is immersed in the tank and a high frequency signal is run through the electrical oscillator (Kim et al, 1999).

The conventional ultrasonic cleaning methods depend on the mechanisms of high-frequency acceleration and cavitation in a cleaning liquid. There are two types of ultrasonic cleaning, depending on the frequency range that they operate. The first one usually operates in the range of several decade kHz and utilises cavitation to remove dirty particles up to several microns. In order to remove smaller particles, such as 1 μm or less, and to prevent cavitation damage to the workpiece, the second type of cleaners operate at much higher frequency, typically around 1 MHz. This type of ultrasonic cleaner employs high-frequency acceleration forces to separate and remove contamination. The second type is used for cleaning of photo masks production or silicon wafers in the semiconductor industry (Kim et al, 1999).

The diagram of an ultrasonic cleaner operated at 28 kHz is shown in Figure 6.5a. The high-frequency vibration of the vibration plate creates ultrasonic waves into the

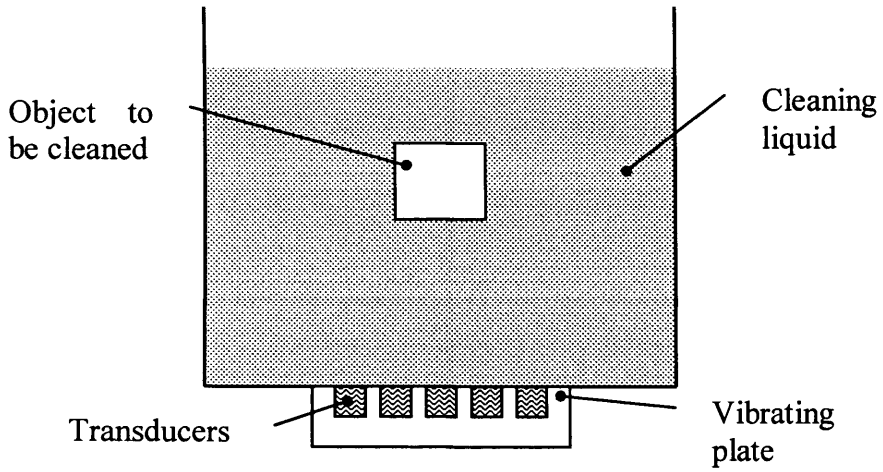

a). 28 kHz-range

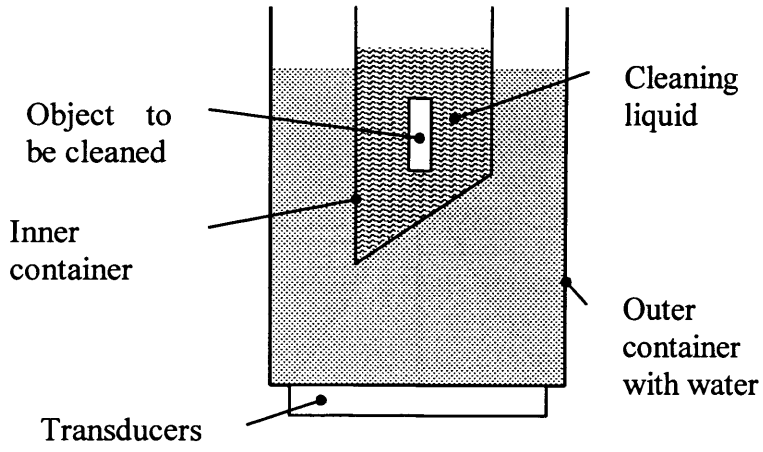

b). 1 MHz-range

Figure 6.5 Diagram of ultrasonic cleaners

cleaning liquid. When these waves reach the cleaning object, ultrasonic cavitation is generated on the object's surface. The pressure waves induce a succession of compression and expansion of gaseous micro-bubbles in the liquid and even micro-explosions occur on the object's surface. In this way, the unattached debris and contamination are separated from the object to be cleaned. The efficiency of the cleaning process depends highly on the magnitude of the acoustic pressure level (Flynn, 1964). But there is a drawback to using a very powerful ultrasonic generator, because high cavitation can have some undesirable effects on the surfaces of the workpiece.

On the other hand, the ultrasonic cleaner removing much smaller particles, such as 1 μm or less, and does not induce cavitation damage is operated at much higher frequency, around 1 MHz (see Figure 6.5b). This kind of cleaner relies on the high-frequency acceleration force and is used for example for the cleaning of photo masks or silicon wafers in the semiconductor industry (Qi and Brereton, 1995; Hatano and Kanai, 1996; Kuehn et al, 1996). As shown in Figure 6.5b, *megasonic* cleaning is performed in a megasonically-exited liquid enclosed in a double container, whose inner container is made of a non-metallic material such as fused quartz or Pyrex glass so as to isolate the cleaning object from the metallic ions. The megasonic waves generated by the piezoelectric transducers propagate in the outer container and are transmitted through the inner container. The bottom of the inner container is inclined to make oblique incidence of the megasonic wave in order to raise the efficiency of the wave transmission through the bottom plate (Hatano and Kanai, 1996).

The ultrasonic bath utilised in this research is of the 28 kHz type. The workpiece to be cleaned is suspended in a single tank, and ultrasonic generator is actuated underneath outside of the tank. Optional temperature control is also available, for investigating the effects of raised temperature levels on the cleaning process.

Figure 6.6a presents the results from laser milling a 4 mm side square. The resulting feature is surrounded with debris and its bottom surface and the sides are covered in recast material, deposited there during machining. The distance range of the debris is considerable and exhibits a deposition tendency in the direction away from the viewer when looking at Figure 6.6a. In fact, this misleading debris orientation is created from the suction device which is positioned close to the machining area in order to remove some of the material ejected during machining.

Figure 6.6b on the other hand displays the same feature after ultrasonic cleaning. The workpiece was immersed into an ultrasonic bath for 5 minutes. The cleaning liquid was water with industrial degreaser added to remove oils or lubricants and further improve the cleaning process. After completing the cleaning cycle the workpiece was rinsed with water and then air-dried.

When comparing the two photos the effectiveness of the ultrasonic cleaning process is obvious. After cleaning the debris are removed completely, including the ones that were deposited directly on the machined surfaces, where the debris was probably fused solid to the base surface, which is now clearly improved. The edges of the feature are also improved and are now noticeably sharper and defined.

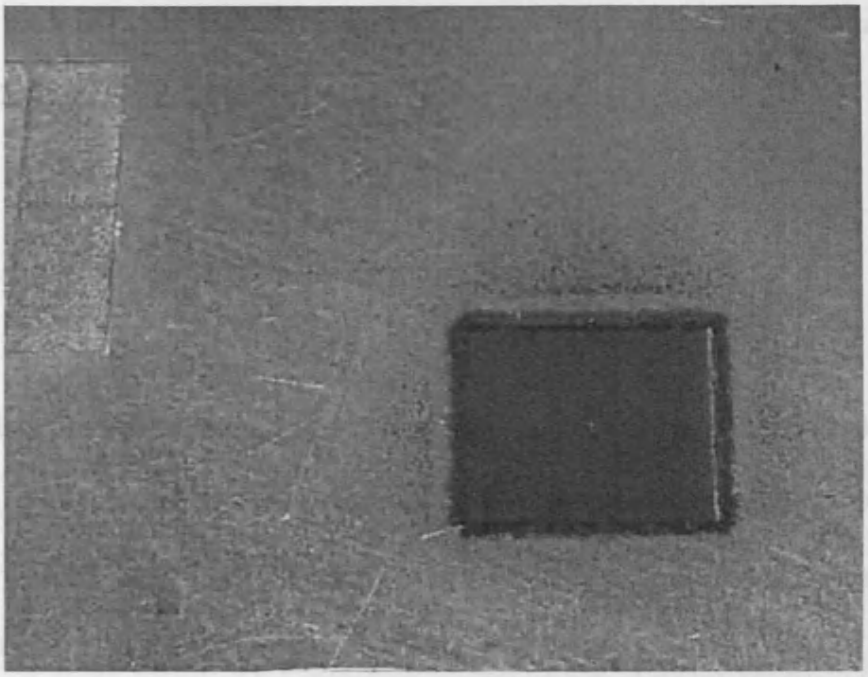

a). without cleaning

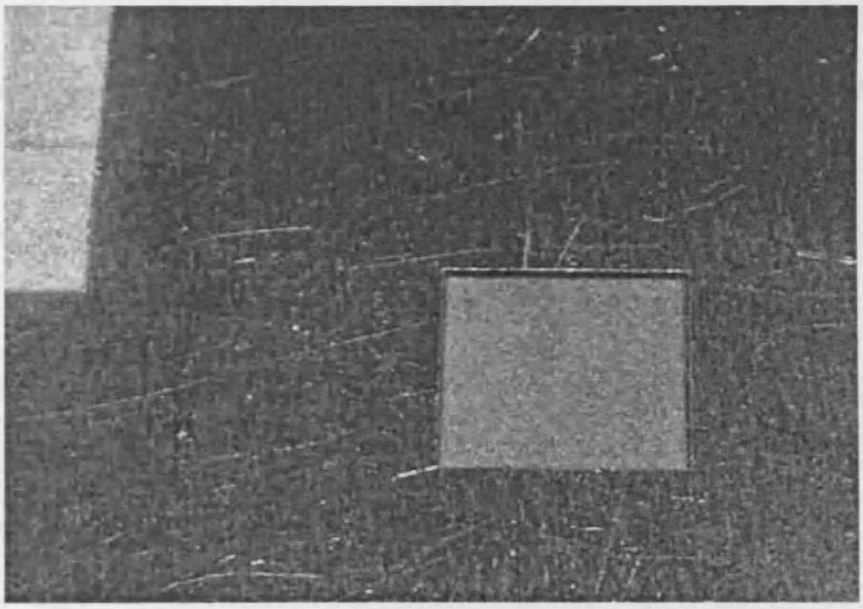

b). after cleaning

Figure 6.6 Laser milled feature before and after ultrasonic cleaning

Although, the quality of the machined surfaces is greatly improved from the ultrasonic cleaning, they are still covered in recast oxidized layer, which is much harder and more difficult to remove.

6.2.2 Chemical deoxidisation (pickling)

Pickling is a term describing a collection of industrial processes aimed at cleaning or removing oxide scales and chromium-depleted layer that forms on the surface of industrial metals (most common is stainless steel) during their processing at high temperatures. Pickling consists of mechanical, electrochemical and/or chemical operations (Li and Celis, 2003; Li et al, 2005). Generally, metals are immersed into solutions of acids which react with metal, metal oxides, heat-treat scale (e.g. from welding) and foreign metals and the resulting salts are subsequently removed from the metal surface through brushing. The chemical reactions between metal, oxide and acid can be described as follows (Rudy, 2002):

Metal Oxide + Acid = Metal Salt + Water

Metal + Acid = Metal Salt + Hydrogen (proton)

Hydrogen (proton) + Hydrogen (proton) = Hydrogen (gas)

The metal substrate, as is, has an oxide surface layer before immersion in the pickling bath. This condition was probably accentuated by a previous thermal operation performed on the metal substrate. The oxide layer hurts the prospective finish in two ways: adhesion of electrodeposits to the base metal will be poor, and the metal surface in an oxide condition is a poor conductor. The oxide must be totally removed without

introducing any damage to the rest of the structure. Depending on the degree of surface acid treatment, this can be done in a single immersion, double immersion, or cathodically in an electrified acid. Acid formulations, available in liquid or powder, are available in three common forms:

- Single constituent, mineral, inorganic type
- Combination of two or more acids. May consist of inorganic and organic acids
- Single or multi-acid combinations, which also contain surfactants, dispersants, and inhibitors.

The acids dissolve the oxides and other thermal debris contained in the surface layer. They can also remove scales and rusts. Sulphuric acid (H_2SO_4) is perhaps the cheapest of the acids used and has reduced fumes. Hydrochloric acid (HCl) provides a much better rate of pickling action at lower temperatures but does generate more fumes. Phosphoric acid (H_3PO_4) must be heated to achieve acceptable pickling activity, and formation of light iron phosphate films on the surface may be detrimental to subsequent electroplating step.

Surfactants and wetting agents lower the solution surface tension, permitting the bath's active agents to more readily penetrate into and attack undesirable surface coatings and films. Other beneficial functions include emulsification of residual oils and grease (not removed in previous alkaline cleaning or carryover) and the formation of a thin surface foam blanket to help retard the corrosive effects of fumes and mists. Dispersants prevent redeposition of removed soils. Inhibitors provide two-fold effects:

controlled pickling, which prevents excessive surface action, and prevention of immersion deposits in aged, contaminated baths.

The pickling process is similar, but should not be confused with the electrochemical polishing process. The differences and the effects of an industrial pickling solution on a stainless steel substrate will be discussed later as a part of an experiment for identifying the effects of electrochemical polishing on laser milled microstructures.

6.3 Electro-chemical polishing

The electro-chemical machining (ECM) process is based on the principle of anode metal dissolution in an electrolyte (Wilson, 1971). The process was first introduced in 1929 and proved to be exceedingly advantageous for high-strength and high-melting point alloys. Industrial applications have been expanded to electro-chemical drilling, deburring, grinding and electro-chemical polishing (Tam et al., 1992).

Electro-chemical polishing is a process of improving microsmoothness (microgeometry) and brightness by anodic dissolving of the substrate in an electrolyte with an external source of electricity (Rudzki, 1983). The basic mechanism of electro-chemical polishing is immersing a metal target into a chemical solution and making it the anode in a direct current circuit. The process is highly dependable on the ability of the solution to polish only the external (outer) surface of the material without the occurrence of corrosion pits, to penetrate the substrate, as occurs during the etching process.

There is considerable interest in the electrolytic and chemical processes for the polishing of metallic surfaces. The most common commercial application areas are for polishing components made of aluminium, stainless steel, brass, nickel and silver, generally components which are difficult or expensive to polish mechanically (Hocheng and Pa, 2003). The beneficial effects of industrial electro polishing of a workpiece are threefold (Kao and Hocheng, 2003). Firstly, *micropolishing* – the removal of the irregularities on the surface of about 0.01 mm in size making the component's surface more reflective and bright, while the smoothness of the surface might not get improved. Second, *macropolishing* – the removal of irregularities larger than 0.1 mm in size, provides a smooth surface, but does not guarantee the attaining of brightness. And third, *passivation* – as a result a chemically passivated layer is produced, which can not be obtained through any mechanical polishing process.

Electro-chemical polishing does not "flow" the surface, as happens in mechanical polishing, thus surface defects such as deep scratches, machining marks and flaws in the metal, will not be removed through electro polishing.

The electro-chemical polishing process may be linked to electroplating in reverse, because it requires the same equipment setup: tank, solution and low voltage direct current provided by a rectifier. There is one essential difference between the two processes: in electropolishing the components are made the anode in the circuit, while in electroplating they are the cathode.

As with electroplating, electro-chemical polishing is generally applied on macro-scale components, and the application of the process for improving the surface finish of laser milled surfaces poses a considerable challenge. The macro-scale electropolishing process depends on a uniform material structure, freedom from surface inclusions and good consistent surface finish all over the component. In contrast, laser milled features are mostly depressed into the material, with worse surface roughness than the rest of the component and a significant presence of foreign or recast particles on the surface. Thus, it is important to investigate in detail the effects of electrochemical polishing on microstructures machined by laser milling.

6.3.1 Electro-chemical polishing of microstructures

Electro-chemical polishing is a process that has the potential to improve considerably on the surface finish obtained from laser milling. There are a number of factors that need to be considered when investigating the achievable improvement and the effect that the polishing will have on the surface topography. The major factors that influence the electro-chemical polishing are micro-scale features, temperature control, solution agitation, duration, and external source of electricity.

The micro features factor is related to the recessed features resulting from laser milling. The micro-size will further inhibit the polishing process on the surfaces of interest. The small size will prevent the access of a fresh solution to the target area, and will result in an adverse concentration of the dissolved material. The higher the concentration of the target ions in the solution (i.e. the solution becomes "dirty"), the

less effective the polishing process becomes, and this could lead to local overheating of the substrate.

The electrolyte of every electro-chemical polishing system has a definite range of optimum operating temperature. A decrease of the temperature below this range could lead to an increase of the viscosity of the electrolyte, thus obstructing the diffusion of the dissolved products into the electrolyte and the supply of fresh electrolyte.

Agitation of the solution is a multipurpose factor that can decrease the effects of the micro-features. It can provide the following advantages (Rudzki, 1983): 1). improve the supply of fresh electrolyte to the micro-recesses; 2). eliminate the undesired concentration of the dissolved material at the substrate; 3). stimulate the release of gas bubbles from the polished substrate which may cause, e.g. pitting; and 4). prevents local overheating of the workpiece.

The duration of the electro-chemical polishing depends on the initial workpiece material and conditions, and electrolyte composition, amongst other factors. Excessive electropolishing does not produce a significant improvement of the surface quality and actually sometimes may even produce the opposite effect. There is also a relationship of the duration of the process to the current density. Typically, an increase of the current density will shorten the electropolishing time.

In practice the ECP is controlled by the current density provided from the external source of electricity. The anodic current density is given as $c.d. = I/S$, where I is the electricity current in [A], S is the surface of the anode workpiece in [cm^2].

Figure 6.7 presents the setup used for the electro-chemical polishing experiments. The DC power supply provides a variable voltage from 0V to 32V with a direct current up to 12 A. The voltmeter is used for setting the operational current thus controlling the current density applied to the anodic workpiece. There are a number of methods to control the surface area of the anode. One is to selectively cover the workpiece with an acid-resistant compound, and only leave open a precise area of interest. In order to resemble the electrochemical polishing process of a macro component with micro features as close as possible, the workpiece is not covered, but selected to a specific size that corresponds to optimum current density.

The workpiece material selected for the experiment was 316 grade stainless steel in 2 mm thick sheets. The 316 stainless steel was chosen due to the good electro-chemical polishing capabilities of the material and the fact that there are numerous recipes for the polishing electrolyte. The sheet material was cut to 2 cm square providing a total anode surface area equal to 9.6 cm^2. The faces of the workpiece were mechanically polished to give a very good initial surface finish (average $R_a = 0.11$ μm).

There were two types of features selected for this experiment. One was a large area shallow feature, designed to provide the true efficiency of the electro-chemical polishing on a laser milled surface. On the other hand, the second feature was designed to investigate the specific effect of electro-chemical polishing on deep

micro-sized features. The second test feature had a smaller area and was deeper achieving a higher aspect ratio. The rationale behind this choice of features was to obtain the effects of the process on micro-sized lateral dimensions especially in deeper structures, where there is constrained agitation of the polishing solution thus impairing the electro-chemical polishing.

The solution agitation is provided by the electromagnetic stirrer (see Figure 6.7). The stirrer was also equipped with a ceramic hotplate, providing a temperature control for the electro-chemical process. The electrolyte together with the cathode in place is brought to the desired temperature before introducing the workpiece and commencing the process.

The material selected for cathode was industrial copper. A sheet of copper was shaped in a 3-cm wide strip and then rolled to obtain a ring smaller than the beaker diameter. In this way, the workpiece could be placed in the middle of the beaker and be surrounded with the cathode from all sides, providing a uniform electrical potential from all sides. Also the shaped cathode gave space for better agitation surrounding the 316 workpiece.

All test structures were machined on a single 316 workpiece, and the laser milling settings are provided in Table 6.2. After machining, the workpiece was cleaned in an ultrasonic bath for 6 min at room temperature.

The next step was to remove the oxides and other contaminants by immersing the experiment workpiece in a pickling solution (Anopol Ltd., 2000). The chemicals

Parameter	Stainless steel 316
Laser flashlamp current I [%]	68.8
Frequency f [kHz]	40
Scanning speed V [mm/s]	400
Pulse duration τ [μs]	10
Hatching distance [μm]	10

Table 6.2 Laser milling process parameters

were obtained in ready to use form (nitric acid HNO_3: 20 %; Hydrofluoric acid HF: 7 % and additives) The setup employed was the same as with the electro-chemical polishing (see Figure 6.7) except for the use of electrical current. The duration of the pickling process was set to 10 minutes at room temperature. Subsequently, the test piece was rinsed and air-dried prior to all measurements. Surface roughness measurements were taken from the experimental structures for comparison.

For the electro-chemical polishing process, the workpiece was submerged in a ready to use solution with the following composition (Anopol Ltd, 2000): sulphuric acid: 15% to 50%, phosphoric acid: 25% to 60%. The solution was at 55 deg Celsius during the polishing experiment. The duration of the process was set to 10 min at a voltage providing anodic current density of 20 A/dm^2. The polishing duration was selected after some preliminary polishing trials, and proved to achieve good results on stainless steel. After completing the process, the workpiece was again rinsed and air-dried. Consequently, a new set of measurements were taken from the experimental surfaces on the interferometry surface profiler.

6.3.2 Results and discussion

The experiment was carried out following the laid out plan. Table 6.3 provides the results from the surface roughness measurements of the experimental features. There are three sets of measurements: non-machined surface (mechanically polished), 5 mm square and 0.5 mm square.

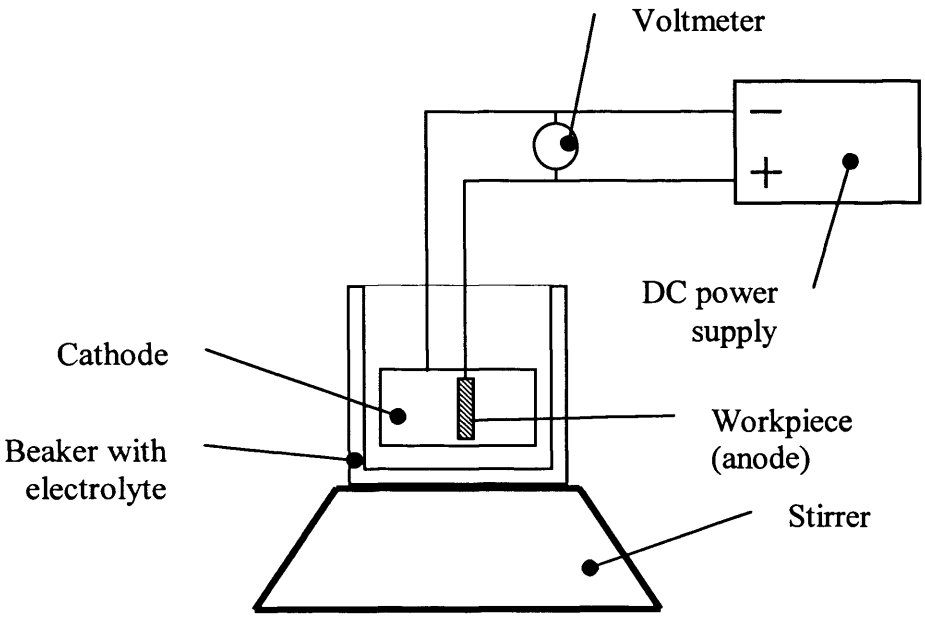

Figure 6.7 Cross-sectional diagram of the electropolishing setup

	Non-machined surface	**5 mm square**			**0.5 mm square**		
		Test 1	**Test 2**	**Test 3**	**Test 1**	**Test 2**	**Test 3**
Initial (Ultrasonic bath)	0.11	1.83	1.76	1.86	2.43	2.60	2.54
Pickling	0.17	1.63	1.69	1.78	2.46	2.63	2.44
ECP	0.14	0.92	0.77	0.88	1.92	1.69	1.71
Average improvement, %		53			30		

Table 6.3 Results from surface roughness R_a [μm] measurements

It is important to emphasise on the results obtained from the mechanically polished surface. The surface roughness in this case actually did not improve, and in fact shows a slight increase. The initial roughness is equal to 0.11 μm and it rises to 0.17 after the pickling process. The electrochemical polishing improves to some extent and gives the final value of R_a = 0.14 μm. The explanation for this effect is separated between the two cleaning processes. First the pickling process is not really expected to improve the surface roughness and by removing scales and oxides, it marginally worsens the initial polishing. The electro-chemical polishing on the other hand, is highly effective in a given range of surface finish, and with the low value provided from the preceding mechanical polishing process, the electrochemical process can only provide a little improvement.

In contrast, the 5 mm square shows a good improvement of the surface resulting from the ECP process. Although, there is a marginal improvement from the pickling process, the largest advance is provided from ECP. In total, the final surface finish is improved by 53% compared to the initial surface.

On the other hand, the 0.5 mm square has an even higher initial roughness R_a = 2.52 μm on average. Compared to the average 1.83 μm for the larger feature, this gives a starting point that is almost 30% worse. And the results obtained are in accordance, by only managing to reach an improvement of 30% when comparing the electrochemical polished surface and the original surface.

It has to be mentioned that due to the small size of the 0.5-mm features, there was a considerable shape deviation (see Figure 6.8a). Rather than obtaining a flat bottom

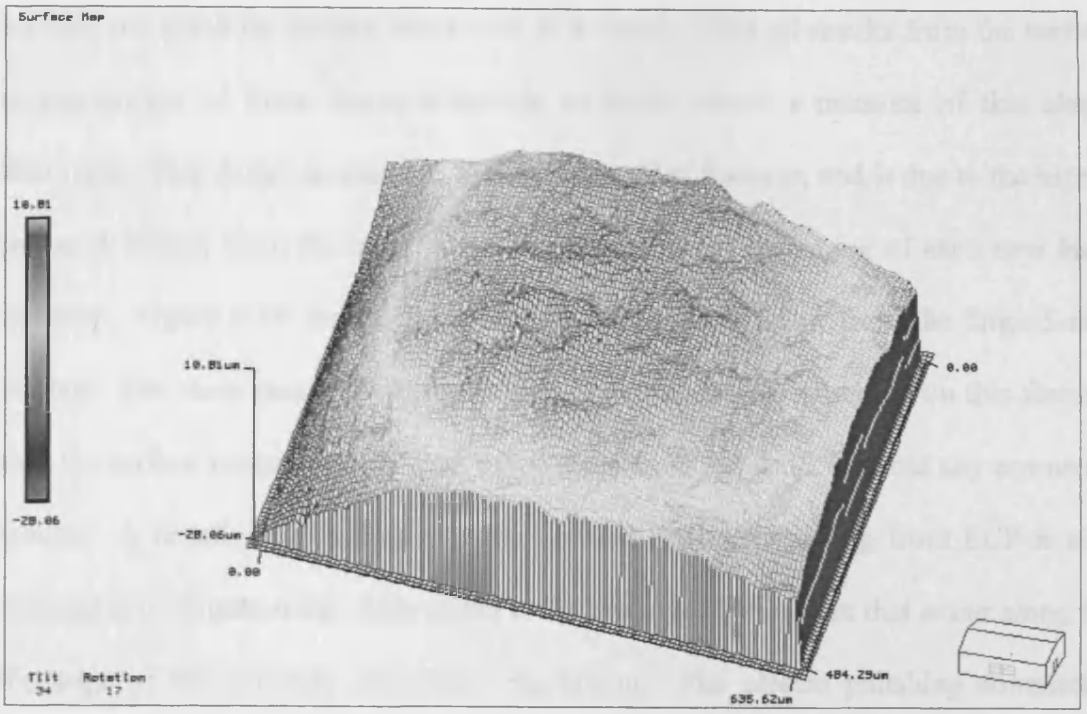

a). A bottom surface of the 0.5 mm test feature

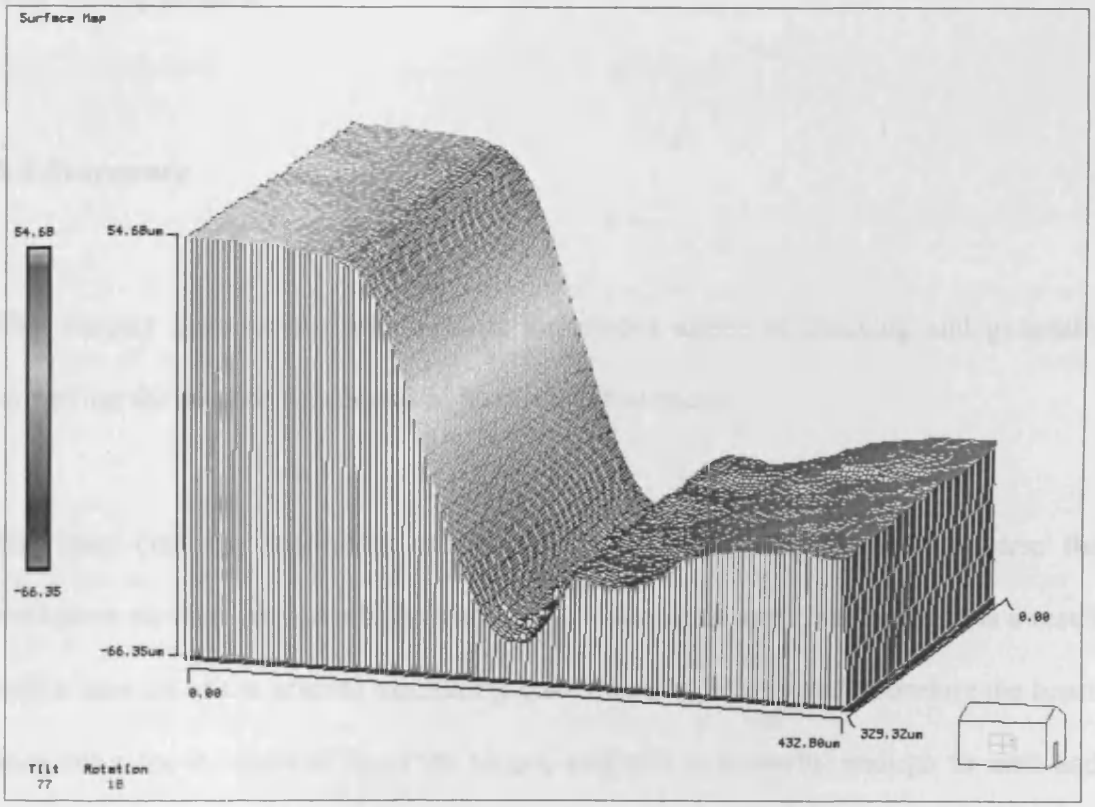

b). A side wall of the 5 mm feature

Figure 6.8 3D view of electropolished surfaces

surface, the resulting surface was closer to a dome. Thus all results from the surface measurements of these features include to some extent a measure of this shape distortion. This defect is common for all laser milled features, and is due to the higher power delivered from the laser to the workpiece at the beginning of each new laser traverse. Figure 6.8b shows a 3D view of a side wall taken from the large 5-mm feature. The same recess close to the side wall can be also observed on this feature, thus the surface measurements were taken away from the walls to avoid any erroneous results. A beneficial effect on the laser milled features resulting from ECP is also noticeable on Figure 6.8b. This effect is the removal of the burrs that occur along the top edge of the structure after laser machining. The electro polishing completely removes any burr formations, which are obviously an undesirable outcome from the laser milling process.

6.4 Summary

This chapter introduces four different techniques aimed at cleaning and generally improving the surface roughness of laser milled surfaces.

The laser cleaning technique utilises the de-focused laser beam to traverse the workpiece surface very much the same way as in normal laser machining. As a result only a fraction of the normal machining power density is achieved, therefore the beam does not remove material from the target, and still is powerful enough to melt and smooth out any surface irregularities. But as with all laser machining processes, the result obtained from this technique is highly dependent on the target material. Two different materials, industrial copper and stainless steel 316 were selected for testing

the laser cleaning method, with controversial results. An experiment was carried out on two test materials to investigate the effects of laser cleaning on the final surface roughness. Laser milling produces a high surface roughness on Copper, and the subsequent laser cleaning has a small to no effect at all. On the contrary, the stainless steel sample attains a lower surface finish, and then improves on it by the laser cleaning process with almost 30%.

Ultrasonic cleaning baths have been utilised in the semiconductor industry to clean debris and contaminants for some time now. In this chapter was demonstrated the application of such equipment to clean away the debris created from the laser milling process. The final result displayed a considerable improvement on the target surface by cleaning the test features and the surroundings without any detrimental effects, usually associated with mechanical cleaning or brushing.

The third process, pickling, is a chemical process through which the target surface is cleaned from various types of surface inclusions. Generally, metals are immersed into solutions of acids which react with metal, metal oxides and heat-treat scale. In this way, after pickling, the targets have surfaces that are free from any traces of foreign materials and can be easily electro-chemically polished. The process displayed a controversial effect on the surface roughness, but is required by the subsequent electro-chemical polishing process. On the other hand, pickling proved to be the best option for cleaning hard and difficult to remove recast layers formed on the target surface from the laser machining.

The electro-chemical polishing process is directed mainly at improving the surface roughness. Although, electro-chemical polishing displayed some restrictions when polishing micro features, it still managed to improve the surface by over 30 %. Nevertheless, the achieved improvement of the surface finish through electro-chemical polishing can provide high enough surface standards for laser milled micro features to satisfy the requirements of the micro-manufacturing processes.

ECP also improves on the edges of the laser machined structures by removing the burrs that are typically left from the laser milling.

Chapter 7 Contributions, conclusions and future work

7.1 Contributions

The laser milling process has been investigated against the requirements of the micro-replication processes. The set of requirements that were analysed in this work are:

- Surface finish
- Aspect ratio
- Accuracy
- Minimum feature size

The laser milling process was tested to identify its capabilities in the specified characteristics. The best surface roughness that was achieved in the presented experimental work was R_a = 1 μm, which was an improvement for the laser milling process, which usually produces R_a = 2 μm. However, the achieved roughness is still high for the replication processes, due to the fact that the polymer replication processes copy the surface topography almost perfectly. High surface roughness results in a texturing effect being replicated onto the components. It was concluded that further investigation is required to improve the surface finish produced by the laser milling process.

The aspect ratio that can be reproduced by hot embossing or microinjection moulding is much higher than laser ablation can give. Aspect ratios of 2.25 for gaps and 3 for walls are in the low range. Nevertheless, the achieved result is still impressive given

the tooling material used, and the fact that the only competition comes from the silicon based manufacturing processes, such as lithography.

The laser milling accuracy is proved to be highly dependent on the laser machining parameters and more importantly on the target material used. During the trials, the machined features were all within the expected tolerance of 50 μm, and copper proved to be a considerable improvement by achieving accuracy within a 25-μm tolerance.

The minimum feature size obtained from laser machining on the specially designed test structures made it obvious that the thermal nature of the laser milling process is the only obstacle to machining micro grooves and walls. However, the process was capable of machining vertical walls of 40 μm thickness with an aspect ratio of 3. The micro grooves proved to be more difficult, and the smallest width groves machined to the full depth were 80 μm.

The surface roughness was expected to be a strong challenge for the laser milling process. Thus, the factors and process parameters that govern the resulting surface topography were investigated in-depth. The average surface roughness achieved by laser milling is in the region of 2 μm, but this shows a high dependency on the type of target material used. A laser material interaction model of the material removal process is developed to investigate the influence of the process parameters. The model is based on the generation of heat in the target, resulting from a laser pulse. A numerical solution of the problem is applied and the obtained results were confirmed with a validation experiment on two different tooling materials. The results obtained from the crater depth experiments were in agreement with the simulation results for

both target materials. The simulation results were used to investigate the effects of laser pulses with different fluence levels.

The surface model provides a comprehensive view of the topography formation of the laser machined surfaces and is used to identify the effects and importance of the different laser milling parameters on the surface roughness. The parameters investigated are marking speed, laser pulse frequency and hatching distance, i.e. crater overlapping, as these are expected to be most influential on the formation of the more complex (3D) surface topography. The base surface formation is investigated with the help of 3D CAD models, providing an analysis tool for the operational overlapping in both *x*- and *y-directions* of idealised craters. An analysis of the effects on the surface roughness of such process parameters as scanning speed and hatching distance is performed. The single crater profile, and indirectly the laser power, is also investigated, and is shown to be an influential factor in formation of the base surface topography.

The secondary surface formations generally refer to factors that are detrimental to the surface finish achieved in laser milling. The factors studied here are volume and size of debris and recast formations, and the crater shape imperfections. The volume and height of the debris and recasts deposited around the single crater is measured and compared to the volume of the crater. The crater shape itself inherits considerable distortions compared to the idealised crater used earlier. The quality of the laser beam and the optical properties of the beam path contribute to a deformed power distribution that plays an influential role in the formation of the crater achieved through laser milling.

A number of techniques for cleaning and improving the surface roughness have been proposed and investigated: laser cleaning, ultrasound bath, deoxidisation (or pickling), and electrochemical polishing. The ultrasound bath and deoxidisation processes offer a non-intrusive means of cleaning the debris and recast layer left from laser milling. These processes proved to be powerful tools in cleaning the laser milled samples, and still preserve the sometimes fragile micro structures. More importantly, pickling proved to be the best option for cleaning hard and difficult to remove the recast layer formed on the target surface from the laser machining.

Laser cleaning is a process based on the laser milling principles, but with a set-up that positions the laser beam out of focus in the work plane. Thus, the laser only "irons out" the surface irregularities left from the preceding laser milling. The laser cleaning process produced controversial results and again the choice of the target material made the difference. Two materials were selected for testing the cleaning capabilities of the process, and the copper sample did not show an improvement of the surface finish after laser cleaning. The 316 stainless steel sample, on the other hand, shows an improvement of the surface roughness with almost 30 % at a laser offset equal to ± 1 mm.

Electrochemical polishing streamlines the microscopic surface of a metal object by removing metal from the object's surface through an electrochemical process. In very basic terms, the object to be electrochemically polished is immersed in an electrolyte and subjected to a direct electrical current. The object is maintained anodic, with the cathodic connection being made to a nearby metal conductor. Therefore, the

electrochemical polishing process is directed mainly at improving the surface roughness of laser milled features. Although, the ECP displayed some restrictions when polishing micro features, it still managed to improve the surface roughness by over 30 %. Nevertheless, the achieved improvement of the surface finish through ECP, can provide a low enough surface for laser milled micro features to satisfy the requirements of the micro-manufacturing processes.

7.2 Conclusions

Laser milling provides an efficient and highly competitive alternative to current micro-tooling processes, such as LIGA. The main advantages offered by laser milling are the capability to machine a wide variety of tooling materials, freeform 3D geometry and micro sized features.

When comparing the laser milling capabilities to the requirements raised from the micro-manufacturing process, it has to be concluded that although laser milling cannot compete with silicon-based tooling processes, it can still provide a competent alternative in the current market place.

The four major tooling characteristics considered in the present work pose a challenge that pushes the laser milling capabilities to its limits. Still the process provides an adequate accuracy and aspect ratio, while the feature size is more than satisfactory for the current target applications. The capability of manufacturing features with vertical walls is another advantage for laser milling. On the other hand, the surface finish proved to be an obstacle that required further investigation.

The proposed theoretical model was successfully applied to investigate the single craters created from a laser pulse. The crater profiles for two target materials were in agreement with the validation experiment. The modelling of a 3D surface, based on the crater profiles, provided a tool for investigating the effects of the scanning speed and the hatching distance, on the final surface topography.

Nevertheless, the laser milling process requires post-process cleaning to be performed. The four proposed cleaning techniques supply means for not only cleaning the debris and recast formations, but also improving the surface finish considerably.

7.3 Further work

A marked improvement on all aspects of the laser milling process is expected from changing the laser source to a lower wavelength and shorter pulse duration. Pico and femtosecond lasers are emerging with very promising manufacturing characteristics and they offer many advantages compared to the microsecond laser. Initial reports give a surface roughness for a surface machined by a picosecond laser to be around the 0.3 μm.

The application of a megasonic bath to clean the debris and loose contaminants also looks to provide a cleaning alternative which requires investigation.

Appendix A

DML 40 SI Laser milling machine

Figure A.1 The DML 40 SI laser milling machine

Machining area	
X axis travel	400 mm
Y axis travel	300 mm
X axis travel	500 mm
Table size	300 ×400 mm
Max table load	50 kg
Operation distance	60 mm
Laser source characteristics	
Type	Nd:YAG
Wavelength	1064 nm
Pulse	Q-Switch
Output modes	Continuous wave (CW) Pulse operation (QS) 0.1 – 50 kHz
CW output power	100 W
QS output power	200 kW/pulse at 1 kHz 40 kW/pulse at 10 kHz
Energy density	Up to 2x 10^4 J/m^2
Average power density	Up to 10^6 W/m^2
Peak power density of a single pulse at 10 kHz	Up to 5 x 10^{11} W/m^2
Scanning speed	Up to 500 mm/s
Laser working area	
Maximum machining depth	10 mm

Beam spot diameter	0.04 – 0.1 mm

Table A.1 Technical specifications of the DML 40 SI

Appendix B

Accuracy Experiment Test Structure

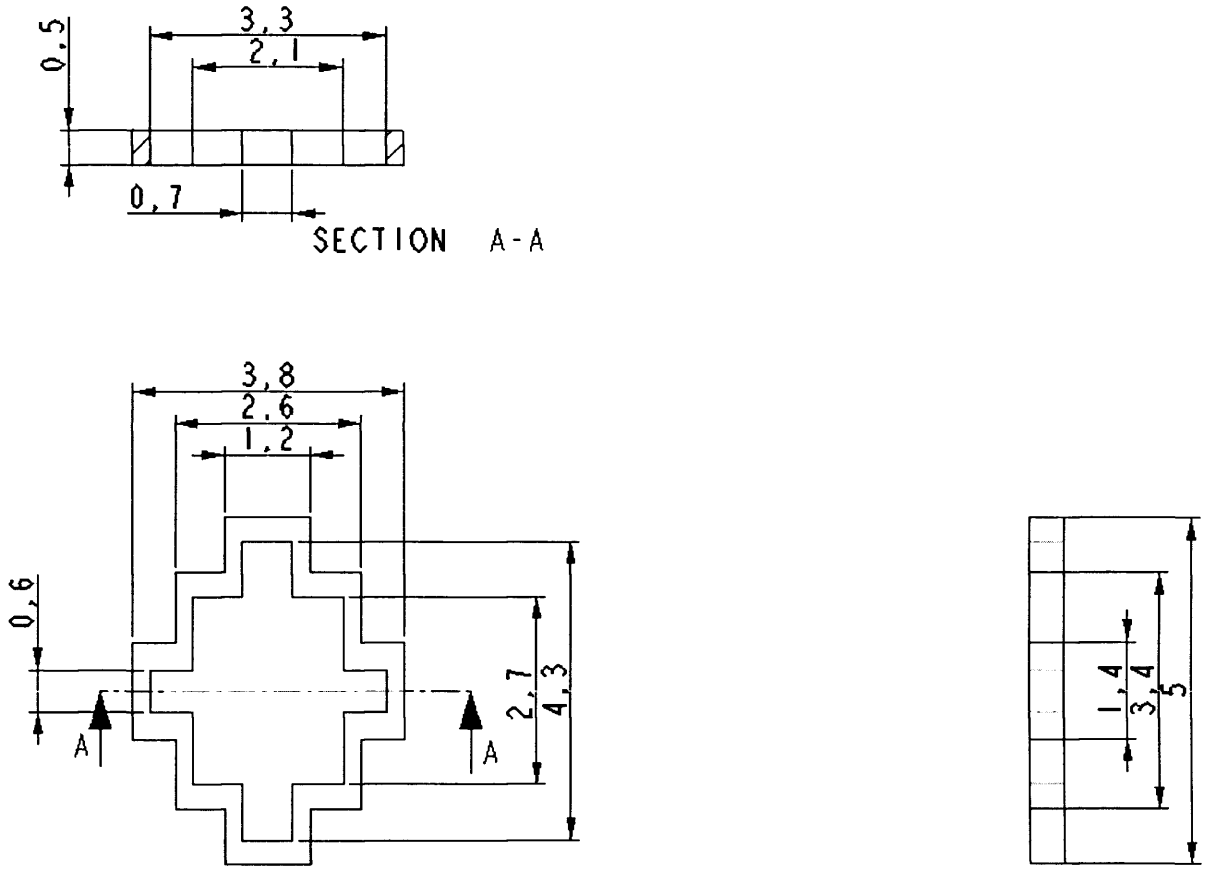

Figure B.1 Nominal dimensions for the accuracy experiment test feature

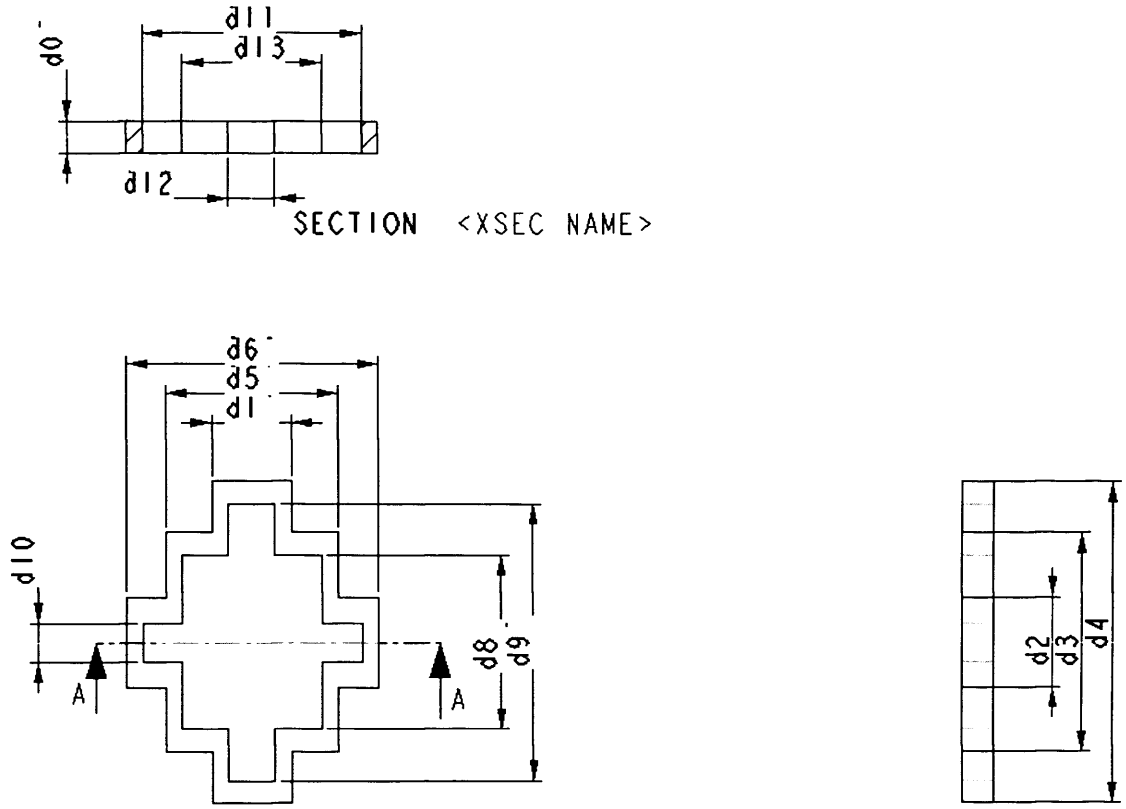

Figure B.2 Dimension designations for the accuracy experiment test feature

Appendix C

Results from laser cleaning of copper

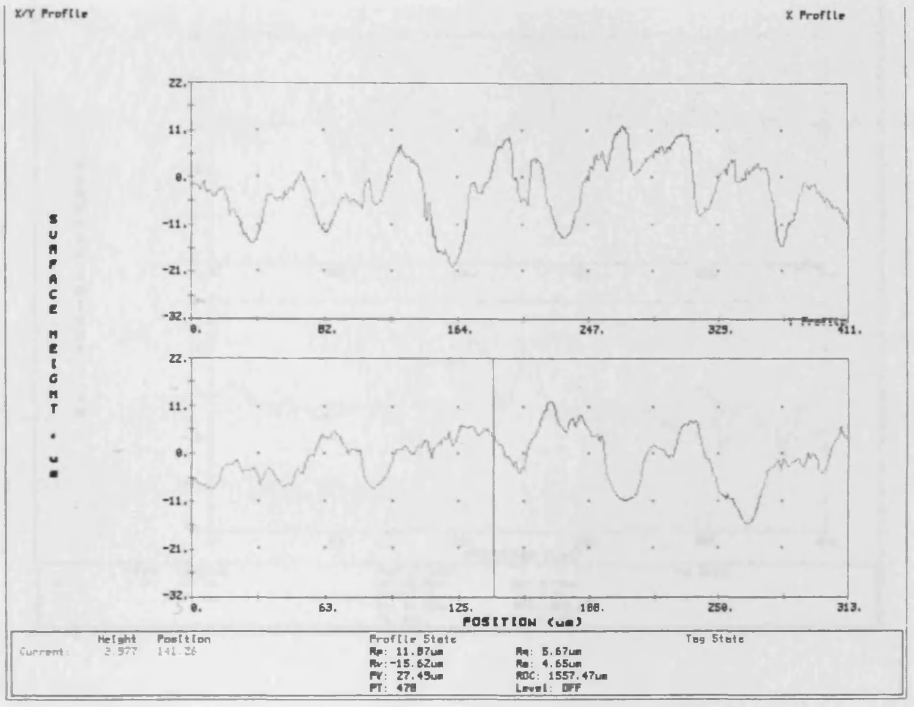

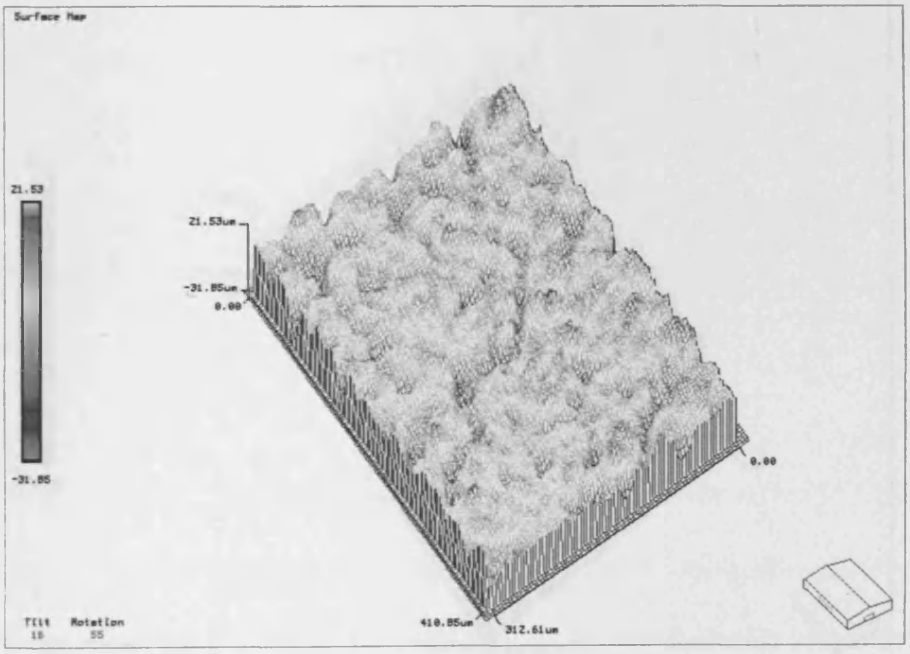

Figure C.1 Line profiles and surface map of copper without laser cleaning

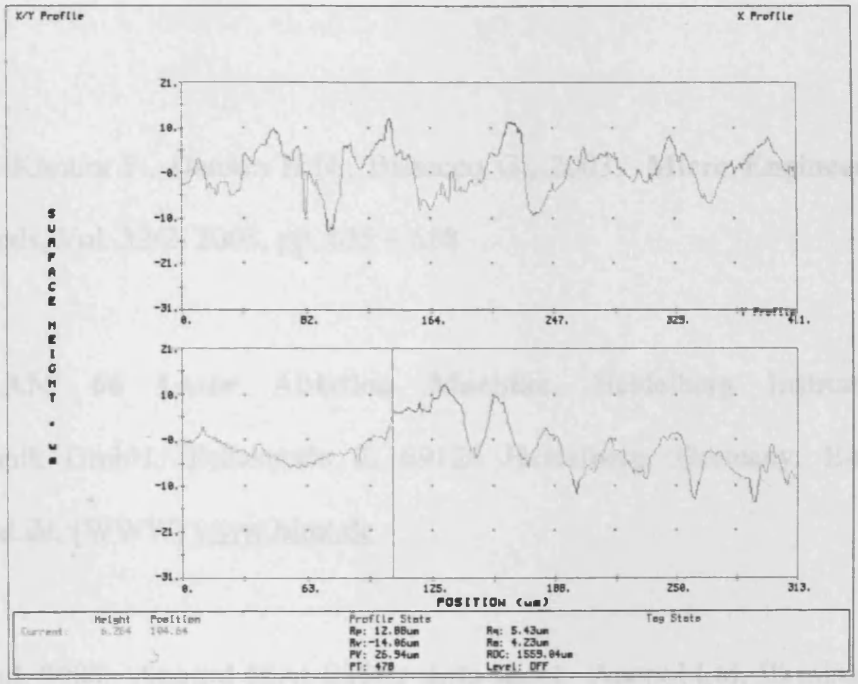

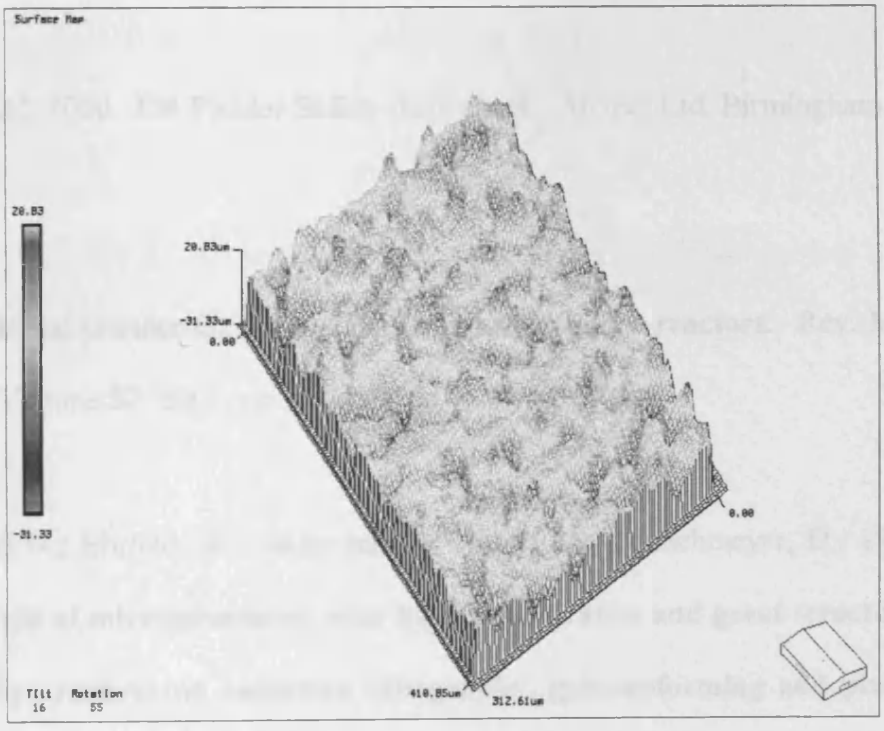

Figure C.2 Line profiles and surface map of copper after laser cleaning with -2 mm offset

REFERENCES

Alting L., Kimura F., Hansen H.N., Bissacco G., 2003. **Micro Engineering.** CIRP Annals, Vol. 52/2, 2003, pp. 635 – 658

Anon. **LAM 66 Laser Ablation Machine.** Heidelberg Instruments Mikrotechnik GmbH, Tullastraße 2, 69126 Heidelberg, Germany. E-mail: himt@himt.de, [WWW] www.himt.de

Anopol Ltd, 2000. **Anopol 66A: Safety data sheet.** Anopol Ltd, Birmingham B5 5QJ

Anopol Ltd, 2000. **EB Pickle: Safety data sheet.** Anopol Ltd, Birmingham B5 5QJ

Becker H. and Gärtner C., 2001. **Polymer based micro-reactors.** Rev. Mol. Biotech. Volume 82, 2001, pp. 89 – 99

Becker, E.W.; Ehrfeld, W.; Hagmann, P.; Maner, A.; Munchmeyer, D., 1986. **Fabrication of microstructures with high aspect ratios and great structural heights by synchrotron radiation lithography, galvanoforming and plastic moulding (LIGA Process).** Microelectronics Engineering, Volume 4, 1986, pp. 35 – 56.

Becker, H. and Heim, U., 1999. **Silicon as tool material for polymer hot embossing**. Proc. MEMS'99, Orlando, 1999, pp. 228 – 232

Becker, H. and Heim, U., 2000. **Hot embossing as a method for the fabrication of polymer high aspect ratio structures.** Sensors and Actuators, Volume 83 (2000), pp. 130 – 135

Billings, B.H. et al., 1972. **American Institute of Physics Handbook**. 3rd ed., New York: McGraw-Hill, 1972

Bogdanski, N., Schulz, H., Wissen, M., Scheer, H. -C., Zajadacz, J., and Zimmer, K. , 2004. **3D-Hot embossing of undercut structures – an approach to micro-zippers**. Microelectronic Engineering, Volumes 73-74, June 2004, pp. 190 - 195

Braun A., Zimmer K. and Bigl F., 2000. **Combination of contour and half-tone masks used in laser ablation.** Applied Surface Science, Vol. 168, Issues 1-4, 2000, pp. 178 - 181

Carslaw, H. S., and Jaeger, J. C., 1959. **Conduction of heat in solids**. Oxford University Press, 2nd Edition, 1959

Chabloz, M., Sakai, Y., Matsuura, T., Tsutsumi, K., (1999). **Improvement of sidewalls roughness in deep silicon etching**. Proc. HARMST'99, Kisarasu, Japan , 1999, pp. 26 – 27

Chang, H.-K., Kim, Y.-K., 2000. **UV-LIGA process for high aspect ratio structure using stress barrier and C-shaped etch hole.** Sensors and actuators, Volume 84 (2000), pp. 342 – 350

Cline, H. E. and Anthony, T.R., 1977. **Heat treating and melting material with a scanning laser or electron beam.** Journal of Applied Physics, 1977, Vol. 48, pp. 3895 - 3900

COHERENT, 2004. [WWW]
Laser power meter: Coherent FieldMaster GS
(http://www.coherentinc.com/Products/index.cfm?fuseaction=Interfaces.Product&PCID=4&PLID=22&PDID=255)
Laser power sensor: - Coherent LM200 HTD
(http://www.coherentinc.com/Products/index.cfm?fuseaction=Interfaces.Product&PCID=4&PLID=106&PDID=706)
Last visited: 12-06-04

Costa A.P., Quintino L. and Greitmann M., 2003. **Laser beam welding hard metals to steel.** Journal of Materials Processing Technology, Volume 141, Issue 2, 2003, pp. 163-173

Fähler, S. and Krebs, H.-U., 1996. **Calculations and experiments of material removal and kinetic energy during pulsed laser ablation of metals.** Applied Surface Science, 1996, Vol. 96 – 98, pp. 61 – 65

Flynn H G, 1964. **Physics of acoustic cavitation in liquids.** Physical Acoustics, vol. 1B, Academic Press, New York, 1964

Fraunhofer Institut Lasertechnik (ILT) website: [WWW] http://www.ilt.fhg.de/eng/lasertypen.html
Last visited: 17-01-03

Gale M. T., 1997. **Replication techniques for diffractive optical elements.** Microelectronic Engineering, Volume 34, Issues 3-4, December 1997, Pages 321 - 339

Ghodssi, R., Beebe, D. J., White, V. and Denton D. D., 1998. **Development of a tangential tactor using a LIGA/MEMS linear microactuator technology.** MicroElectro - Mechanical Systems (MEMS). 1998 International Mechanical Engineering Congress and Exposition, New York, NY, USA

Gietzelt T., Jacobi O., Piotter V., Ruprecht R. and Hausselt J., 2004. **Development of a micro annular gear pump by micro powder injection moulding.** Journal of Material Science, Volume 39, 2004, pp. 2113 – 2119

Goode B.J., Jones R.D. and Howells J.N.H., 1998. **Ultrasonic pickling of steel strip.** Ultrasonics, Vol. 36, 1998, p. 79

Gotz, T., Bergt, M., Hoheisel, W., Trager, F., Stuke, M., 1996. **Laser ablation**

of metals: the transition from non-thermal process to thermal evaporation. Applied Surface Science, Volume 96-98, 1996, pp. 280 - 286

Harzic R. Le, Breitling D., Weikert M., Sommer S., Föhl C., Valette S., Donnet C., Audouard E. and Dausinger F., 2005. **Pulse width and energy influence on laser micromachining of metals in a range of 100 fs to 5 ps.** Applied Surface Science, *In Press, Corrected Proof*, Available online 21 January 2005

Hatano H. and Kanai S., 1996. **High-frequency ultrasonic cleaning tank utilising oblique incidence.** IEEE Transactions on Ultrasonics, Ferroelectrics, and Frequency Control, 1996, Vol 43(4), pp. 531 - 535

Hellrung, D., Yeh, Li-Ya, Depiereux, Fr., Gillner, A., Poprawe, R., 1999. **High-accuracy micromachining of ceramics by frequency-tripled Nd:YAG lasers.** Proceedings SPIE Vol. 3618 (1999), pp. 348 - 356

Heyl, P., Olschewski, T., Wijnaendts, R. W., 2001. **Manufacturing of 3D structures for micro-tools using laser ablation.** Microelectronic Engineering, Volume 57 – 58, 2001, pp. 775 - 780

Hocheng H. and Pa P.S., 2003. **Electropolishing of cylindrical workpiece of tool materials using disc-form electrodes.** Journal of Materials Processing Technology Vol. 142 (2003), pp. 203 – 212

Hsu H.-T. and Lin J., 2005. **Thermal–mechanical analysis of the surface**

waves in laser cleaning. International Journal of Machine Tools & Manufacture, Vol. 45 (2005), pp. 979 – 985

Ihlemann J. and Rubahn K., 2000. **Excimer laser micro machining: fabrication and applications of dielectric masks**. Applied Surface Science Vol. 154–155, 2000, pp. 587 – 592

Incropera, F. P., 2002. **Fundamentals of heat and mass transfer** / Frank P. Incropera, David P. DeWitt., ed. 5. New York : J. Wiley, 2002

Jandeleit, J., Horn, A., Weichenhain, R., Kreutz, E. W., Poprawe, R., (1998) **Fundamental investigations of micromachining by nano- and picosecond laser radiation**. Journal of Applied Surface Science, Volume 127-129 (1998), pp. 885 – 891

Kaldos A., Pieper H.J., Wolf E., Krause M., 2004. **Laser machining in die making — a modern rapid tooling process**. Journal of Materials Processing Technology 155–156, 2004, pp. 1815 – 1820

Kao P S and Hocheng H, 2003. **Optimization of electrochemical polishing of stainless steel by grey relational analysis**. Journal of Materials Processing Technology, Volume 140, 2003, pp. 255 - 259

Kemmann, O., Weber, L., 2001. **Simulation of the micro injection moulding process**. Chapter 3 in **Specialized Moulding Techniques**, edited by Heim, H-

P.; Potente, H., ISBN: 1-884207-91-X, William Andrew Publishing/Plastics Design Library, 2001.

Kim J O, Choi S, Kim J H, 1999. **Vibroacoustic characteristics of ultrasonic cleaners**. Applied Acoustics, 1999, Vol. 58, pp. 211 – 228

Kjær E. M., Johansen B. B., Sørensen H. H., Rasmussen H. K., Arlø U. R., 2002. **Micro injection moulding**. Proc. of the 1st Euspen topical conference on fabrication and metrology in nanotechnology, Copenhagen, Denmark, pp. 259 - 267

Kuehn T.H., Kittelson D.B., Wu Y. and Gouk R., 1996. **Particle removal from semiconductor wafers by megasonic cleaning**. J. Aerosol Sci. 27 (1996), p. 427.

Lasertech GmbH, 1999. **Operating manual.** Gildemeister Lasertec GmbH, Tirolerstrasse 85, D 87459 Pfronten, Germany

Li L.-F. and Celis J.-P., 2003. **Pickling of austenitic stainless steels (a review)**. Canadian Metallurgical Quarterly, Volume 42 (2003), pp. 365 – 376

Li L.-F., Caenen P., Daerden M., Vaes D., Meers G., Dhondt C., and Celis J.-P., 2005. **Mechanism of single and multiple step pickling of 304 stainless steel in acid electrolytes**. Corrosion Science, Volume 47, Issue 5, May 2005, Pages 1307-1324

Lierath F., Pieper H.J., Wolf E., 2003. **Laser machining — a modern tooling process.** Proceedings of the CAMT Conference on Modern Trends in Manufacturing, Wroclaw, 2003, pp. 433–446

Lin L., Shia T K and Chiu C-J, 2000. **Silicon-processed plastic micropyramids for brightness enhancement applications.** Journal of Micromechanical Microengineering, Volume 10 (2000), pp. 395 – 400

Liu, X., Du, D., and Mourou, G., 1997. **Laser ablation and micromachining with ultrashort laser pulses.** IEEE J. Quantum Electronics, 1997, Vol. 33, No. 10, pp. 1706 – 1716

Lunney, J. G. and Jordan, R., 1998. **Pulsed laser ablation of metals.** Applied Surface Science, 1998, Vol. 127 – 129, pp. 941 – 946

Madou, M J, **(2001) Fundamentals of Microfabrication – The Science of Miniaturisation.** 2nd Ed. *CRC Press,* Boca Raton, Florida

Makarova, O. V.; Mancini, D. C.; Moldovan, N.; Divan, R.; Tang, Cha-Mei; Ryding, D. G.; Lee, R. H., (2003). **Microfabrication of freestanding metal structures using graphite substrate.** Sensors and Actuators A: Physical, Volume 103, Issues 1-2, 15 January 2003, Pages 182-186

Manca, O., Morrone, B., and Naso, V., 1995. **Quasi-steady-state three-**

dimensional temperature distribution induced by a moving circular Gaussian heat source in a finite depth solid. Int. J. Heat Mass Transfer, 1995, Vol. 38, No. 7, pp. 1305 – 1315

Mazumder, J. and Steen, W. M., 1980. **Heat transfer model for CW laser material processing**. Journal of Applied Physics, 1980, Volume 51, pp. 941 - 947

Mecomber J.S., Hurd D. and Limbach P.A., 2005. **Enhanced machining of micron-scale features in microchip moulding masters by CNC milling**. Int J of Machine Tools and Manufacture, In Press, Corrected Proofs, Available online 24 February 2005

Meeusen, W., Reynaerts, D., Peirs, J., Brussel, H. Van, Dierickx, V., Driesen, W., (2001). **The machining of freeform micro moulds by micro edm; work in progress**. Proc. MME 2001 (Micromechanics Europe Workshop), Cork, Ireland, 2001, pp. 46 – 49

Meijer J., 2004. **Laser beam machining (LBM), state of the art and new opportunities**. Journal of Materials Processing Technology, Volume 149, Issues 1-3, 2004, pp. 2 - 17

Melles Griot Website: [WWW]

http://beammeasurement.mellesgriot.com/tut_gaussian_beam_prop.asp

Last visit: 18-11-2004

MicroXAM, 2003. **MapVue software user manual.** ADE PhaseShift, USA, 2003

Modest, M. F., 1996. **Three-dimensional, transient model for laser machining of ablating/decomposing materials.** Int. J. Heat Mass Transfer, 1996, Vol. 39, No. 2, pp. 221 – 234

Nantel M, Yashkir Y, Lee S K, Mugford C, and Hockley B S, 2001. **Laser micromachining of semiconductors for photonics applications.** Proceedings of SPIE – Vol. 4594, October 2001, pp. 156-167

Nath, A.K., Sridhar, R., Ganesh, P. and Kaul, R., 2002. **Laser power coupling efficiency in conduction and keyhole welding of austenitic stainless steel.** SADHANA - India, Vol. 27, Part 3, June 2002, pp. 383 – 392

Nikumb S., Chen Q., Li C., Reshef H.,. Zheng H.Y, Qiu H. and Low D., 2004. **Precision glass machining, drilling and profile cutting by short pulse lasers.** Thin Solid Films, Vol. 477, Issues 1-2, 2005, pp. 216 - 221

Ong N., Koh Y.and Fu Y., 2002. **Microlens array produced using hot embossing process.** Microelectronical Engineering, Volume 60 (2002), pp. 365 – 379

O'Shea, D. C., 1985. **Elements of Modern Optical Design.** John Wiley and

Sons, 1985

Palik, E.D., 1985. **Handbook of Optical Constants of Solids**. Academic Press Inc., NY, 1985

Petzoldt S., Reif J., Matthias E., 1996. **Laser plasma threshold of metals**. Applied Surface Science, Volume 96 – 98, 1996, pp. 199 – 204

Pham, D. T., Dimov, S. S., Ji, C., Petkov, P. V., Dobrev, T., 2004. **Laser milling as a 'rapid' micromanufacturing process**. Proc. Institution of Mechanical Engineers, Volume 218 Part B: Journal of Engineering Manufacture, pp. 1 - 7

Pham, D. T., Dimov, S. S., Petkov, P. V., Petkov, S. P., 2001. **Rapid manufacturing of ceramic parts**. Proceedings of 17th National Conference on Manufacturing Research, Cardiff University, Cardiff, pp. 211 – 216

Pham, D. T., Dimov, S. S., Petkov, P. V., Petkov, S. P., 2002. **Laser Milling.** Proc Institution of Mechanical Engineers, Volume 216, Number 5, Part B: Journal of Engineering Manufacture (2002), pp. 657 – 669.

Piotter V., Benzler T., Müller K., Ruprecht R., and Hausselt J., 2002. **Micro injection moulding of components for microsystems**. Proc. of the 1st Euspen topical conference on fabrication and metrology in nanotechnology, Copenhagen, Denmark, pp. 182 - 189

Pronko, P. P., Dutta, S. K., Squier, J., Rudd, J. V., Du, D., Mourou, G., 1995 **Machining of sub-micron holes using a femtosecond laser at 800 nm.** Optics Communications Vol. 114 (1995), pp. 106 – 110

Provatas M.,. Edwards S.A and Choudhury N.R., 2002. **Surface finish of injection moulded materials by micro-thermal analysis.** Thermochim. Acta., Volume 392 (2002), pp. 339 – 355

Qi Q and Brereton G J, 1995. **Mechanisms of removal of micron-sized particles by high-frequency ultrasonic waves.** IEEE Transactions on Ultrasonics, Ferroelectrics, and Frequency Control, 1995, Vol. 42(4), pp. 619 – 629

QuickVision, 2001. **QuickVision AccelPro user manual.** Mitutoyo Japan Corporation, 2001

Ready, J. F., 1971. **Effects of high power laser radiation.** Academic Press, New York, 1971

Rizvi N.H. and Apte P., 2002. **Developments in laser micro-machining techniques.** Journal of Materials Processing Technology, Volume 127, Issue 2, 2002, pp. 206-210

Rudy S F, 2002. **Pickling and acid dipping.** Metal Finishing, Volume 100,

Supplement 1, January 2002, Pages 173 - 179

Rudzki, George J., 1983. **Surface finishing systems: metal and non-metal finishing handbook**. Finishing Publications Ltd.,UK, 1983

Ruprecht R., Gietzelt T., Muller K., Piotter V. and Jausselt J., 2002. **Injection moulding of microstructured components from plastics, metals and ceramics.** Microsystem Technology, Volume 8 (2002), pp. 351 – 358

Rykalin, N. N., Uglov, A. A., and Makarov, N. I., 1967. **Effects of peak frequency in a laser pulse on the heating of metal sheets**. Soviet Physics – Doklady, Vol. 12, 1967, pp. 664 – 646

Scanning electron microscopy, 2004 [WWW]

http://mse.iastate.edu/microscopy/home.html

Last visited: 24-10-2004

Schaller, Th., Bohn, L., Mayer, J., Schubert, K., 1999. **Microstructure grooves with a width of less than 50 μm cut with ground hard metal micro end mills**. Precision Engineering 23 (1999), pp. 229 – 235

Shan X.C., Ikehara T., Murakoshi Y. and Maeda R., 2005. **Applications of micro hot embossing for optical switch formation**. Sensors and Actuators A: Physical, Volume 119, Issue 2, 13 April 2005, pp. 433 – 440

Shao T.M., Hua M., Tam H.Y., Cheung E.H.M., 2005. **An approach to modelling of laser polishing of metals.** Surface and Coatings Technology, Vol. 197, Issue 1, 2005, pp. 77 - 84

Smurov, I.Yu., Uglov, A.A., Lashyn, A.M., Matteazzi, P., Covelli, L. and Tagliaferri, V., 1991. **Modelling of pulse-periodic energy flow action on metallic materials.** International Journal of Heat and Mass Transfer, Volume 34, 1991, No 4/5, pp. 961 – 971

Spennemann, A.; Michaeli, W.; 2001. **Process Analysis and Injection Moulding of Microstructures.** Chapter 3 in **Specialized Molding Techniques,** edited by Heim, H-P.; Potente, H., ISBN: 1-884207-91-X, William Andrew Publishing/Plastics Design Library, 2001.

Spiricon Inc., 2003 [WWW]. **Industrial beam profilers**
(http://www.spiricon.com/pdf/IBP_Data_Sheet.pdf)
Last visited: 11-03-05

Tam A.C., Leung W.P., Zapka W. and Ziemlich W., 1992. **Laser-cleaning techniques for removal of surface particulates.** Journal of Applied Physics Volume 71 (1992), pp. 3515–3523

Tam S.C., Loh N.L., Mah C.P. A. and Loh N.H., 1992. **Electrochemical polishing of biomedical titanium orifice rings.** Journal of Material Processing Technology, Vol. 35(1), 1992, pp. 83 - 91

Tay B.Y., Liu L., Loh N.H., Tor S.B., Murakoshi Y. and Maeda R., 2005. **Surface roughness of microstructured component fabricated by μMIM.** Materials Science and Engineering A, Volume 396, Issues 1-2, 2005, pp. 311 – 319

Tsai C.-H. and Chen H.-W., 2003. **Laser milling of cavity in ceramic substrate by fracture-machining element technique.** Journal of Materials Processing Technology, Volume 136, Issues 1-3, 2003, pp. 158 - 165

Waits, C.M., Kastantin, M., Ghodssi, R., 2003. **Investigation of gray-scale technology for large area 3D silicon MEMS structures.** Journal of Micromechanical Microengineering, Volume 13 (2003), pp. 170 – 177.

Waits, C.M., Morgan, B., Kastantin, M., Ghodssi, R., (2005). **Microfabrication of 3D silicon MEMS structures using gray-scale lithography and deep reactive ion etching**. Sensors and Actuators A: Physical, Volume119 (2005), pp. 245 – 253

Weaver, J.H., Krafka, C., Lynch, D.W. and Koch, E.E., 1981. **Optical properties of metals, Vol. I and Vol. II**. Zentralstelle für Atomkernenergie-Dokumentation, ZAED, 1981,

White, R. M., 1963. **Generation of elastic waves by transient surface**

heating. Journal of Applied Physics, Vol. 34, 1963, pp. 3559 – 3567

Wilson, J. and Hawkes, J.F.B., 1987. **Lasers: principles and applications.** Prentice Hall - Europe, 1987

Wilson, J., 1971. **Practice and Theory of Electrochemical Machining.** Wiley/Interscience, New York, 1971

Yilbas B.S., Gbadebo S.A. , and Sami M., 2000. **Laser heating: an electron-kinetic theory approach and induced thermal stresses.** Optics and Lasers in Engineering, 2000, Vol. 33, pp. 65 – 79

Zhu X., 2000. **A new method for determining critical pulse width in laser material processing.** Applied Surface Science, Volume 167, 2000, pp. 230 – 242